NMR Methods for a comprehensive and fast characterisation of mass transport in porous materials

Dissertation

zur Erlangung des Doktorgrades der Naturwissenschaften
- Doctor rerum naturalium -

vorgelegt
dem Fachbereich 02 (Biologie/Chemie)
der Universität Bremen

von
Adrian Ricke, Master of Science
geboren am 11. November 1993 in Osnabrück

Bremen, 2023

Gutachter:

Herr Priv.-Doz. Dr. Wolfgang Dreher
AG in-vivo-MR, FB02 (Chemie/Biologie)
Universität Bremen

Herr Prof. Dr. Matthias Günther
Fraunhofer-Institut für Digitale Medizin MEVIS
Bremen

Weitere Mitglieder der Prüfungskomission:

Herr Prof. Dr. Peter Spiteller
AG Instrumentelle Analytik, FB02 (Chemie/Biologie)
Universität Bremen

Herr Prof. Dr. Marcus Bäumer
AG Nanostrukturierte Oberflächen, FB02 (Chemie/Biologie)
Universität Bremen

Herr Dr. Ekkehard Küstermann
AG in-vivo-MR, FB02 (Chemie/Biologie)
Universität Bremen

Herr Jakob Maibaum
Universität Bremen

Promotionskolloquium am 14.12.2023

Lebenslauf und Publikationsliste

Persönliche Daten

- Name: Adrian Ricke

- geboren: 11.11.1993

Lebenslauf

- August 2000 - Juni 2004: Grundschule St. Antonius, Osnabrück

- August 2004 - Juli 2012: Gymnasium Angelaschule (Abitur), Osnabrück

- Oktober 2013 - März 2017: Bachelorstudium der Physik (B.Sc.), Universität Osnabrück

- März 2017 - März 2019: Masterstudium der Physik (M.Sc.)

- Mai 2019 - August 2019: Wissenschaftliche Hilfskraft, Fachbereich Physik, Universität Osnabrück

- Oktober 2019 - März 2023: Wissenschaftlicher Mitarbeiter, DFG-Graduiertenkolleg MIMENIMA (GRK 1860), Fachbereich 02 (Biologie/Chemie), Universität Bremen

Wissenschaftliche Veröffentlichungen: Die Publikationen [1-4] sind im Rahmen meines Bachelor- sowie Masterstudiums der Physik an der Universität Osnabrück entstanden und haben thematisch keine Verbindung zu dieser Dissertation. Die Publikationen [5-7] entstanden während meines Promotionsstudiums an der Universität Bremen.

[1] <u>Adrian Ricke</u>, Elena Bondarenko, Györgyi Úr, Tamás Kálai, Kálmán Hideg, Heinz-Jürgen Steinhoff, and Michael Matthies. Interaction Kinetics of Sulfadiazine and N-Acetyl-sulfadiazine with Soil Humic Acid: ESR Investigations with Nitroxide Spin Label. *Applied Magnetic Resonance*, 50:171–185, 2019. `https://doi.org/10.1007/s00723-018-1082-2`

[2] Wageiha Mosslehy, Natalia Voskoboynikova, Alexandr Colbasevici, <u>Adrian Ricke</u>, Daniel Klose, Johann P. Klare, Armen Y. Mulkidjanian, and Heinz-Jürgen Steinhoff. Conformational Dynamics of Sensory Rhodopsin II in Nanolipoprotein and Styrene–Maleic Acid Lipid Particles. *Photochemistry and Photobiology*, 95(5):1195–1204, 2019. `https://doi.org/10.1111/php.13096`

[3] Friedrich Finkenwirth, Michael Sippach, Sinah N. Pecina, Mario Gäde, Julia Ruta, <u>Adrian Ricke</u>, Elena Bondarenko, Johann P. Klare, Maximilian Zinke, Sascha Lange, Adam Lange, Heinz-Jürgen Steinhoff, and Thomas Eitinger. Dynamic interactions of CbiN and CbiM trigger activity of a cobalt energy-coupling-factor transporter. *Biochimica et Biophysica Acta (BBA) - Biomembranes*, 1862(2):183114,

2020. `https://doi.org/10.1016/j.bbamem.2019.183114`

[4] <u>Adrian Ricke</u>, Tamás Kálai, Heinz-Jürgen Steinhoff, and Michael Matthies. Interaction kinetics and accessibility of sulfadiazine in model clay-humic acid suspension: Electron spin resonance investigations with nitroxide spin label. *Science of The Total Environment*, 796:149042, 2021. `https://doi.org/10.1016/j.scitotenv.2021.149042`

[5] <u>Adrian Ricke</u>, Mehrdad Sadeghi, and Wolfgang Dreher. Magnetic Resonance Velocimetry for porous media: sources and reduction of measurement errors for improved accuracy. *Experiments in Fluids*, 64(7):132, 2023. `https://doi.org/10.1007/s00348-023-03666-z`

[6] Mehrdad Sadeghi, <u>Adrian Ricke</u>, Georg R. Pesch, Wolfgang Dreher, and Jorg Thöming. Comparative full-field velocimetry of liquid flow within monolithic catalyst carriers via CFD simulations and MRV measurements. *Experiments in Fluids*, 64(8):138, 2023. `https://doi.org/10.1007/s00348-023-03681-0`

[7] Thomas Ilzig, <u>Adrian Ricke</u>, Judith M. U. Siebert, Michaela Wilhelm, Wolfgang Dreher, and Stefan Odenbach. Quantitative analysis of colloid retention and pore fluid flow in monolithic, open-porous media by X-ray computed microtomography and magnetic resonance velocimetry. *Chemical Engineering Science*, 119299, 2023. `https://doi.org/10.1016/j.ces.2023.119299`

Zusammenfassung

Die kernmagnetische Resonanz (NMR) ist eine leistungsfähige Messmethode zur nicht-invasiven Untersuchung statischer und dynamischer Eigenschaften von Fluiden in komplexen und undurchsichtigen Strukturen. Verschiedene Eigenschaften wie Stoffverteilung, Temperatur, Strömungsgeschwindigkeiten, Diffusionseigenschaften und vieles mehr können dreidimensional abgebildet werden. Die sogenannte Magnetic Resonance Velocimetry (MRV) ermöglicht die in situ Analyse der lokalen Strömungsgeschwindigkeit von Fluiden. Eine solche Analyse hilft bei der Charakterisierung von Stofftransporteigenschaften und der Validierung oder Verbesserung numerischer Simulationen für poröse Medien. Der Wert solcher Validierungen wird jedoch durch verschiedene Probleme, die die Messgenauigkeit verschlechtern, verringert.

In dieser Dissertation werden systematische Fehler und der Einfluss von Rauschen betrachtet, welche die Genauigkeit von MRV-Messungen verringern. Es werden unterschiedliche Techniken zur Minimierung oder Korrektur von Verschiebungs- und Phasenfehlern beschrieben. Insbesondere wird die sogenannte Dual-Velocity ENCoding (VENC)-Technik verwendet. Es wird beschrieben, wie das Verhältnis zwischen niedrigem und hohem VENC-Wert gewählt werden sollte, um die größtmögliche Verbesserung des Geschwindigkeit-zu-Rausch Verhältnisses (VNR) zu erzielen.

Als Kompromiss zwischen VNR, Gesamtmesszeit, räumlicher Auflösung und Verschiebungsfehlern wird eine neue Multi-Echo MRV-Sequenz vorgestellt. Zur Verbesserung des VNR wurde ein Dual-VENC-Kodierungsschema mit unterschiedlichen Geschwindigkeits-Kodierungsschritten für die einzelnen Echos verwendet. Die Wiederholungszeit T_R wurde optimiert, um eine weitere Verbesserung des VNR zu erreichen. Die beschriebene MRV-Sequenz wurde an einem präklinischen 7-Tesla Magnetresonanztomographen implementiert und zur Messung der dreidimensionalen Strömungsgeschwindigkeit von Wasser in einer Open Cell Foam (OCF)-Struktur und einer Wabenstruktur mit dreidimensionaler isotroper räumlicher Auflösung verwendet.

Die für die OCF-Struktur durchgeführten Geschwindigkeitsmessungen wurden zur Kreuzvalidierung mit Computional Fluid Dynamics (CFD)-Simulationen verwendet. Es wird eine Technik beschrieben, um die Geschwindigkeitskarten von MRV und CFD abzugleichen und ihre Übereinstimmung wurde anhand eines Ähnlichkeitsindexes quantifiziert. Der Einfluss verschiedener Artefakte auf den Ähnlichkeitsindex wird im Detail diskutiert. Um den Ursprung der verschiedenen Artefakte besser zu verstehen, wurden die Oberfläche und das Innere der OCF-Struktur getrennt betrachtet.

Abstract

Nuclear Magnetic Resonance (NMR) is a powerful tool for non-invasively investigating static and dynamic properties of fluids inside complex and opaque structures. Various properties such as substance distribution, temperature, flow velocities, diffusion properties and much more can be imaged three-dimensionally. The Magnetic Resonance Velocimetry (MRV) allows for the in situ analysis of the local flow velocity of fluids. Such an analysis characterises mass transport properties and helps to validate or improve numerical predictions for porous media. However, the benefit of such validations is lowered by several problems worsening the measurement accuracy.

This work addresses systematic errors and the influence of noise, which may reduce the accuracy of MRV measurements. Different techniques are described to minimise or correct displacement and phase errors. In particular, the so-called dual-Velocity ENCoding (VENC) technique is considered. It is described how the ratio between low- and high-VENC value should be chosen in order to obtain the highest possible improvement of the Velocity-to-Noise Ratio (VNR).

A new multi-echo MRV sequence is proposed as a compromise between VNR, total measurement time, spatial resolution and displacement errors. For improved VNR, a dual-VENC encoding scheme was used with different velocity encoding steps for the individual echoes. The repetition time T_R was optimised to achieve a further VNR improvement. The proposed MRV sequence was implemented on a 7 Tesla preclinical Magnetic Resonance Imaging (MRI) system and used to measure the three-directional flow velocity of water in an Open Cell Foam (OCF) structure and a honeycomb structure with three-dimensional isotropic spatial resolution.

The velocity measurements performed for the OCF structure were used for cross-validation with Computional Fluid Dynamics (CFD) simulations. A technique is described to match MRV and CFD velocity maps and their agreement was evaluated by a similarity index. The influence of different artefacts on the similarity index is evaluated in detail. To better understand the origin of different artefacts, the surface and the inside of the OCF structure were analysed separately.

Contents

List of Figures

List of Tables

List of used abbreviations

CFD Computional Fluid Dynamics

CCF Closed Cell Foam

CPI Channels Per Inch

FID Free Induction Decay

FLIESSEN FLow Imaging Employing Single-Shot ENcoding

FOV Field Of View

FT Fourier Transformation

GRE Gradient Echo

LDV Laser Doppler Velocimetry

MRI Magnetic Resonance Imaging

MRV Magnetic Resonance Velocimetry

NMR Nuclear Magnetic Resonance

OCF Open Cell Foam

PC Phase Contrast

PIV Particle Image Velocimetry

PLA PolyLacticAcid

PLIF Planar Laser Induced Fluorescence

PEPT Positron Emission Particle Tracking

PPI Pores Per Inch

RARE Rapid Acquisition with Relaxation Enhancement

RMSE Root-Mean-Square Error

ROI Region Of Interest

RF Radio Frequency

SE Spin Echo

SNR Signal-to-Noise Ratio

SSA Specific Surface Area

VENC Velocity ENCoding

VFR Volumetric Flow Rate

VNR Velocity-to-Noise Ratio

μ**CT** micro-Computed Tomography

Preface

This doctoral thesis is a contribution describing my work within the research project entitled "NMR Methods for a comprehensive and fast characterisation of mass transport in porous materials" (funded by the German Research Foundation from October 2019 to March 2023). The project aims at methodological improvements and optimisation of spatially resolved Magnetic Resonance Velocimetry (MRV) for characterizing mass transport processes in opaque porous materials. The project is divided into three subprojects and the corresponding structure of the thesis is as follows:

The general principles of Magnetic Resonance Imaging (MRI) and MRV are explained in chapter 1. In chapter 2, basics of fluid mechanics, porous media and the principle of Computational Fluid Dynamics (CFD) simulations are briefly explained. The setup for the flow measurements as well as the used porous samples are described in chapter 3. In chapter 4, a new multi-echo MRV sequence for measuring fluid flow velocity is described and verified by dedicated measurements. In chapter 5, different artefacts are explained, which may occur in MRV measurements. Correction techniques are described for improved accuracy of the measured flow maps. In chapter 6, the measurements performed with the multi-echo sequence from chapter 4 are used for cross-validation with CFD simulations. The agreement of the three-dimensional velocity maps is evaluated by determining a similarity index. A summary of this work is given in chapter 7.

1 General introduction to MRI and MRV

This work is focused on Magnetic Resonance Imaging (MRI), which is an imaging technique based on the Nuclear Magnetic Resonance (NMR) effect.

In medical diagnostics, MRI is one of the most important imaging techniques for examining various diseases, such as liver [1] or heart diseases [2], changes in brain metabolism [3] and detecting cancer at an early stage [4–8]. MRI is also gaining popularity in other scientific applications. It became an important tool in the field of chemical engineering to analyse catalytic reactions in terms of local temperature [9–11] or mapping the chemical composition [9,12–14]. Gases can be analysed in terms of diffusion [15] or dispersion [16, 17]. Early NMR studies on porous media were concerned with the study of spin-relaxation of fluids confined in such porous media [18, 19]. The so-called Magnetic Resonance Velocimetry (MRV) also became an important tool for analysing the fluid flow in porous media [20–23]. In combination with numerical simulation tools like Computional Fluid Dynamics (CFD) [24], MRV can be used for cross-validations [25, 26]. However, there are many factors that reduce the accuracy of such validations. In particular, these are metrological reasons that cause artefacts in the MRV images. These include displacement errors [27–29], partial volume effects [26, 30] and phase offsets introduced by eddy currents [31]. Many correction mechanisms have already been presented in the literature, but rather for medical applications than for porous media.

In the following, the fundamentals of MRI and MRV are explained briefly. Further details about MRI are explained in various text books [31–33].

1.1 Spin angular momentum

An intrinsic basic property of atoms and molecules is the quantum mechanical spin. The nuclear spin is characterised by the *spin quantum number I* and has, depending on the atom (respectively molecule), an integer or half-integer value. The classical analogue to the spin is the angular momentum. Its magnitude is given by

$$L = \hbar\sqrt{I(I+1)} \tag{1}$$

with the reduced Planck constant $\hbar = 6.626 \cdot 10^{-34}\,\mathrm{J \cdot s}/(2\pi)$. However, in MRI mainly particles with $I = \frac{1}{2}$ are used. Due to their high natural abundance and their large gyromagnetic ratio, ^{1}H and ^{19}F are widely used for MRI measurements. If an external magnetic field B_0 is applied, the magnetic moment of the spin is determined by

$$\vec{\mu} = \gamma \cdot \vec{L} \tag{2}$$

where γ is the gyromagnetic ratio. For ^{1}H it is $\gamma = 26.752 \cdot 10^7\,\frac{\mathrm{rad}}{\mathrm{T \cdot s}}$. The magnetic moment of the spin precesses around the direction of the field (usually defined as z-direction). In this context, the precession frequency is called Larmor frequency and is described as

$$\omega_0 = \gamma B_0 = \frac{E}{\hbar} \tag{3}$$

since the energy of a photon is proportional to the frequency ($E = h\nu = \hbar\omega$).
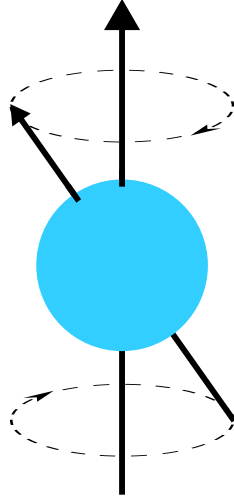
Figure 1: The magnetic moment $\vec{\mu}$ of the spin precesses about the static field B_0 at Larmor frequency ω_0.

1.2 Spin polarisation

Depending on the *spin quantum number*, a spin can be oriented in different discrete directions. This is described by the *spin magnetic quantum number* $m = -I, -I + 1, ..., I$, where the number of possible orientations is $2I + 1$. Thus, for a $\frac{1}{2}$-spin (like ^1H) two orientations are possible, $m = \pm\frac{1}{2}$. The magnitude of the angular momentum in the z-direction is given by

$$L_z = m\hbar. \tag{4}$$

If no external magnetic field is present, the spins in both states have the same energy level and are randomly distributed in both directions. If an external static magnetic field is applied, the spins are split into multiple energy levels due to the Zeeman-effect. According to eqs. (2) and (4), the energy is determined by
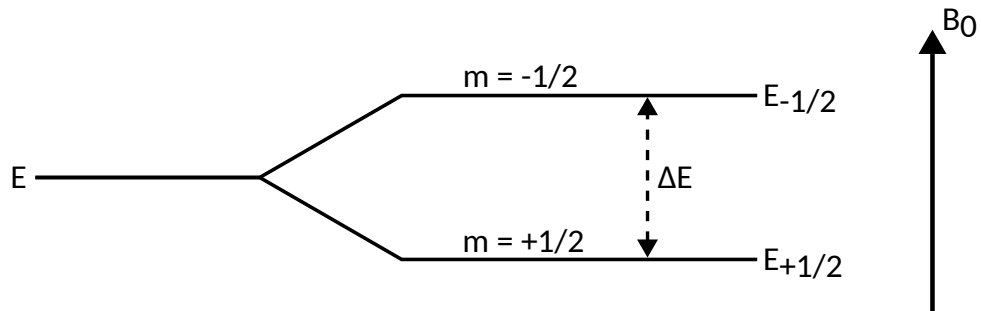
Figure 2: Without magnetic field, there is one energy level for a $\frac{1}{2}$-spin system. If an external magnetic field B_0 is applied, this energy level is split. The energy difference between both states is $\Delta E = \hbar\gamma B_0$.

$$E = -\vec{\mu} \cdot \vec{B_0} = -\hbar\gamma m B_0 \tag{5}$$

and the energy difference between neighbouring energy levels is

$$\Delta E = \hbar\gamma B_0. \tag{6}$$

2

For ^{1}H, two energy levels are present. The $m = -\frac{1}{2}$ state is the upper energy level and oriented antiparallel to the magnetic field. The state with $m = +\frac{1}{2}$ is the lower energy level and is oriented parallel to the magnetic field. This is the preferred state. Due to the difference between lower and upper energy level, a macroscopic magnetisation is present. This process of generating the net magnetization $\vec{M}_0$ of a sample is called polarisation.

The Maxwell-Boltzmann distribution describes the probability of the spins to take the lower $(N_+, \ m = +\frac{1}{2})$ and upper $(N_-, \ m = -\frac{1}{2})$ energy level. The ratio is described by

$$\frac{N_-}{N_+} = e^{-\frac{\Delta E}{k_\mathrm{B} T}} = e^{-\frac{\gamma \hbar B_0}{k_\mathrm{B} T}} = e^{-\frac{\hbar \omega_0}{k_\mathrm{B} T}} \tag{7}$$

with the Boltzmann constant $k_B = 1.381 \cdot 10^{-23} \frac{\mathrm{J}}{\mathrm{K}}$ and the temperature T. For the Taylor series with $\gamma \hbar B_0 \ll k_\mathrm{B} T$ it follows

$$\frac{N_-}{N_+} \approx 1 - \frac{\gamma \hbar B_0}{k_B T}. \tag{8}$$

The population difference is calculated as

$$\Delta N_\pm = N_+ - N_- = N_+ \cdot (1 - \frac{N_-}{N_+}) \propto N_\mathrm{total} \cdot \frac{\gamma \hbar B_0}{k_\mathrm{B} T} \tag{9}$$

where N_total is the total number of spins. For the net magnetisation of the spins it follows

$$M_0 = \Delta N_\pm \cdot \mu \propto N_\mathrm{total} \cdot \frac{\gamma^2 \hbar^2 B_0}{k_\mathrm{B} T}. \tag{10}$$

1.3 Excitation and relaxation

For an NMR measurement, the sample is polarised by applying an external magnetic field B_0. Therefore, the longitudinal net magnetisation vector M_0 is oriented parallel to B_0. By applying a time varying magnetic field pulse B_1 for a time duration τ, the sample is excited. The response of the nuclear magnetic moments (spins) is then evaluated.

For excitation, the resonance condition needs to be fulfilled, thus B_1 should have the Larmor frequency ω_0. For NMR, these are usually in the range of Radio Frequency (RF). For an MRI scanner with $B_0 = 7.05\,\mathrm{T}$ (^{1}H), the Larmor frequency is $\omega_0 = 1886\,\mathrm{MHz}$, respectively $\nu_0 = 300.3\,\mathrm{MHz}$ (see eq. (3)). B_1 is oriented perpendicular to B_0, thus the net magnetisation is flipped towards the xy-plane with the flip angle α with respect to the z-direction:

$$\alpha = \gamma B_1 \tau \tag{11}$$

It can be seen from the equation that the flip angle can be determined by the magnetic field strength and the duration τ of the applied pulse.

Before the RF-pulse is applied, the net magnetisation is oriented along B_0 (z-direction). It is $M_\mathrm{z} = M_0$ and $M_\mathrm{x} = M_\mathrm{y} = 0$, where M_0 is the equilibrium magnetisation. During the process of excitation, the magnetisation vector $\vec{M}$ precesses
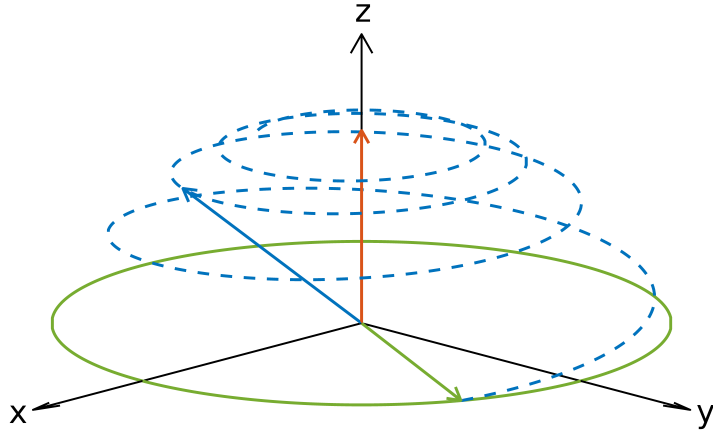
Figure 3: Motion of the magnetisation vector during a 90° excitation pulse: Initially, the magnetisation (orange vector) is oriented parallel to the external magnetic field B_0 (z-direction). During the process of excitation (applying a time varying magnetic field B_1), the magnetisation (blue vector) is tilted towards the xy-plane. Hereby, the magnetisation describes a spiral path (blue dashed line). After completing the magnetisation process, the magnetisation (green vector) lies in the xy-plane ($M_z = 0$). Its precession is described by a circle (drawn in green).

around the z-direction in the xy-plane and forms a spherical pattern (see fig. 3). Thus, the longitudinal component decreases while the transverse component increases until the flip angle is achieved. After applying an RF-pulse with a 90° flip angle, the magnetisation over the time t is given by $M_z = 0$, $M_x = M_0 \cdot \cos(\omega_0 t)$ and $M_y = M_0 \cdot \sin(\omega_0 t)$. Relaxation back to the thermal equilibrium takes place and the
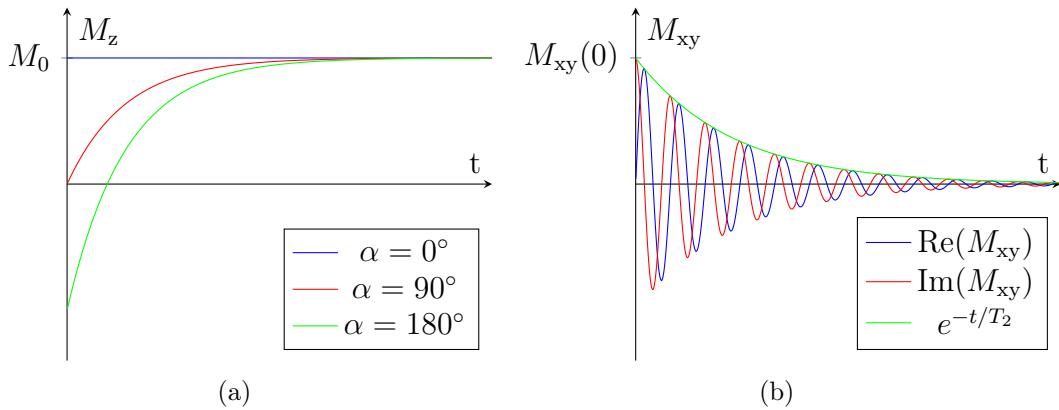
Figure 4: (a) During longitudinal relaxation, the magnetisation approaches the equilibrium value M_0 exponentially (eq. (13)). The initial magnetisation $M_z(0)$ depends on the flip angle α. (b) The transverse relaxation is described by an exponentially decaying sinusoidal (eq. (14)). Here, the real and imaginary part are phase shifted by 90°.

4

time-dependent magnetisation is described by the Bloch equation:

$$\frac{d\vec{M}}{dt} = \gamma \cdot \vec{M}(t) \times \vec{B}(t) - \frac{\vec{M}_{\mathrm{x}}(t) + \vec{M}_{\mathrm{y}}(t)}{T_2} - \frac{\vec{M}_{\mathrm{z}}(t) - \vec{M}_0}{T_1} \qquad (12)$$

The system emits energy in form of photons to the environment (also called lattice) to reach the equilibrium. Therefore, this process is called spin-lattice relaxation. In this context, the longitudinal magnetisation rises exponentially with the longitudinal relaxation time T_1 and can be described by

$$M_{\mathrm{z}}(t) = M_{\mathrm{z}}(0) \cdot e^{-t/T_1} + M_0 \cdot (1 - e^{-t/T_1}). \qquad (13)$$

This process is visualised in fig. 4(a). The initial magnetisation in z-direction depends on the flip angle α and is $M_{\mathrm{z}}(0) = M_0 \cdot \cos(\alpha)$. The transverse magnetisation

$$M_{\mathrm{xy}} = M_{\mathrm{x}} + iM_{\mathrm{y}}$$

can be described as

$$M_{\mathrm{xy}}(t) = M_0 \cdot \sin(\alpha) \cdot (\cos(\omega_0 t) + i\sin(\omega_0 t)) \cdot e^{-t/T_2} \qquad (14)$$

with the flip angle α. This is plotted in fig. 4(b). Real and imaginary signals are phase shifted to each other and sinus-shaped with exponential decaying amplitude (transverse relaxation time T_2). Interaction between the nuclei causes a fluctuation of the frequency, for example chemical interaction due to anisotropy, and the spins dephase. Therefore, this process is called spin-spin relaxation. The resulting Free Induction Decay (FID) is acquired as NMR signal by using an RF coil. It is $T_2 \leq T_1$ and therefore the transverse magnetisation usually disappears before the longitudinal magnetisation is fully recovered. The rotation of the magnetisation vector during the relaxation process is described by a spiral pattern.

A Fourier Transformation (FT) is done to transform the time-dependent NMR signals into the frequency domain:

$$M(\omega) = \int_{-\infty}^{+\infty} M(t)e^{-i\omega t}\, dt \qquad (15)$$

1.4 Gradient and Spin Echo

Two common techniques are used for MRI. Due to its rather short measurement time, Gradient Echo (GRE) sequences with small flip angles and short repetition time T_{R} (as for example the FLASH sequence [34,35]) are widely used in medical MRI to minimise blurring effects (for example caused by breathing or other movements of the body) or to minimise patient's discomfort. Dedicated gradients are applied for manipulation of the FID, which arises after applying an excitation RF-pulse and flipping the magnetisation into the xy-plane (fig. 5). First, a gradient is applied, which causes a dephasing of the spins. After applying a second gradient with same duration and strength but opposite polarity, the spins are rephased and a GRE is formed. However, the disadvantage of GRE sequences is that the signal amplitude depends on the FID. Due to inhomogeneities in the magnetic field and susceptibility
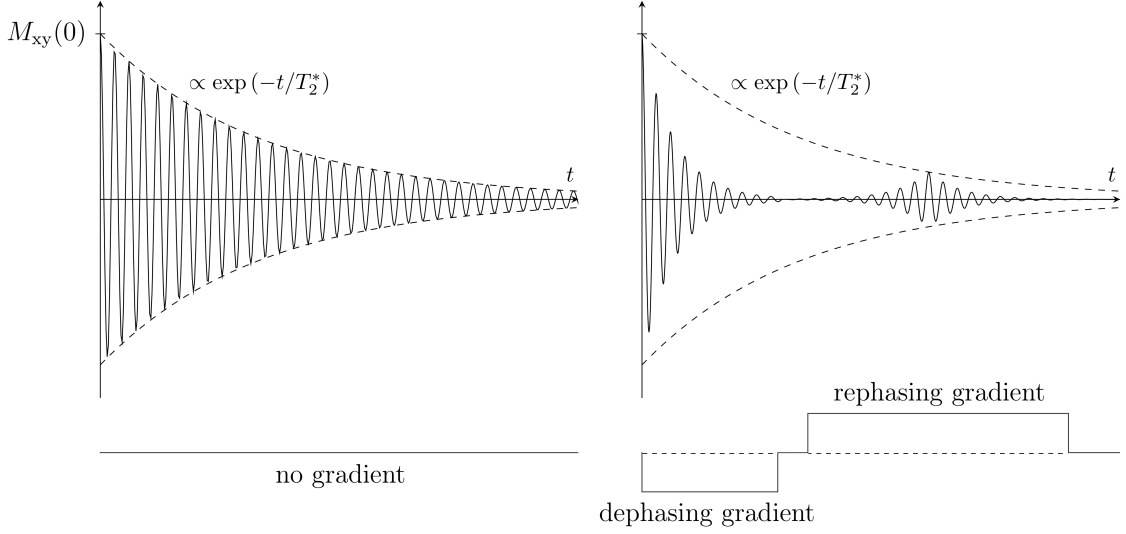
Figure 5: Formation of a Gradient Echo (GRE). At $t = 0$, an excitation RF-pulse is applied to flip the magnetisation into the xy-plane. On the left: Dephasing of the spins leads to an exponential decrease of the amplitude of the FID. Due to inhomogeneities in the magnetic field, this decrease is not characterised by the relaxation time T_2, but the shorter T_2^*. On the right: A dephasing gradient is applied, which accelerates the dephasing of the FID. A rephasing gradient with opposite polarity to the dephasing gradient reverses the phase change and a GRE is formed.

effects, the decrease of the FID is not characterised by the relaxation time T_2, but the shorter effective transverse relaxation time T_2^*:

$$\frac{1}{T_2^*} = \frac{1}{T_2} + \frac{1}{T_2'} \tag{16}$$

T_2' is inversely proportional to the magnetic field inhomogeneity ΔB_0 (full width at half maximum of a Lorentzian) [31]:

$$T_2' = \frac{2}{\gamma \Delta B_0} \tag{17}$$

In Spin Echo (SE) sequences, dephasing of the spins caused by T_2' effects is reversed (see fig. 6). Initially, an excitation RF-pulse is applied to flip the magnetisation into the xy-plane and the spins begin to dephase. The signal amplitude exponentially decreases with $\propto \exp(-t/T_2^*)$. After the time τ, a 180° RF-pulse is applied and the spins rephase. During this process, the signal loss due to T_2' effects is reversed. After an additional τ, the rephasing process is completed and an SE results. The signal amplitude of the SE is decreased by $\propto \exp(-2\tau/T_2)$ in comparison to the initial amplitude.

1.5 Magnetic Resonance Imaging

In addition to the static magnetic field B_0, magnetic field gradients (short: gradients) can be applied to encode spatial information (distribution or displacement). This
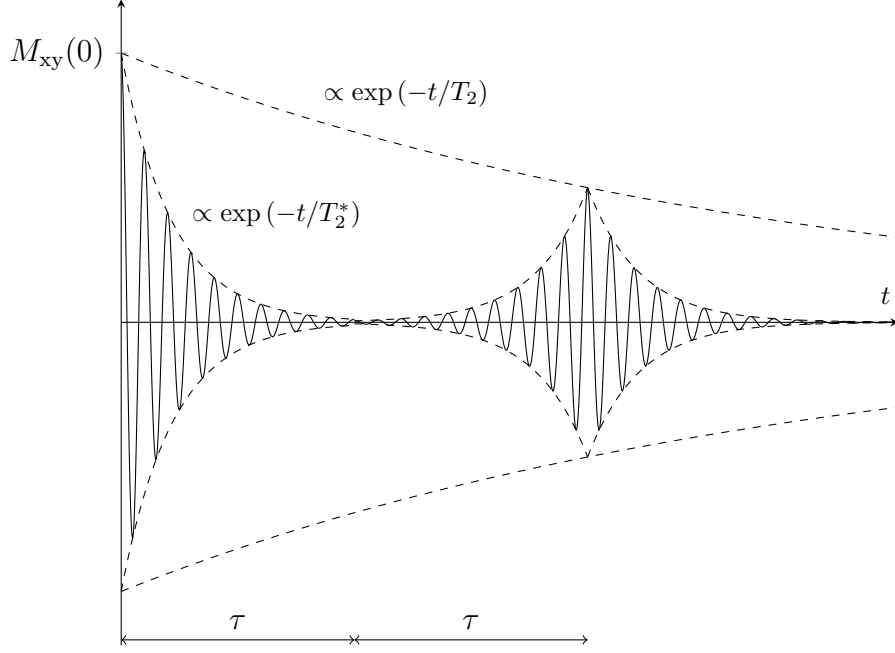
Figure 6: Formation of an SE. At $t = 0$, an excitation RF-pulse is applied to flip the magnetisation into the xy-plane. Dephasing of the spins leads to an exponential decrease of the amplitude of the FID. Due to inhomogeneities in the magnetic field, this decrease is not characterised by the relaxation time T_2, but the shorter T_2^*. After a time delay of τ, a 180° RF-pulse is applied to refocus the dephased spins. This dephasing process is completed after an additional τ and an SE is formed. The use of such a refocusing pulse reverses dephasing caused by T_2' effects. Thus, the signal decay is not determined by T_2^*, but by T_2.

technique enables 2D and 3D imaging, but also other properties of a system can be measured by using gradients. For example, properties such as diffusion, dispersion or velocity can be measured. In case of imaging, a gradient is applied, which generates a spatially dependent magnetic field. With respect to its strength G, the Larmor frequency is described by the fundamental equation of MRI

$$\omega_0(r) = \gamma(B_0 + \vec{G} \cdot \vec{r}) \tag{18}$$

where the spatial position is denoted as r. Gradients can be used in different ways to encode spatial informations. Three possibilities are explained in the following.

1.5.1 Slice selection gradient

The excitation and refocusing of the magnetisation can be limited to a slice, when a slice selection gradient is applied during the RF-pulses. The strength of the slice selection gradient G_{ss} determines the linear distribution of the magnetic field in the sample. The shape and duration of the RF-pulse determines the bandwidth $\Delta\omega_0$. In combination with G_{ss}, the slice thickness is defined:

$$\Delta r = \frac{\Delta\omega_0}{\gamma G_{ss}}. \tag{19}$$

7

For small flip angles, the frequency profile of an RF-pulse can be approximated by the FT of the RF-pulse shape in the time domain. For slice selection, usually the shape of a rectangle is used in the frequency domain. An ideal rectangular pulse is achieved for an infinitely long sinc pulse. However, a sinc pulse that can be generated in practice has finite duration and is obtained by truncating all but the central lobe and a few side lobes.

1.5.2 Frequency and phase gradients

Similar to slice selection, frequency- and phase-encoding is done for spatial encoding. The resonance frequency is varied along a spatial axis by the gradient, which generates a spatial and time dependent magnetic field. This gradient is applied for the time δ when no RF-pulses are applied.

For frequency encoding, the spatial encoding gradient is applied during the acquisition of the NMR signal. Regarding to eq. (18), the Larmor frequency of a spin isochromat can be assigned to its position. Applying the frequency encoding gradient G_f also causes a change of the signal phase:

$$\Phi(r) = r \cdot \gamma \int_0^\delta G_f(t) \, dt = 2\pi \cdot k \cdot r \tag{20}$$

Here, the k-space is defined as $k = \frac{\gamma}{2\pi} \int_0^\delta G(t) \, dt$. The corresponding NMR signal at a k-space point can be described by

$$S(k) = \int M_{xy}(r) \cdot e^{-i\Phi(r)} \, dr. \tag{21}$$

A prephase gradient is applied before the readout gradient to dephase the transverse magnetisation so that an echo signal can be created at a later time. The application of the readout gradient causes rephasing. When the readout gradient's area equals the area of the prephase gradient, an echo is formed.

Approximating the integral as a discrete sum using eq. (20) gives:

$$S(k) = \sum_{n=0}^{N-1} M_{xy}(r) \cdot e^{-2\pi \cdot n \cdot \Delta r \cdot k} \tag{22}$$

Here, Δr and N are the pixel size and the number of pixels. The signal can be Fourier transformed from the k-space into the spatial domain. The duration of data acquisition is determined as follows:

$$T_{acq} = \frac{N}{\Delta\nu} = \Delta t \cdot N \tag{23}$$

Here, $\Delta\nu$ is the receiver bandwidth, N is the number of k-space data points along the readout direction and Δt is the sampling interval (i.e. the delay between two adjacent k-space data points). Considering the Field Of View (FOV) along the readout direction, it is:

$$\Delta k = \frac{1}{N \cdot \Delta r} = \frac{1}{FOV} \tag{24}$$

Also, it can be written:

$$\Delta k = \frac{\gamma \cdot G_{\mathrm{f}} \cdot \Delta t}{2\pi} = \frac{\gamma \cdot G_{\mathrm{f}} \cdot T_{\mathrm{acq}}}{2\pi \cdot N} \tag{25}$$

Combining eqs. (23) to (25), we obtain:

$$G_{\mathrm{f}} = \frac{2\pi \cdot \Delta\nu}{\gamma \cdot \mathrm{FOV}} \tag{26}$$

This indicates that the higher the readout gradient, the smaller the FOV that can be achieved.

In contrast to frequency encoding, phase encoding gradients are not applied during, but before the signal is acquired. A phase change according to eq. (20) takes place. For repeating the acquisition N-times, where each time the phase encoding gradient has an increased strength, N values for k are generated. This provides sufficient information for $M_{xy} = f(n \cdot \Delta r)$ to be reconstructed. Commonly, the duration of G_{p} is kept constant and its amplitude is varied over the N repetitions to vary k_r. This method was firstly proposed in [36]. Usually, rewinding of the phase encoding gradient is done after the readout to rephase the transverse magnetisation and avoid artefacts in subsequent signal acquisitions.

1.5.3 Crusher and spoiler gradients

If an SE sequence has non-ideal refocusing pulses (flip angle $\alpha \neq 180°$), in addition to the SE signal other signal pathways (including FIDs and stimulated echoes) occur [37]. These may cause image artefacts, which can be eliminated by using crusher gradients [31]. Two crusher gradients of equal strength are applied in the same direction. The first crusher gradient is applied before and the second one is applied after the refocusing pulse. By manipulating the signal phase, the unwanted signal pathways are eliminated while the wanted ones are preserved.

Residual transverse magnetisation at the end of a sequence may also produce artefacts. These can be eliminate by using spoiler gradients, which are applied at the end of the sequence. They dephase the transverse magnetisation while the longitudinal magnetisation is preserved [31].

1.6 Magnetic Resonance Velocimetry

1.6.1 Phase contrast MRV

Flow velocities can be measured using Phase Contrast (PC) MRV. Here, velocity encoding gradients are applied, which cause a phase evolution of moving spins proportional to the velocity while for static spins the initial phase is retained after encoding. The phase Φ of the NMR signal is described by

$$\Phi = \Phi_0 + \gamma \cdot \vec{v} \cdot \vec{M_1} \tag{27}$$

where γ is the gyromagnetic ratio and $\vec{v}$ is the velocity. $\vec{M_1}$ is the first moment of the gradient applied for the duration T defined by:

$$\vec{M_1} = \int_0^T \vec{G}(t) \cdot t \, dt \tag{28}$$

Φ_0 results from background phase effects due to eddy currents, magnetic susceptibility and concomitant gradients. To filter out such effects for one-directional velocity, two measurements are done with different first moments $\vec{M}_1^{(1)}$ and $\vec{M}_1^{(2)}$ (e.g. using opposite gradient polarities) but under otherwise same conditions. Subtraction of the signal phases results in $\Delta\Phi$, which is dependent on velocity $\vec{v}$ and $\Delta\vec{M}_1 = \vec{M}_1^{(1)} - \vec{M}_1^{(2)}$. Thus, the velocity v along the gradient direction is determined as

$$v = \frac{\Delta\Phi}{\gamma \cdot \Delta M_1}. \tag{29}$$

The phase can only be uniquely measured from $-\pi$ to $+\pi$. For too high velocities, the velocity dependent phase shift can exceed $\pm\pi$ and phase aliasing occurs. The Velocity ENCoding (VENC) is thus defined as the velocity that produces a phase shift $\Delta\Phi = \pi$, i.e.

$$\text{VENC} = \frac{\pi}{\gamma \cdot \Delta M_1}. \tag{30}$$

The phase shift can be calculated as $\Delta\Phi = \arg(Z_1) - \arg(Z_2) = \Phi_1 - \Phi_2$, which is computationally costly because of two arg operations. Also, additional aliasings may be introduced. Instead, the phase shift is calculated by $\Delta\Phi = \arg(Z_1/Z_2) = \arg(Z_1 \cdot \bar{Z}_2)$ [31].

For the phase shift, eddy current errors originating from the velocity encoding gradients are not eliminated. Eddy currents depend on the direction of the applied gradients, making the eddy current error additive in the phase difference image [31]. If the object under investigation allows it, it is common to perform an additional measurement with the same parameters but without flow and subtract the phase images [38–40]. However, doing so, the Signal-to-Noise Ratio (SNR) (respectively Velocity-to-Noise Ratio (VNR)) is decreased by $\sqrt{2}$ because noise values of both measurements sum up. As an alternative, the influence of such errors can be reduced by fitting a polynomial to the no-flow dataset and subtract this from the flow dataset [41]. However, it must be considered that for an inaccurate fitting systematic errors may occur lowering the benefit of this technique.

Only velocities along the direction of the flow encoding gradients contribute to the encoded phase of the NMR signal. In case of three-directional velocity at least four encoding steps with gradients applied in different directions are needed. In this work the four-step balanced encoding (also called Hadamard encoding) was used [42]. Z_1 to Z_4 are the complex images acquired for individual encoding steps. The phases in x-, y- and z-direction are calculated as follows:

$$\Delta\Phi_{\text{x}} = \arg(\bar{Z}_1 \cdot Z_2 \cdot Z_3 \cdot \bar{Z}_4) \tag{31}$$
$$\Delta\Phi_{\text{y}} = \arg(\bar{Z}_1 \cdot Z_2 \cdot \bar{Z}_3 \cdot Z_4) \tag{32}$$
$$\Delta\Phi_{\text{z}} = \arg(\bar{Z}_1 \cdot \bar{Z}_2 \cdot Z_3 \cdot Z_4) \tag{33}$$

1.6.2 SNR and VNR

As described in [43] the standard deviation of the velocity is determined as

$$\sigma_v = \frac{\sqrt{N}}{\pi} \cdot \frac{\text{VENC}}{\text{SNR}} \tag{34}$$

where N is the number of encoding steps. For each voxel the SNR is calculated from the magnitude I of the complex signal and the standard deviation σ:

$$\text{SNR} = \frac{I}{\sigma} \tag{35}$$

For the results shown in this work, the standard deviation σ_0 is determined in the signal free part of the magnitude image. In magnitude images the noise distribution in regions without NMR signal is governed by a Rayleigh distribution [44]. Thus, the standard deviation σ, which is used to characterise the VNR, is given by $\sigma = 1.5264 \cdot \sigma_0$. The VNR is determined as described in [43, 45]:

$$\text{VNR} = \frac{v}{\sigma_v} \tag{36}$$

1.6.3 Dual-VENC

In eq. (34) it is visible that the VENC value should be set as low as possible to achieve a low noise value σ_v (i.e. good VNR). However, it must be noted that for $\text{VENC} < v_{\text{true}}$ aliasing occurs. For correction of the aliasing a reference scan with a higher VENC value is used and the difference $D = v_{\text{high}} - v_{\text{low}}$ is determined. The number of wrappings N is then determined as

$$N = \text{N.I.}\left(\frac{D}{2 \cdot \text{VENC}_{\text{low}}}\right) \tag{37}$$

where N.I. is the nearest integer function. The corrected (unwrapped) velocity is calculated as:

$$v_{\text{unwr}} = v + 2 \cdot N \cdot \text{VENC}_{\text{low}} \tag{38}$$

This dual-VENC method has already been widely used [43, 46–48]. In case of three-directional velocity measurements, an eight-step measurement can be done (four steps for a low- and four steps for a high-VENC measurement). This doubles the number of measurements in comparison to a single-VENC measurement but results in a VNR improvement by the factor

$$R = \frac{\text{VENC}_{\text{high}}}{\text{VENC}_{\text{low}}} = \frac{\sigma_{v-\text{high}}}{\sigma_{v-\text{low}}}. \tag{39}$$

It should be noted that for a large R unwrapping may fail due to large noise values in the difference D. Neglecting pulsation effects and assuming stable conditions (temperature, electrical components) during the whole measurement, the condition for a low number of wrong unwrappings can be written as described in [43]:

$$\text{noise}(D) < \text{VENC}_{\text{low}} \tag{40}$$

Regarding eq. (39) we formulate the noise value at each voxel by $\text{noise}(D) = m \cdot \sqrt{\frac{1}{R^2} + 1} \cdot \sigma_{v-\text{high}}$ where m is the number of standard deviations that can be tolerated. With eq. (34) it follows

$$m < \frac{\pi}{\sqrt{R^2 + 1} \cdot \sqrt{N}} \cdot \text{SNR} \tag{41}$$

For standard normal distribution the probability of a result outside of the interval $[-m \cdot \sigma; m \cdot \sigma]$ can be calculated by

$$P(x = m \cdot \sigma) = 1 - \int_{-x}^{x} f(x)\,dx = 1 - \mathrm{erf}(\frac{m}{\sqrt{2}}) \qquad (42)$$

where $f(x)$ is the probabilty density function and erf the Gaussian error function. For a given ratio R and SNR the fraction P of wrongly unwrapped voxels can be calculated with eqs. (41) and (42).

An additional VNR improvement is achieved by weighted averaging of the unwrapped low-VENC and the high-VENC maps:

$$\mathrm{VNR_{avg}} = \mathrm{VNR_{unwr}} \cdot \frac{\sqrt{1 + R^2}}{R} \qquad (43)$$

1.7 NMR Facilities

An NMR tomograph consists of different parts. A magnet generates the static magnetic field B_0, a gradient system generates the gradients, which are used to encode spatial or other informations of a sample. RF coils transmit and/or receive the NMR signals. Furthermore, there are the gradient and RF amplifiers, the digitizer for analog-to-digital conversion, and the console for controlling the scanner.

Figure 7: The MRI scanner BioSpec 70/20 USR and the unmounted birdcage coil.

In this work, all measurements were performed on a horizontal 7 T scanner (BioSpec 70/20 USR, Bruker BioSpin MRI, Ettlingen, Germany), which is equipped with a

114 mm bore gradient system (BGA 12S2, maximum gradient strength of 440 $\frac{mT}{m}$, maximum slew rate of 3440 $\frac{mT}{m \cdot ms}$). A horizontal 72-mm bore birdcage ^{1}H quadrature transceiver RF coil (Bruker BioSpin MRI, Ettlingen, Germany) was used in all measurements. The scanner is located in a separate, air-conditions room. A picture of the scanner is shown in fig. 7. The console is a Linux workstation with ParaVision 5.1, in which pulse sequence programming, measurements and online image reconstruction can be performed.

2 Introduction to fluid flow in porous media

2.1 Flow patterns

For the movement of fluids, a distinction is made between laminar and turbulent flow. Laminar flow is a smooth fluid motion, for which in a transition area between two different velocities no vortices or secondary flows occur. Thus, the fluid flows in layers, which do not mix. If the vectorial flow velocity is independent of time at every point in the flow field, this is called steady flow [49, 50].

Turbulent flow is fluid motion characterised by chaotic changes in pressure and flow

laminar flow
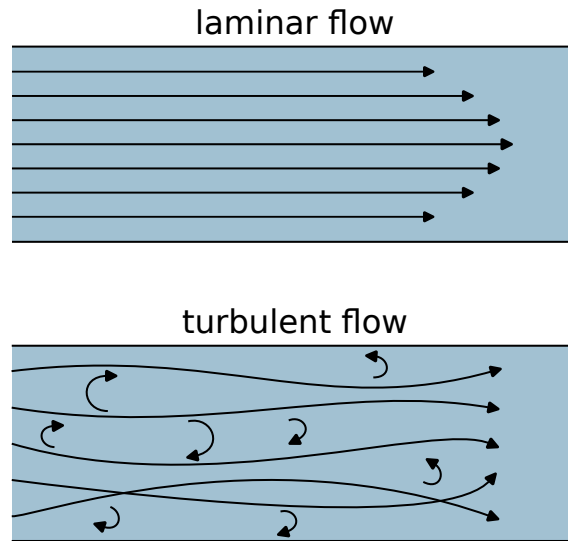
turbulent flow

Figure 8: For laminar flow, the fluid moves in layers. In contrast, for turbulent flow chaotic eddies, vortices and other instabilities occur.

velocity. Chaotic eddies and other flow instabilities are produced. Since turbulent flows are unsteady in time, they can only be measured to a limited extent by MRI. Ultrafast measurement techniques are necessary (usually 2D imaging). Suitable sequences were presented in different works [51–55]. In contrast, 3D measurements, which usually have much longer acquisition duration, are only suitable to measure steady laminar flow.

Laminar and turbulent flow are distinguished by the Reynolds number Re, which is the ratio of inertial forces to viscous forces within a fluid that is subjected to relative internal movement. The Reynolds number is defined by:

$$Re = \frac{v \cdot l}{\nu_\mathrm{f}} = \frac{v \cdot l \cdot \rho_\mathrm{f}}{\mu_\mathrm{f}} \tag{44}$$

Here, v is the flow velocity, l a characteristic linear dimension, ν_f the kinematic viscosity, ρ_f the density of the fluid and μ_f the dynamic viscosity. For tubular flow, usually the inner diameter D_in is used as the characteristic dimension and the axial velocity v_z:

$$Re = \frac{v_\mathrm{z} \cdot D_\mathrm{in} \cdot \rho_\mathrm{f}}{\mu_\mathrm{f}} \tag{45}$$

Below the critical value Re_{crit} (viscous forces are dominant) laminar flow is present. Above Re_{crit} (inertial forces are dominant) the laminar flow becomes unstable to small disturbances and one speaks of turbulent flow. Re_{crit} depends on the geometry of the object through which the fluid is flowing. For tubular flow, it is $Re_{\text{crit}} \approx 2300$ [50, 56]. Here, the characteristic linear dimension is described by the tube diameter and for v the mean flow velocity is used. The difference between both flow patterns is schematically shown in fig. 8.

The Mach number describes the ratio between the flow velocity and the speed of sound c of the fluid and is a parameter to distinguish between compressible and incompressible flows.

$$\text{Ma} = \frac{v}{c} \tag{46}$$

The major difference between compressible and incompressible flows is that in the former the fluid density varies throughout the flow, whereas in the latter it is constant. For $\text{Ma} < 0.3$, compressibility effects of the fluid can be neglected and the flow is characterised as incompressible [49]. For water, it is $c \approx 1400 \, \frac{\text{m}}{\text{s}}$ [50] and $\text{Ma} = 0.3$ is achieved for $v \approx 420 \, \frac{\text{m}}{\text{s}}$. In this work, for all measurements the flow velocity was much lower (maximum velocities up to a few $\frac{\text{cm}}{\text{s}}$) and incompressibility could be assumed for water flow.

When a flow enters a tube, it has to travel a certain distance until the effects from the inner wall have affected the flow in such a way that the laminar flow becomes fully developed. This distance is characterised by the entrance length L_{e} [50]:

$$L_{\text{e}} = 0.056 \cdot Re \cdot D_{\text{in}} \tag{47}$$

Here, D_{in} is the inner diameter of the tube.

2.2 Porous media

Catalysts are one of the most important elements in chemical and petrochemical industry as well as other sectors. Catalysis accelerates, e.g., the production of chemicals [57] or is used for reducing pollution and waste [58–60]. Examples for prominent catalytic reactions are the Haber-Bosch synthesis of ammonia [61] or the Fischer-Tropsch process for the synthesis of carbon monoxide and hydrogen to hydrocarbons [62].

In chemical industry, pellets and extrudates are widely used as catalyst supports, which are loosely packed in a reactor [63]. In contrast to such packed beds, alternative types of catalyst supports are monolithic solid Open Cell Foams (OCFs) or honeycomb structures. Their high porosity provides low pressure drop along the catalyst support compared to packed beds [64–67] resulting in savings in energy efficiency and low-contact-time operation. Additionally, the high Specific Surface Area (SSA) leads to higher efficiency for catalytic processes that otherwise require large pellets [65, 68, 69]. Furthermore, a high thermal transport is enabled due to thermal conductivity in the continuos solid phase [64, 65]. In contrast to honeycombs, OCFs also have the benefit that they enable a radial convection, which additionally improves the heat transfer. Thus, better reactor stability is enabled for highly exothermic reactions [68, 69]. In addition, the mixing of the fluid in the OCF
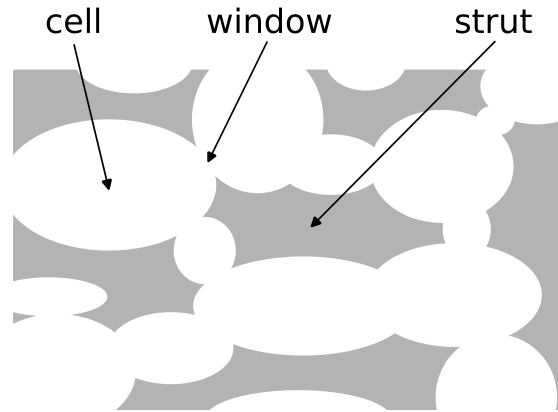
Figure 9: Different regions of an OCF are depicted.

is improved, which increases the heat and mass transfer between liquid and solid phase at the interface.

For foams, a distinction is made between closed and open cell. Closed Cell Foams (CCFs) are composed of polyhedra-like cells connected by solid faces. Thus, no interconnectivity between pores is present. In contrast, OCFs have solid edges and open faces [65]. A fluid can flow from one to another cell. OCFs can be divided into three regions, as depicted in fig. 9: The skeletal portion of the medium is called strut. Cells are approximately spherical voids enclosed by the struts. Windows are openings connecting the cells to each other.

OCFs have a sponge-like structure, which can be seen in fig. 10. Typically, pore
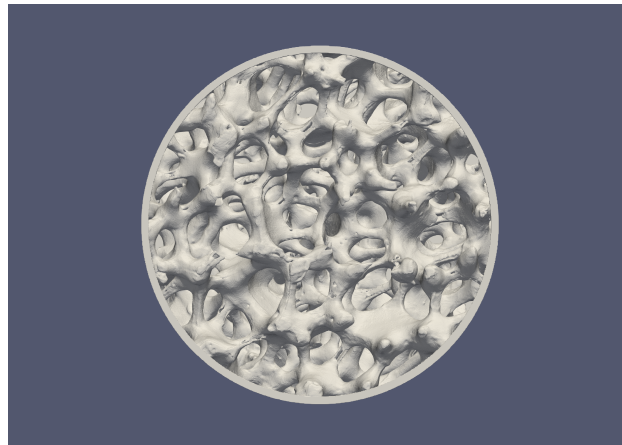
Figure 10: Axial view on a 10 PPI OCF structure. The three-dimensional image of this structure was generated by μCT. Visualisation was done by using the software ParaView.

densities range between 10 and 100 PPI and porosities between 0.75 and 0.9 [65,66]. Parameters to characterise an OCF structure are the pore density in PPI, the pore size diameter d_{p}, window size d_{w}, porosity ϵ (the fraction of the pore volume between the solid struts), the bulk density ρ_{B} (mass per unit volume of foam) and SSA S_{V} (geometric surface area per unit volume of solid).

For the calculation of the pore-Reynolds number Re_{p}, in case of OCF structures the pore size d_{p} is substituted for the characteristic linear dimension:

$$Re_{\mathrm{p}} = \frac{v \cdot d_{\mathrm{p}} \cdot \rho}{\mu} \tag{48}$$

2.3 Numerical Simulations

In situ analysis of fluid flow through porous media offers not only a characterisation of the flow behaviour but also the possibility to validate numerical simulations. In general, numerical simulations help to minimise costs by providing a higher degree of flexibility using adequate computational power, when the appropriate numerical setup is implemented. Thus, these techniques are widely used for industrial applications. In contrast, experimental measurement techniques (like MRI) cause much larger costs and effort. Simulations are based on mathematical models, which are approximations of real-world systems, and these models may not accurately represent all of the physical phenomena present in a system. In addition, numerical errors (such as discretisation errors) may occur. Therefore, measurements are necessary for cross-validation. Due to its flexibility in measuring different properties and different fluids, MRI is a powerful measurement technique for analysing fluid flow.
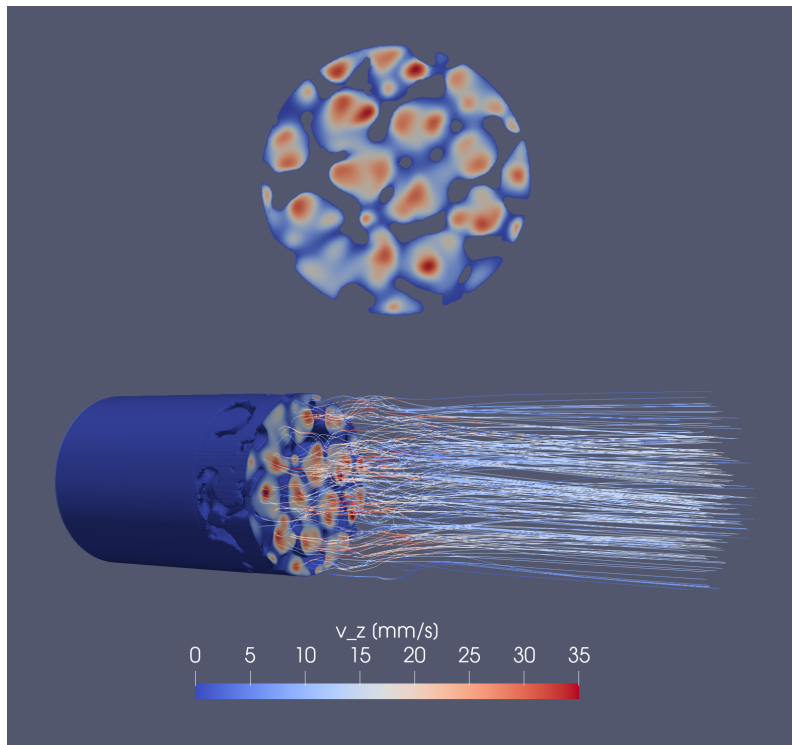
Figure 11: A CFD simulation was done for water flowing through a 10 PPI OCF structure. Velocity map for the axial velocity is shown. Streamlines were calculated by using the software Paraview.

In Computational Fluid Dynamics (CFD) simulations, a system of equations is solved, including the momentum balancing Navier-Stokes equations and a mass balancing

continuity equation. The continuity equation states that the rate at which mass enters a system is equal to the rate at which mass leaves the system plus the accumulation of mass within the system. This equation is written as follows:

$$\frac{\partial \rho}{\partial t} + \nabla \cdot (\rho \cdot v) = 0 \tag{49}$$

Here, ρ is the fluid density, t the time and v the fluid velocity.

The Navier-Stokes equation in the narrower sense is the momentum theorem as an application of Newton's axioms to a continuum. A form used for compressible fluids is

$$\rho \frac{\mathrm{D}\vec{v}}{\mathrm{D}t} = \rho(\frac{\partial \vec{v}}{\partial t} + (\vec{v} \cdot \nabla)\vec{v}) = -\nabla p + \mu \Delta \vec{v} + (\lambda + \mu)\nabla(\nabla \cdot \vec{v}) + \vec{f} \tag{50}$$

with the volume viscosity λ and the body force $\vec{f}$. Δ and ∇ are the Laplace operator and the nabla operator, respectively. If the density of the fluid does not change along the particle path, the flow is called incompressible and the continuity equation simplifies to $\nabla \cdot \vec{v} = 0$ and the Navier-Stokes equation to:

$$\rho(\frac{\partial \vec{v}}{\partial t} + (\vec{v} \cdot \nabla)\vec{v}) = -\nabla p + \mu \Delta \vec{v} + \vec{f} \tag{51}$$

The simulation was done by using the software OpenFOAM. Exemplarily, the simulated axial velocity field of water flowing through a 10 PPI OCF structure is shown in fig. 11. Further details are given in section 6.3.

3 Setup

3.1 Samples and flow setup

For all flow measurements, tap water was used as fluid. Three different samples were used: (1) A flow phantom, (2) an OCF structure and (3) a honeycomb structure. (1) The flow phantom was manufactured in the university workshop by heating and turning a glass tube (inner diameter (5 ± 0.15) mm) in helical shape. Since more heat was added from one side during the manufacturing process, the helix is flattened on the outside of the windings. Also the cross-section was narrowed. The cross-section is decreased by 32% in comparison to the straight section (this value was determined on the basis of the 3D MRI data). A picture of the flow phantom is shown in fig. 12.
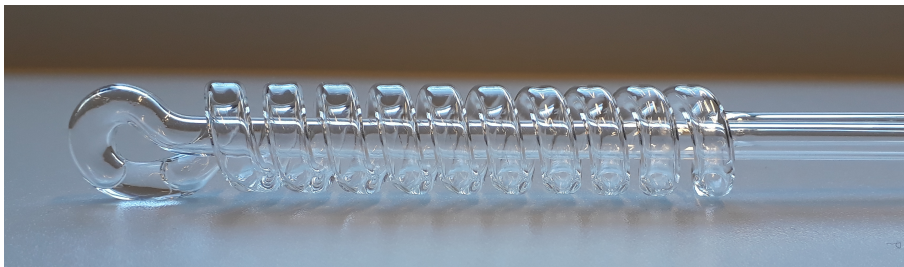
Figure 12: Photo of the flow phantom. The tube is round in the straight section but flattened on the outside at the windings, which come about due to the manufacture process.

(2) The 10 PPI OCF structure (25 mm in diameter) consists of PolyLacticAcid (PLA) and was 3D-printed by a Digital Light Processing printer (Elegoo Mars, Shenzhen, China) with 2 k resolution ($12.5\,\mu$m $\times$ $12.5\,\mu$m) in XY direction and layer height (Z) of $50\,\mu$m. To prevent unwanted bypass flow, seal tape was wrapped

Figure 13: From the stl-file shown in fig. 10, an OCF structure was 3D-printed of PLA and used for the measurements. For details, see table 1.

around the OCF before it was pushed into the glass vessel. The properties of the

OCF are given in table 1.

No-flow measurements were performed to determine the relaxation times T_1 and T_2. Using a single-SE imaging sequence, the same axial 2D slice inside the OCF was acquired for different values of T_R. The signal magnitude was determined for a Region Of Interest (ROI) inside the OCF and is plotted in fig. 14. Fitting the data
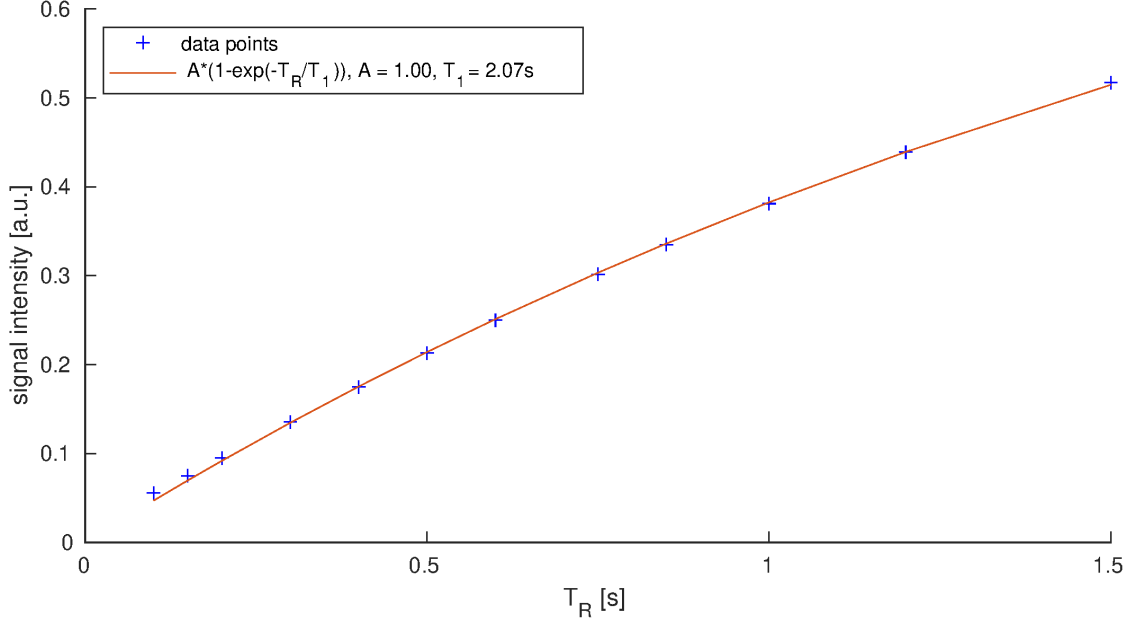
Figure 14: The signal magnitude inside the OCF structure was determined for different repetition times T_R. By fitting, the relaxation time T_1 was determined.

with

$$A \cdot (1 - \exp(T_R/T_1))$$

results in $T_1 = 2.07\,\mathrm{s}$. With a multi-SE imaging sequence, for each echo the same axial slice was acquired. The time interval between two consecutive echoes was $\Delta T_E = 12\,\mathrm{ms}$. The signal magnitude was determined for a ROI inside the OCF and the decrease of the transverse magnetisation for the later echoes can be observed (see fig. 15). Fitting to

$$A \cdot \exp(-t/T_2)$$

results in $T_2 = 0.41\,\mathrm{s}$.

(3) A honeycomb structure (3D printed of PLA) with a channel size of 2.4 mm and a wall thickness between two channels of 0.8 mm was used (fig. 16). The usage of seal tape (as described for the OCF) prevented bypass flow.

To cover similar velocity ranges, flow rates of $9.9 \pm 0.1\,\frac{\mathrm{ml}}{\mathrm{min}}$ (flow phantom), $206 \pm 2\,\frac{\mathrm{ml}}{\mathrm{min}}$ (OCF) and $200 \pm 2\,\frac{\mathrm{ml}}{\mathrm{min}}$ (honeycomb) were realised using a peristaltic pump (Standard Digital Drive with Easy-Load II Pump Head; Masterflex, Vernon Hills, USA) with pulse dampener and pump tubing also from Masterflex. PVC-tubing was used for connection to the flow phantom and the glass vessel with the OCF or honeycomb (fig. 17). Tap water was used as the operating fluid since this is widely used as flow model for MRV measurements. The average inlet velocity v_z was calculated depending on the Volumetric Flow Rate (VFR). Reynolds numbers were determined
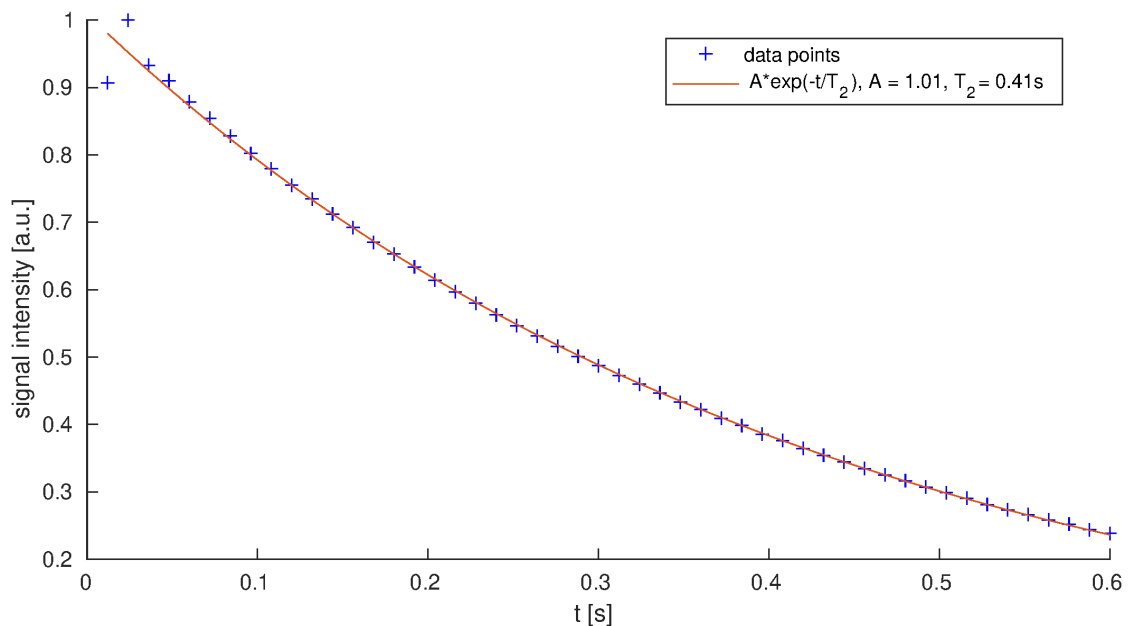
Figure 15: The signal magnitude inside the OCF structure was determined for the consecutive echoes. By fitting, the relaxation time T_2 was determined.

Table 1: Morphological properties of the OCF with 10 pores per inch.

Parameter	Value
Open porosity	0.77
Pore diameter[1]	5.8 ± 1.9
Window diameter[1]	3.3 ± 0.9
Specific surface area[2]	521.3

[1]in mm

[2]in $m^2 m^{-3}$

according to eq. (45): $Re = 42$ (flow phantom), $Re = 175$ (glass vessel with OCF), and $Re = 169$ (glass vessel with honeycomb). Entrance length (eq. (47)) was $L_e = 12\,mm$ (flow phantom), $L_e = 245\,mm$ (OCF), and $L_e = 237\,mm$ (honeycomb). The straight inlet of the flow phantom had a length of $180\,mm$. The total length of the glass vessel, in which the OCF or honeycomb was located, was $445\,mm$. The samples were not positioned in the middle of the glass vessel but at a length of about $300\,mm$. Since for all three samples the straight inlet was longer than the entrance length, fully developed laminar flow can be assumed.

For calculating the pore-Re number, the mean pore diameter $5.8\,mm$ (table 1) was used instead of the tube diameter. Since it is difficult to estimate the average velocity in a pore, the high-VENC was chosen for u_z leading to a pore-Re of 261. Therefore, laminar flow can be assumed for all samples since the critical Reynolds number is given as $Re_{crit} \approx 2300$ [50, 56].

Figure 16: A honeycomb structure made of PLA used for the measurements.
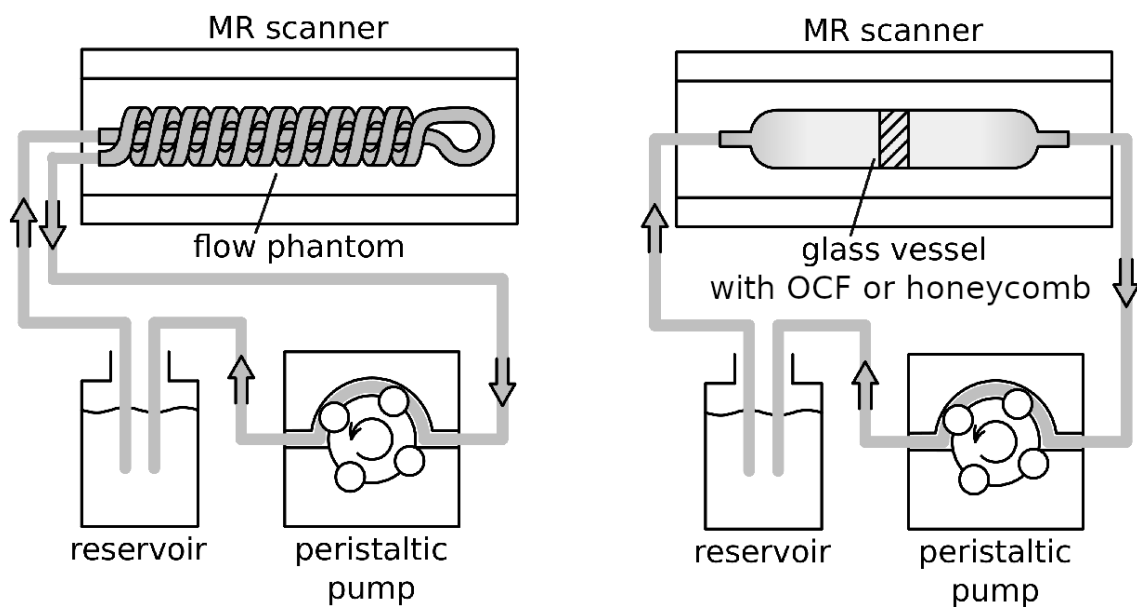
Figure 17: Schematic of the setup. To minimise pulsation effects, a pulse dampener was used (not shown).

4 Multi-echo MRV sequence

4.1 Introduction

Understanding transport phenomena within monolithic catalyst carriers requires numerical and experimental tools. Morphological properties of monolithic catalysts such as OCF and honeycomb structures control the transport phenomena and have a considerable influence on the performance of the reactive system [70]. Generally, OCFs and honeycombs are classified based on the number of PPI or number of Channels Per Inch (CPI). The structure of OCFs is determined by their pore size, window size, porosity and SSA, while the morphology of honeycomb monoliths is determined by the channel size and wall thickness between two channels. For measuring flow velocity, different methods are used like Laser Doppler Velocimetry (LDV), Particle Image Velocimetry (PIV), or Planar Laser Induced Fluorescence (PLIF) [71–74], which need optical access to the fluid. A non-optical technique is Positron Emission Particle Tracking (PEPT), where positron emitting particles are added to the fluid [75]. The benefit of non-invasive and non-optical PC-MRV is that, without adding any tracer particles, the three-directional velocity of a fluid in opaque structures can be measured with three-dimensional spatial resolution. Therefore, PC-MRV is widely used in medical application, for example to measure cerebral [76, 77] and aortic [78–82] blood flow and cerebrospinal fluid pulsation [83–85]. PC-MRV is also an important tool to analyse flow velocity in engineering applications like porous media [20, 22, 25, 40, 86–88]. Velocity fields are measured by encoding the signal phase of moving spins [78, 89]. For measuring one-directional velocity typically two steps are done with velocity encoding gradients applied in opposite direction. This is done to subtract phase errors originating, e.g., from B_0 inhomogeneities or eddy currents and to suppress unwanted phase variation in stationary regions [31]. Three-directional velocity encoding is realised by using at least four steps with flow encoding gradients applied in different spatial directions. A simple four-step encoding scheme uses a single reference scan with velocity encoding gradients set to zero and three scans with velocity encoding gradients applied in x-, y- or z-direction [90]. Alternatively, a balanced four-step encoding scheme (also called Hadamard encoding) can be used where the direction of the flow encoding gradients is altered in pairs for each step [91]. Details about the encoding steps are given in table 2. By linear combination of the four datasets the velocity components in x-, y- and z-direction are reconstructed (see eqs. (31) to (33)). A comparison of the different flow encoding schemes can be found in [42, 92, 93]. In [42], it was shown that simple and balanced four-step encoding have the same average noise performance. However, in contrast to the simple scheme, the noise in the measured velocity components is uncorrelated and velocity encoding for the same dynamic range is achieved with lower gradient strength.

One challenge is the optimal choice of the VENC, which determines the velocity range that can be uniquely assigned. In systems with a wide range of velocities, single-VENC measurements result either in aliasing for fast flow or a low VNR for slow flow. In the past years, several aliasing-correction algorithms were presented [94–98]. However, such numerical algorithms may fail for many wrappings or for small pores, which is a problem for analysing porous media. Unwrapping

techniques can also be realised by measuring additional encoding steps. In [43] the two-step encoding (one-directional velocity) was expanded by adding an extra step such that a higher VENC-value was achieved. This step was used to unwrap the aliased low-VENC data and therefore improvement of the VNR was achieved. A similar dual-VENC technique was used for three-directional velocity [46–48, 99].

In clinical application it is of central interest to keep the measurement time short to reduce costs, avoid patient discomfort and minimise blurring of the images caused by movements (e.g. breathing). Due to their shorter measurement time, gradient-echo sequences with small flip angles and short repetition time T_{R} are the common choice for in-vivo measurements. Also they allow a low specific absorption rate (heating of tissue) [100, 101]. However, a disadvantage of this technique is the dependence on T_2' and thus the susceptibility to magnetic field inhomogeneities. The advantage of SE sequences is their independence of T_2' and therefore better image quality is achieved in case of magnetic field inhomogeneities. Thus, SE sequences [31, 102, 103] are a good choice for measuring flow velocity in porous media [20, 25, 40, 86, 87, 104].

Eddy currents depend on the strength and direction of the applied gradient. Thus, phase errors originating from the velocity encoding gradients do not subtract completely in the phase difference image and cause a spatial dependent offset [31]. To correct such offsets, an additional measurement with same parameters but without flow can be done [38–40, 54, 105]. The offset can be corrected by directly subtracting the phase values of the no-flow dataset voxel-wise.

Flow through porous media like OCFs, which have different sized pores, usually has large differences between slow and fast flow regions. For both, slow and fast velocities, there are characteristic problems that lower the accuracy of measured velocity fields. This is especially disadvantageous if MRV measurements are used for cross-validation with CFD simulations. Slow flow regions, which are especially located at the pore surface, are often negatively influenced by partial volume effects [30] while displacement errors have a negative effect on fast flow regions. Displacement errors may occur because the fluid moves between encoding events, in particular if the delay between spatial encoding and velocity encoding is long. Thus, velocity values would be assigned to wrong positions [27–29, 39]. To reduce this effect, the voxel size of the measurement and timings of the sequence should be adjusted to occurring velocities. In [106] a single-point PC sequence was proposed to minimise displacement errors. However, the point-wise acquisition leads to long acquisition times and is therefore impractical for 3D imaging with a large matrix size.

In [87] a Rapid Acquisition with Relaxation Enhancement (RARE)-PC-MRV sequence was presented for reduced measurement time. After one excitation pulse several echoes are acquired. Because of displacement errors this sequence is limited to slow flow velocities. To reduce the displacement effect, the FLow Imaging Employing Single-Shot ENcoding (FLIESSEN) sequence was proposed, which is a single-shot multi-echo sequence with velocity encoding and decoding for each echo [107].

The objective of the present work was to describe techniques to reduce artefacts and increase the accuracy of MRV measurements for porous media using water flow through an OCF as an example. To reduce measurement time, a multi-echo sequence was designed where each echo pair experiences a different velocity encoding.

Thus, per excitation pulse for one line in k-space [108] a whole eight-step dual-VENC balanced encoding is done. For minimising artefacts in the fast flow regions, such as displacement errors, timings of the sequence and voxel size were carefully chosen. To improve accuracy in slow flow regions and minimising aliasing problems in fast flow regions, a dual-VENC method was used.

4.2 MRV sequence

A SE and PC-based MRV pulse sequence was implemented (fig. 18). Spatial res-
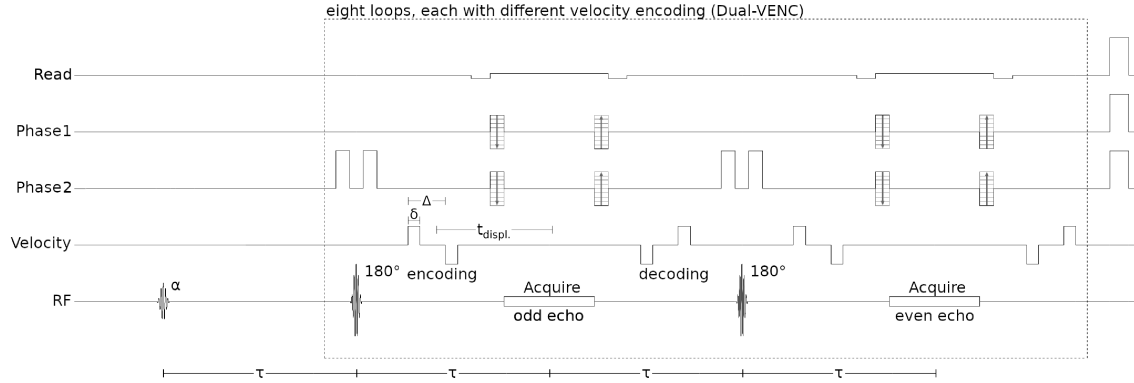
Figure 18: Scheme of the 16-echo MRV sequence: An excitation pulse is applied with flip angle $\alpha = 90°$. In eight loops (dotted rectangle) different velocity encoding gradients are applied for achieving a full dual-VENC encoding scheme. For each loop, odd and even echoes are acquired and averaged in post-processing to correct for offsets introduced by different phase coherence pathways. Spatial encoding is done by gradients in read-, phase1- and phase2-direction. Velocity encoding gradients with duration δ and time delay Δ are applied. Spins are refocused by using 180° pulses after duration τ. SE is acquired after an additional τ.

olution was achieved by one read and two phase encoding gradients. The spatial encoding by the readout and phase encoding gradients was sufficient to avoid signal wrap-around for the measured samples and the chosen FOV. Therefore, non-selective rectangular RF-pulses were used for excitation and refocusing to reduce the interecho delay and avoid signal losses. To eliminate unwanted magnetisation in order to remove image artefacts, crusher gradients were applied before and after the refocusing pulses. Additionally, spoiler gradients were used at the end of the sequence (for details, see section 1.5.3). In [87, 105], the velocity encoding was done before the multi-echo loop. However, in this case measurements are limited to slow velocities. Otherwise large displacement errors would arise for the later echoes. To avoid this, in the proposed sequence velocity encoding was done similar to the FLIESSEN sequence [107]. Before and after each echo, pairs of velocity encoding gradients, i.e. gradient pulses with same strength but opposite direction, were applied to set the phase shift to zero before the next RF refocusing pulse. This increases the echo time but reduces displacement effects. For the FLIESSEN sequence, different positions in k-space are acquired for consecutive echoes. This results in a reduced spatial resolution in phase encoding directions. In the proposed sequence, this effect

was avoided since for each echo train one position in k-space was acquired. In total eight different velocity encoding gradients were applied to achieve a full dual-VENC encoding scheme for acquisition of three-directional velocity in one measurement. For every echo pair consisting of two consecutive echoes (odd and even) the same velocity encoding was done. Datasets from odd and even echoes were combined to

Table 2: Encoding steps (dual-VENC balanced encoding scheme) for the echo pairs. The factors a and b are set depending on $VENC_1$ and $VENC_2$.

Echo pair	M_1^x	M_1^y	M_1^z
1	$-a$	$-a$	$-a$
2	$+a$	$+a$	$-a$
3	$+a$	$-a$	$+a$
4	$-a$	$+a$	$+a$
5	$-b$	$-b$	$-b$
6	$+b$	$+b$	$-b$
7	$+b$	$-b$	$+b$
8	$-b$	$+b$	$+b$

suppress additional phase differences caused by different coherence pathways (for details see [87, 105, 109]). Between velocity encoding and decoding, spins may be accelerated or decelerated (e.g., for spins moving near a narrowing). In this case the signal phase imposed by the velocity encoding gradients is not completely eliminated after decoding and an acceleration-dependent phase shift remains. Combination of odd and even echoes cancels this effect [107], provided that the acceleration remains constant for both echoes. The velocity with $VENC_{low}$ was reconstructed from the first eight echoes and the velocity with $VENC_{high}$ was reconstructed from the last eight echoes. Associated velocities are called v_1 and v_2. Hence, in total 16 echoes were acquired. As discussed in [39], the maximum displacement in number of voxels is given by

$$displacement \approx v_{\max} \cdot \frac{t_{\mathrm{displ}}}{voxel\ size} \tag{52}$$

where t_{displ} is the time between the centre of velocity encoding and the centre of the following acquisition. Even though t_{displ} should be chosen as short as possible it shall be noted that the gradient amplitude is limited and therefore for a given VENC the duration δ and delay Δ cannot be chosen arbitrarily short. Since gradients with large amplitude may produce eddy currents which worsen the image quality, these should only be applied if compensation is provided to correct for eddy currents. If the compensation is not perfect, which is usually the case for experimental data, the remaining artefacts scale with the gradient amplitude. Additionally, performing measurements with large gradient amplitude may shorten the lifespan of the gradient system. Using $\tau = 6.0\,\mathrm{ms}$, a duration of $192\,\mathrm{ms}$ results from excitation

pulse until acquisition of the last of the 16 echoes. Experimentally, a transverse relaxation time $T_2 = 0.41\,\text{s}$ was determined for the water filled OCF structure (see section 3.1). Thus, due to transverse relaxation the SNR of the last echo was reduced by $36.5\,\%$ in comparison to the first echo. The SNR of the final (unwrapped) velocity map is mainly determined by the VENC_{low}. Therefore, the $\text{VENC}_{\text{high}}$ encoding steps were measured in the last eight echoes. Using additional dedicated gradients, flow-induced signal loss can be reduced [110–112]. However, in the proposed sequence, flow compensating gradients were not used for spatial encoding since this would increase the echo time of the sequence. Additionally, this would increase the displacement error. For the chosen flow rates, the signal loss due to missing flow compensation gradients was negligible (about $2\,\%$ for the flow phantom and $3\,\%$ for the OCF). For details, see sections 4.5 and 4.6.1. In the current implementation of the pulse sequence the following parameters were used: The acquisition time per echo was $1.5\,\text{ms}$. Flow encoding gradients had a duration of $\delta = 0.78\,\text{ms}$ and a delay of $\Delta = 2.71\,\text{ms}$. The time between the centre of velocity encoding and the centre of acquisition was $t_{\text{displ}} = 3.58\,\text{ms}$. It should be noted that this value may differ for other implementations or applications, since it depends on several factors (hardware, acquisition time, voxel size, VENC, flow velocity, etc.).

4.3 Optimised repetition time

For a given sequence the SNR can be improved by increasing the number of accumulations or increasing the repetition time T_{R}. For a constant measurement time it shall be analysed at which ratio between the number of accumulations and T_{R} the optimal SNR improvement is achieved. Therefore, the longitudinal magnetisation is considered. After applying the $90°$ excitation pulse at $t_0 = 0$ the longitudinal mag-
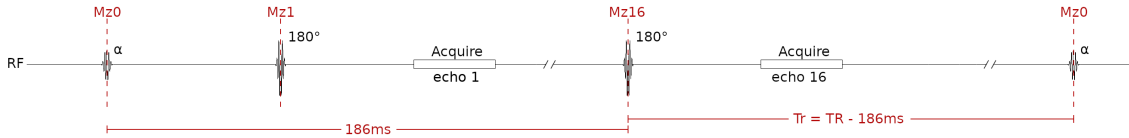
Figure 19: Echo train with longitudinal magnetisation at specific times.

netisation is $M_{\text{z0}} = M_{\text{z}}(t_0) = 0$. Due to longitudinal relaxation the magnetisation after applying the first $180°$ pulse (at t_1) is

$$M_{\text{z1}} = -(M_0 - (M_0 - M_{\text{z0}}) \cdot e^{-6\,\text{ms}/T_1}). \tag{53}$$

In total sixteen $180°$-pulses are applied in the echo train. The longitudinal magnetisation directly after the k-th inversion pulse is calculated as follows:

$$M_{\text{z}k+1} = -(M_0 - (M_0 - M_{\text{z}k}) \cdot e^{-12\,\text{ms}/T_1}) \qquad \text{with} \qquad k = 1, ..., 15 \tag{54}$$

For $T_1 = 2\,\text{s}$, which was experimentally determined for the water filled OCF structure (see section 3.1), a quite low $M_{\text{z16}} = -0.003 \cdot M_0$ results. Therefore, M_{z16} is neglected in the following. We consider the time between the last inversion pulse

and the excitation pulse where longitudinal relaxation takes place. With $M_0 = 1$ and normalisation to unit time, the longitudinal magnetisation is approximated by

$$M_t^z = (1 - e^{-(T_\mathrm{R} - 186\,\mathrm{ms})/T_1}) \cdot \frac{1}{\sqrt{T_\mathrm{R}}}. \tag{55}$$

Plots for eq. (55) at different T_1 values are shown in fig. 20. For long T_1 a broad

Figure 20: Simulation is done based on eq. (55). For $T_\mathrm{R} = 1\,\mathrm{s}, 2\,\mathrm{s}, 3\,\mathrm{s}$ maxima are at $1.6\,\mathrm{s}, 2.9\,\mathrm{s}, 4.2\,\mathrm{s}$.

maximum is visible. However, an optimal T_R value should be chosen to avoid SNR losses, which is of particular importance for short T_1.

4.4 Measurement parameters

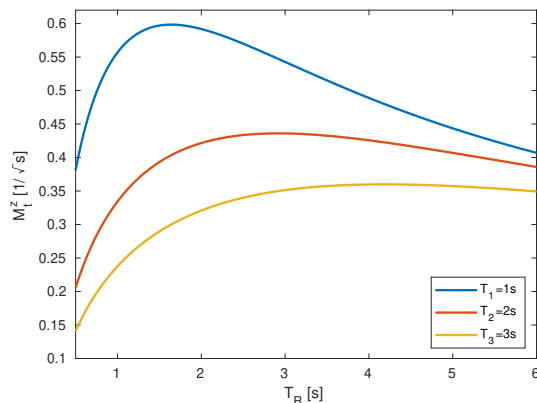The repetition time was $T_\mathrm{R} = 2.9\,\mathrm{s}$ (according to the maximum in fig. 20). The amplitude of the flow encoding gradients was set depending on the desired VENC value. Further measurement parameters are listed in table 3. The measurements

Table 3: Parameters for the measurements of the flow phantom (1) and the OCF (2). For improved SNR, measurements were averaged n-times. Total measurement time is calculated for the pump switched on and off.

	Matrix size	FOV [mm^3]	Voxel size [mm]	VENC$_1$ [$\frac{\mathrm{mm}}{\mathrm{s}}$]	VENC$_2$ [$\frac{\mathrm{mm}}{\mathrm{s}}$]	n_avg	Meas. time [h]
(1)	$120 \times 80 \times 80$	$36 \times 24 \times 24$	0.30	40	40	1	10.3
(2)	$80 \times 80 \times 80$	$36 \times 36 \times 36$	0.45	20	45	2	20.6

for the flow phantom were done at $\mathrm{VENC}_1 = \mathrm{VENC}_2 = 40\,\frac{\mathrm{mm}}{\mathrm{s}}$ to analyse the reproducibility of the measured velocity v_1 and v_2. For improving the VNR, the dual-VENC method was used for the OCF. VENC values were $\mathrm{VENC}_1 = 20\,\frac{\mathrm{mm}}{\mathrm{s}}$ and $\mathrm{VENC}_2 = 45\,\frac{\mathrm{mm}}{\mathrm{s}}$. The final (unwrapped) velocity is mainly determined by the VNR of the low-VENC data. Thus, the low-VENC value was chosen for VENC_1

because the first echoes experience a lower SNR loss (respectively VNR loss) due to transverse relaxation. Measurements were performed with and without flow. Considering the no-flow data, noise parameters were determined for the high-VENC data (last eight echoes) after averaging the two accumulations. For each pair of consecutive odd and even echo the magnitude images were combined (averaging) and the respective SNR was calculated according to eq. (35). The mean value was SNR = 199.6, which was used to calculate $\sigma_v = 0.144 \frac{\text{mm}}{\text{s}}$ (eq. (34), number of encoding steps $N = 4$). Post-processing of the data was performed using a self-developed MATLAB script (R2021a MathWorks, Natick, MA, USA). Binary masking was based on Otsu's thresholding [113] for the corresponding magnitude images. This was done to distinguish the OCF (respectively flow phantom) from the noisy background.

4.5 Results

4.5.1 Flow phantom

In figs. 21 to 26 the velocity maps for axial slice 61 (out of 120) of the flow phantom are shown. For the maps without flow an offset is visible (depending on the spatial position up to 12 % of the VENC). For other slices of the 3D velocity map, even larger offsets could be determined (up to 57 % of the VENC). For a quantitative analysis for each of the v_z maps, the VFR was calculated in a ROI (straight tube) by

$$\text{VFR}_z(z) = L_x \cdot L_y \cdot \sum_{x,y} v_z(x, y, z) \tag{56}$$

where L_x and L_y are the voxel size in x- and y-direction. The bar plot with the resulting VFR for v_1^z and v_2^z is shown in fig. 27.

For all cases without offset correction (odd, even, combined) the VFR is between 12 and 14 $\frac{\text{ml}}{\text{min}}$ and therefore does not fit the expected $9.9 \pm 0.1 \frac{\text{ml}}{\text{min}}$. Better agreement is visible for the data that are corrected by subtraction of a reference scan without flow. Similar results were obtained for all axial slices. Considering only odd or only even echoes, the VFR is still a bit too low or too high. Best agreement is obtained for the combination (averaging) of odd and even echoes and correction with the no-flow measurement. However, these values are always between 10.1 and 10.2 $\frac{\text{ml}}{\text{min}}$, thus overestimating the expected VFR of $9.9 \pm 0.1 \frac{\text{ml}}{\text{min}}$ by 1 to 4 %. An analogue analysis was done for velocities v_1 (first eight echoes) and v_2 (last eight echoes) in x- and y-direction (figs. 28 to 30). A plot with the VFR for v_z calculated for each axial slice can be found in figs. 31 and 32. Also here the best agreement is obtained for the combination of odd and even echoes and correction with the no-flow measurement. Considering the whole 3D dataset, maximum velocities were found in the centre of the glass tube and had values of 23.5 $\frac{\text{mm}}{\text{s}}$ (x-/y-direction) and 17.3 $\frac{\text{mm}}{\text{s}}$ (z-direction). Since the cross-section is slightly flattened due to the manufacture process, it is not easy to predict the flow behaviour in x- and y-direction. However, for the straight tube with a round cross-section the velocity profile can be predicted for a laminar tube flow with $v_{\max} = 2 \cdot v_{\text{mean}}$. With the tube diameter and the VFR given in section 3.1, it was therefore calculated $v_{\max} = 16.8 \frac{\text{mm}}{\text{s}}$. The measured value for $v_{\max}$ was about 3 % higher due to superimposed noise. For laminar flow, the mean axial

Figure 21: Velocity maps (v_1^x) for axial slice 61. For the maps without flow, non-zero values are visible. For offset correction, flow and no-flow velocity maps were subtracted.
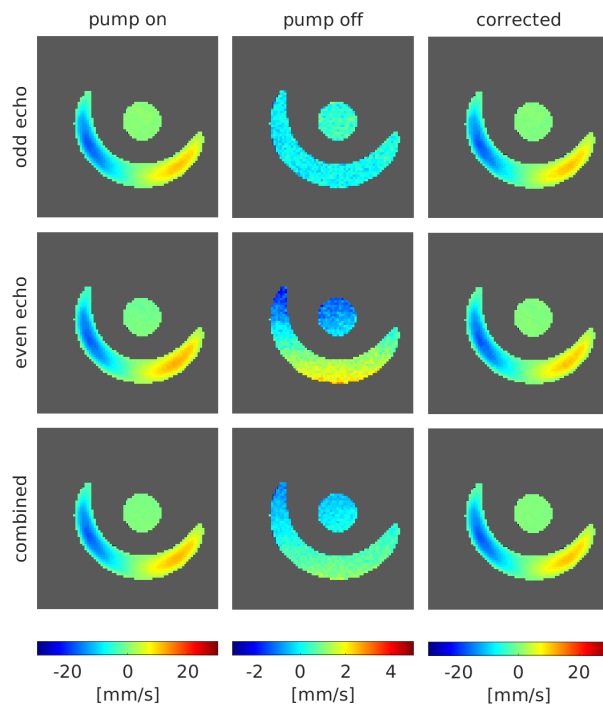
Figure 22: Velocity maps (v_2^x) for axial slice 61. For the maps without flow, non-zero values are visible. For offset correction, flow and no-flow velocity maps were subtracted.
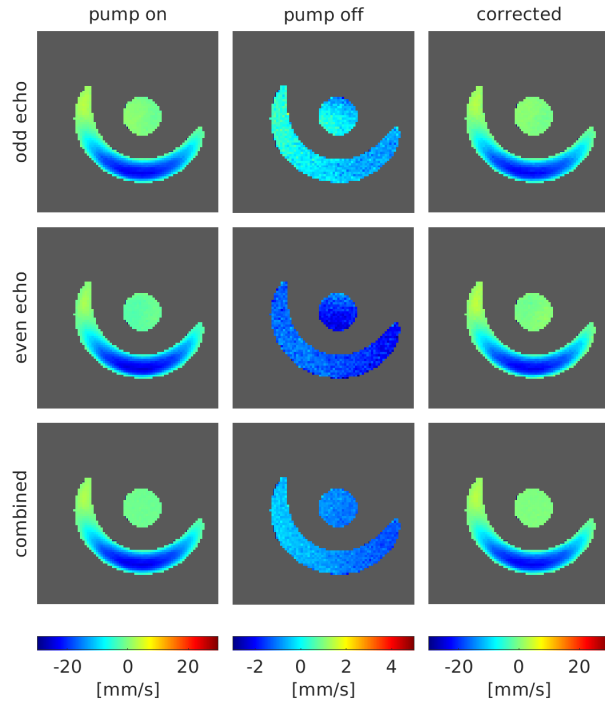
Figure 23: Velocity maps (v_1^y) for axial slice 61. For the maps without flow, non-zero values are visible. For offset correction, flow and no-flow velocity maps were subtracted.
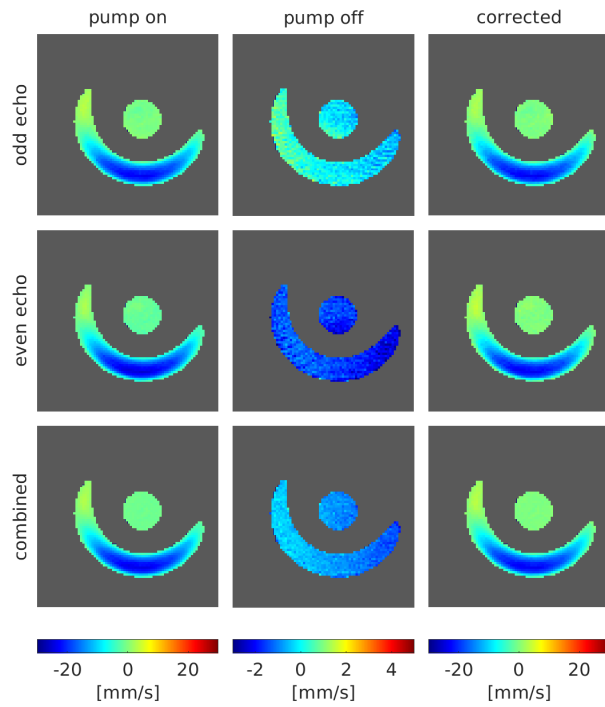
Figure 24: Velocity maps (v_2^y) for axial slice 61. For the maps without flow, non-zero values are visible. For offset correction, flow and no-flow velocity maps were subtracted.
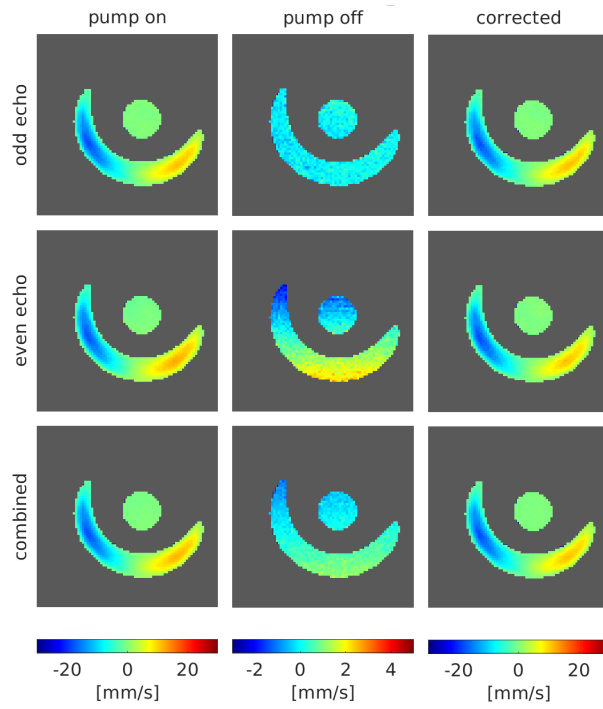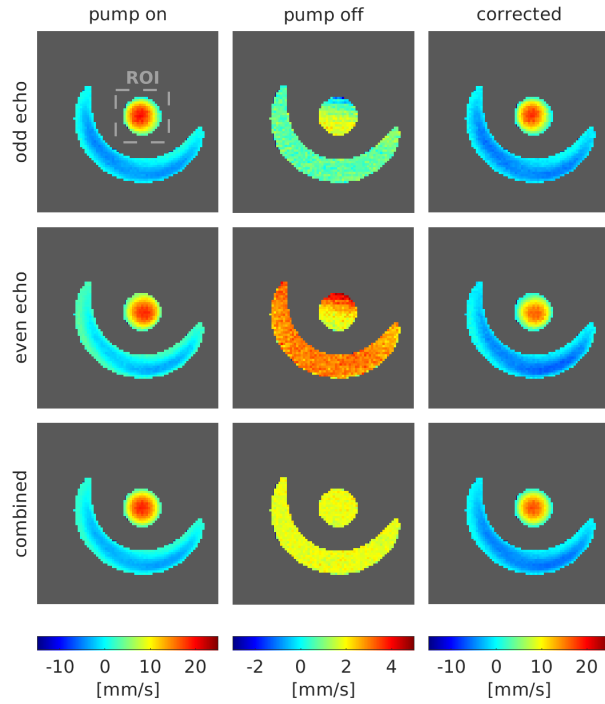
Figure 25: Velocity maps (v_1^z) for axial slice 61. For the maps without flow, non-zero values are visible. For offset correction, flow and no-flow velocity maps were subtracted.
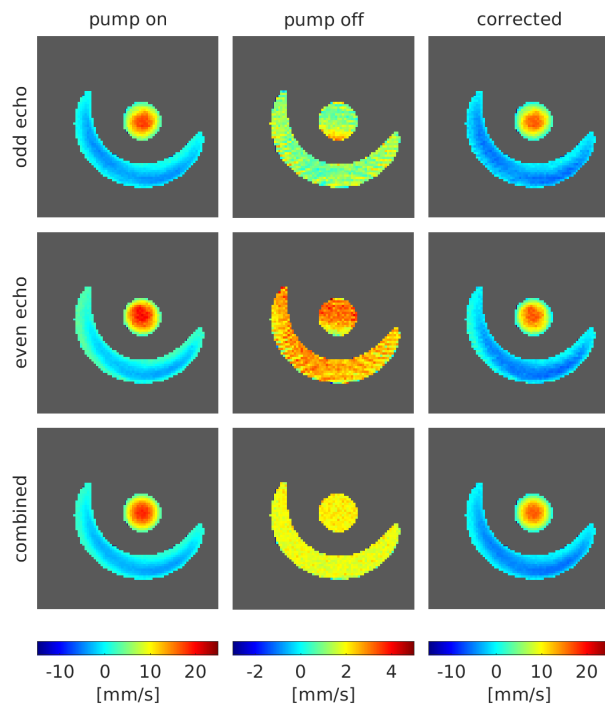
Figure 26: Velocity maps (v_2^z) for axial slice 61. For the maps without flow, non-zero values are visible. For offset correction, flow and no-flow velocity maps were subtracted.
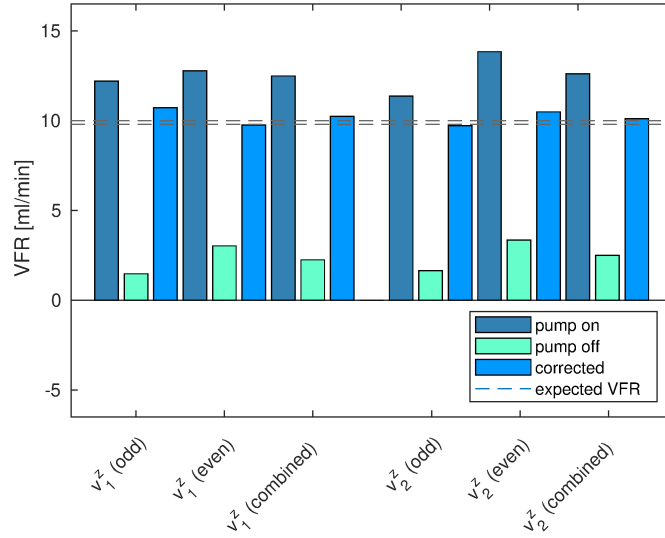
Figure 27: For every velocity map from fig. 25 and fig. 26 the VFR in the ROI was calculated and visualised as bar plot. The dotted lines indicate the expected VFR of $9.9 \pm 0.1 \frac{\mathrm{mm}}{\mathrm{s}}$.
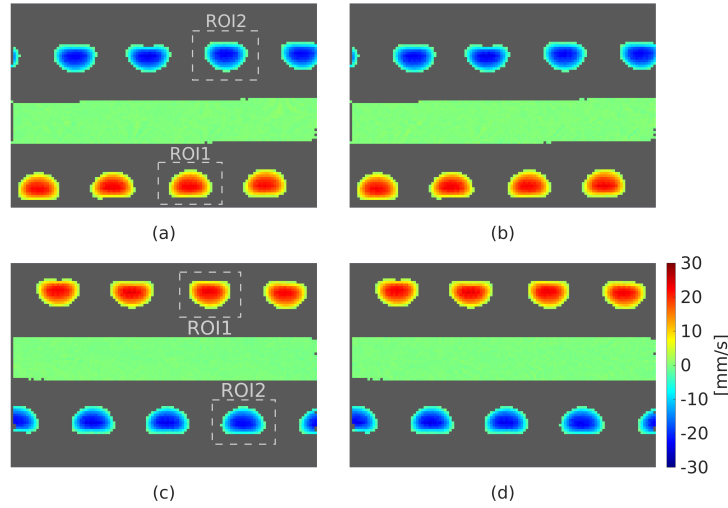
Figure 28: Velocity maps for combined odd and even echo and offset correction by no-flow measurement. Sagittal slice 37, velocity maps v_1^{x} (a) and v_2^{x} (b). Coronal slice 46, velocity maps v_1^{y} (c) and v_2^{y} (d).

velocity v_r at radius r can be calculated as a function of the maximum velocity v_{max} and the tube radius a:

$$v_r = v_{\mathrm{max}} \cdot \left(1 - \frac{r^2}{a^2}\right) \tag{57}$$

For one exemplary axial slice, the calculated axial velocity is compared with the measured one (fig. 33).

For each voxel, the signal intensity (magnitude value of the complex signal) was determined within the binary mask and averaged. The corresponding values acquired with flow are reduced by 2 % compared to those acquired without flow.
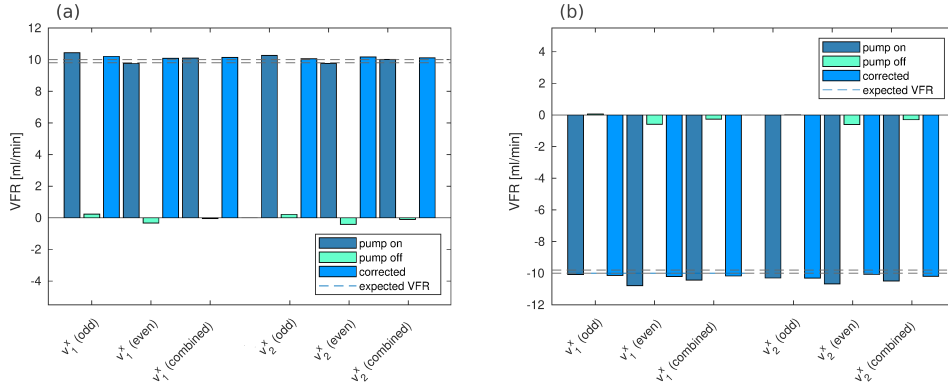
Figure 29: VFR analysis for ROI 1 (a) and ROI 2 (b) corresponding to fig. 28 (sagittal slice 37, velocity v_1^x and v_2^x).
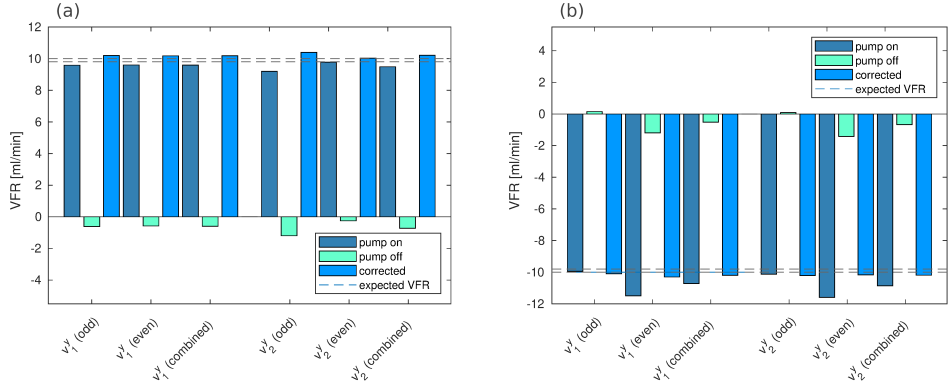
Figure 30: VFR analysis for ROI 1 (a) and ROI 2 (b) corresponding to fig. 28 (coronal slice 46, velocity v_1^y and v_2^y).

From the measured velocity components (v_x, v_y, v_z), the velocity magnitude was visualised in 3D by using the open-source software Paraview 5.10 (see fig. 34).

4.5.2 OCF

A dual-VENC measurement was performed for the OCF (for details see table 1). Complex valued images for each encoding step were combined (averaging odd and even echoes), before velocity values in x-, y- and z-direction were calculated. For the no-flow velocity map an offset up to 21.1% (v_1) and 12.9% (v_2) of the VENC depending on the spatial position was determined. For one axial slice, offsets are visualised in fig. 35. Offset correction was done by subtracting the flow from the no-flow velocity map. For an additional VNR improvement, unwrapped low-VENC and high-VENC maps were weigthed averaged based on the ratio $R = 2.25$. Axial slices of the corresponding velocity maps are shown in fig. 36.

The absolute values of the complex map were determined inside the binary mask and averaged. The values acquired with flow are decreased by 3% in comparison to those acquired without flow.
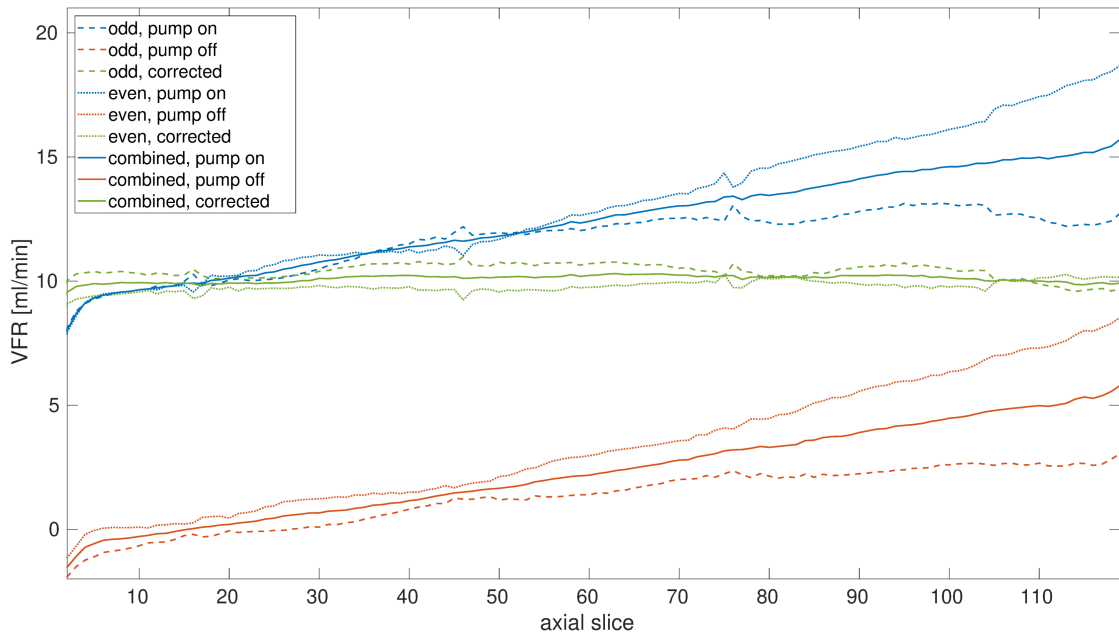
Figure 31: Plot of the VFR (v_1^z) along the z-direction of the flow phantom. The expected VFR is $9.9 \pm 0.1 \frac{\mathrm{ml}}{\mathrm{min}}$.
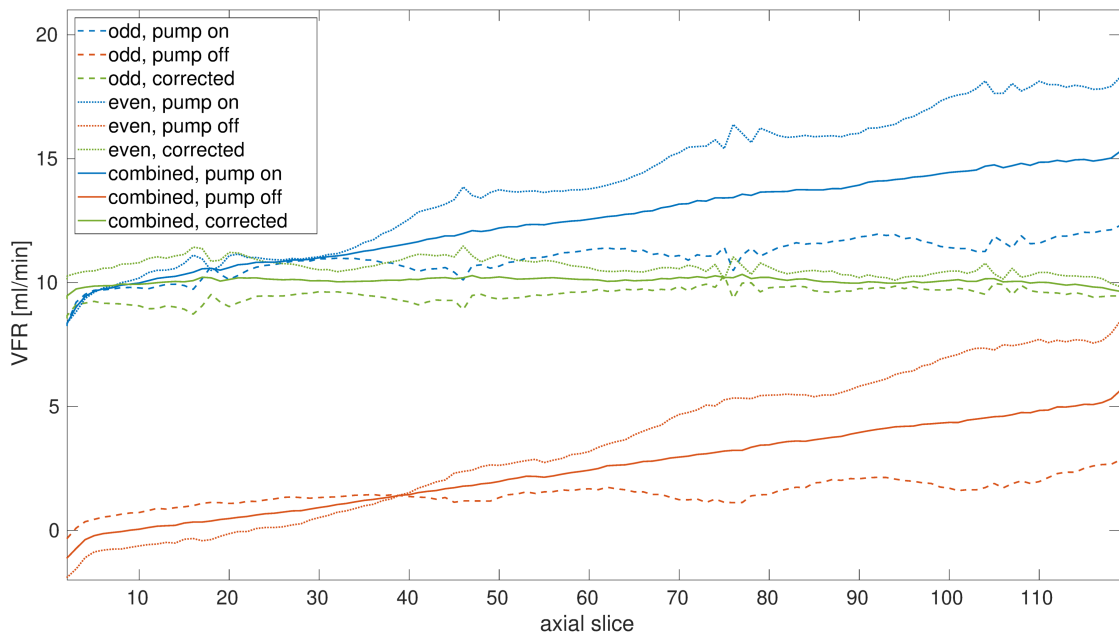
Figure 32: Plot of the VFR (v_2^z) along the z-direction of the flow phantom. The expected VFR is $9.9 \pm 0.1 \frac{\mathrm{ml}}{\mathrm{min}}$.
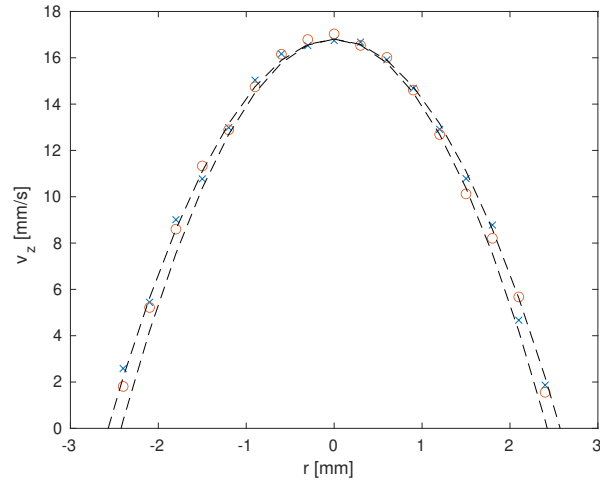
Figure 33: Velocity v_1^z ($\times$) and v_2^z ($\circ$) (datasets with $\mathrm{VENC}_1 = \mathrm{VENC}_2 = 40\,\frac{\mathrm{mm}}{\mathrm{s}}$) determined in a central axial slice after combining odd and even echoes and subtracting the no-flow data. In addition, the expected curve according to eq. (57) was calculated. In this calculation, the accuracy of the tube diameter ($5\pm0.15\,\mathrm{mm}$) was considered. The upper and lower limit of the expected curve are plotted with dashed lines.
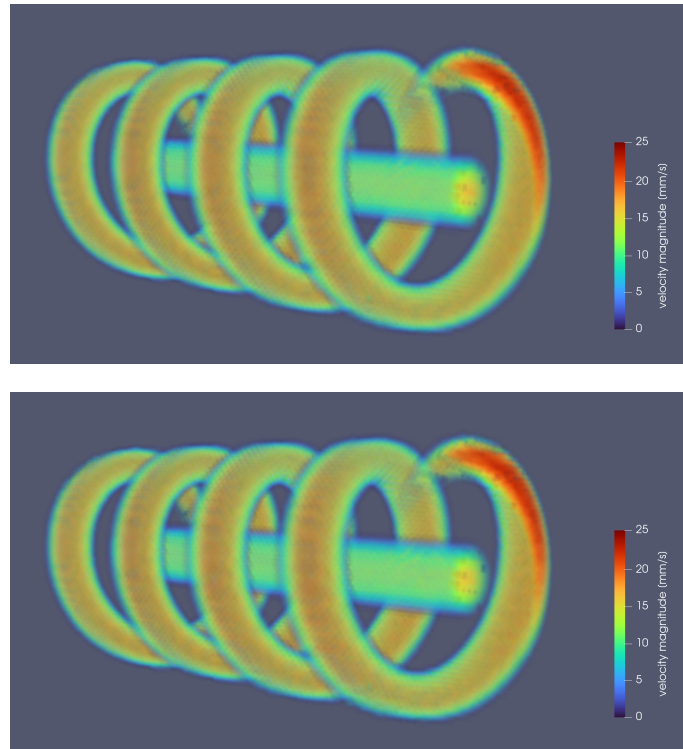
Figure 34: By using Paraview 5.10, the velocity magnitude was visualised in 3D. Similar shape can be observed for v_1 (top) and v_2 (bottom). These velocity maps were determined by offset correcting the velocity maps acquired with flow by subtracting the ones acquired without flow. Odd and even echo images were combined.
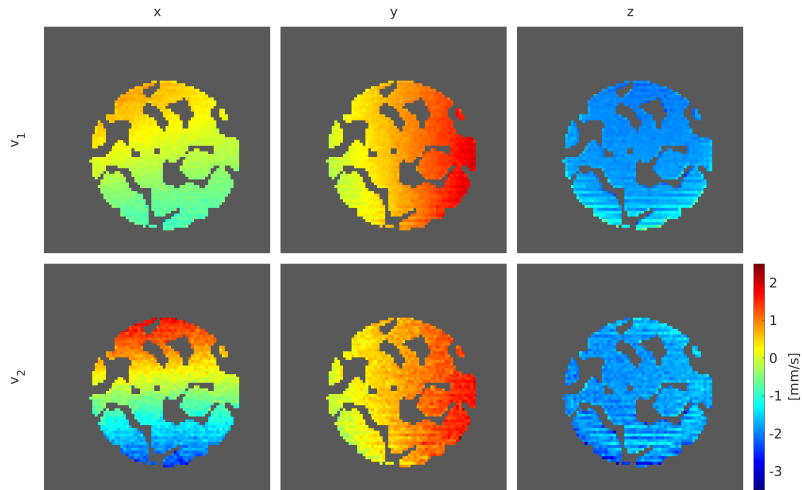
Figure 35: Exemplarily, no-flow velocity maps v_1 and v_2 (with $\text{VENC}_1 = 20 \frac{\text{mm}}{\text{s}}$ and $\text{VENC}_2 = 45 \frac{\text{mm}}{\text{s}}$) are shown for axial slice 41. Considering the whole 3D dataset, offsets up to 21.1% (v_1) and 12.9% (v_2) of the VENC depending on the spatial position were determined.
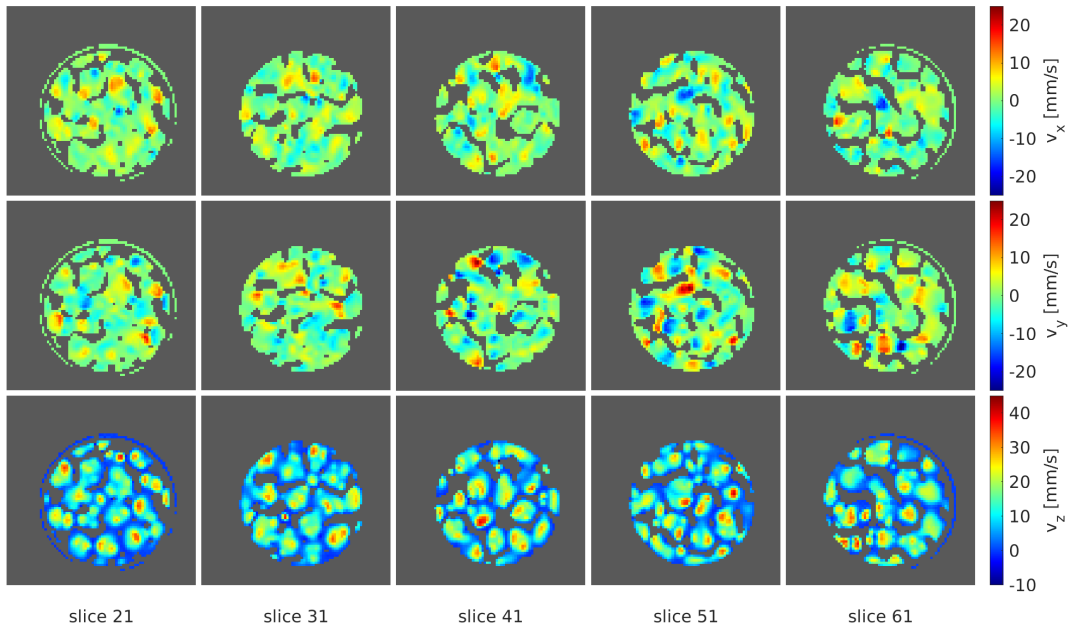
Figure 36: Velocity maps were offset corrected by subtracting the no-flow maps and unwrapped using the dual-VENC method. Additionally, unwrapped and high-VENC maps were weighted averaged. Exemplarily, several axial slices are shown for all velocity components (v_x, v_y, v_z). For fixation in the glass tube, seal tape was wrapped around the OCF. No tape was present at the beginning and end of the OCF. The water filled gaps between OCF and glass vessel result in the "rings" in slices 21 and 61. Velocity values inside these "rings" are about zero.

4.6 Discussion

High accuracy of MRV measurements on porous media is essential, especially if such measurements are used for validation of CFD-simulations. For improved VNR, a new multi-echo sequence with optimised repetition time T_R was proposed and a dual-VENC technique was used. Furthermore, systematic errors were analysed, which may occur in MRV measurements, in particular displacement errors and phase errors originating from eddy currents or different coherence pathways. Techniques were described to minimise or correct such errors.

4.6.1 Pulse Sequence

A flow phantom with predictable flow behaviour was measured to test the new multi-echo sequence. An offset was observed and the measured VFR overestimated the expected VFR if only odd or only even echoes are considered. This confirms that a combination (averaging) of odd and even echoes is necessary to correct for different coherence pathways. An offset was also observed if only the velocity maps with flow are considered. This confirms the assumption that the phase difference image (eqs. (31) to (33)) does not eliminate all phase errors. These findings are consistent with [87]. Eddy currents depend on the strength and direction of the applied magnetic gradients [31]. Thus, the eddy currents originating from the velocity encoding gradients behave additive in the phase difference image. The eddy currents could be reduced by setting smaller amplitude and longer duration for the velocity encoding and spatial encoding gradients. However, this would increase the echo time and as a consequence, the SNR would be decreased and the displacement error increased. In commercial systems, compensation for eddy currents is realised by using pre-emphasis systems that adjust gradient waveforms incorporating predictions of eddy current effects [31, 114, 115]. However, not all eddy current effects can be compensated for and there is currently no definitive solution to eliminate all background phase shifts caused by eddy currents. Therefore, residual phase shifts may occur, affecting the accuracy of the measurements. This is especially a problem when a very precise analysis is to be carried out, e.g. a comparison of MRV measurements with CFD simulations. Therefore, measurements with and without flow were subtracted from each other to ensure an accurate correction of remaining offsets. The corresponding VFR was slightly overestimated by 1 to 4 %. It can be assumed that the slow velocities, which are located at the surface of the flow phantom, were slightly overestimated due to partial volume effects. Details about such effects are described in [30, 31]. The measured axial velocity was compared with theoretically predicted values for laminar flow. A good agreement was visible for the flow profile. The maximum velocity determined from the measured axial velocity was slightly larger than the predicted value due to superimposed noise.

After one excitation pulse, several echoes were acquired. For the transverse relaxation time $T_2 = 0.41\,\mathrm{s}$ it was possible to measure 16 echoes with acceptable signal loss to achieve full dual-VENC encoding. Velocity maps v_1 and v_2 were reconstructed from the first and last eight echoes, respectively. By setting $\mathrm{VENC}_1 = \mathrm{VENC}_2$, reproducibility was evaluated, even though v_2 has lower SNR due to longer echo times. Velocity encoding and decoding gradients were applied before and after each echo.

Thus, the echo time was increased, respectively the SNR decreased. In [87], the interecho delay was shorter, because the velocity encoding gradients were applied before the echo train. However, this approach increases displacement errors. Thus, if the same echo time is assumed for both sequences, the displacement error for the last echo differs by a factor 50. Single-point imaging sequences, as proposed by [106], are able to reach a great reduction of displacement errors, but in comparison to the the sequence shown here the measurement time is strongly increased and not suitable for 3D imaging. For reduced measurement time, in [54] an echo-planar imaging sequence with velocity encoding was proposed. The reduction of displacement errors by updating the flow encoding for each echo was already proposed in [107] for the FLIESSEN sequence. Since this sequence aimed at short total measurement time, each echo of the long echo train was measured with different spatial phase encoding. In contrast, the sequence proposed in the present work uses all echoes for flow encoding. Therefore, the minimum total measurement time is longer than in FLIESSEN or other sequences that have a long echo train length with short T_{R}. However, for the sequence shown here a reduced spatial resolution in phase encoding directions is avoided as each image is measured at a fixed echo time.

The proposed approach assumes constant velocity and does not compensate for non-zero acceleration. To minimise the displacement errors, the time t_{displ} between velocity encoding and acquisition was kept as short as possible. Thus, also the influence of acceleration on the signal phase is limited. Most importantly, only two consecutive echoes (odd, even) are used for the calculation of the same image as different velocity encoding steps are performed along the echo train. Thus, summation of acceleration effects (by the consecutive echoes) would not lead to incorrect velocity encoding, but to reduced signal due to intra-voxel dephasing. However, a comparison of the data measured with and without flow yielded no notable differences in the signal intensity (magnitude value of the complex signal). The difference was 2 % for the flow phantom and 3 % for the OCF. Therefore, SNR losses due to velocity and acceleration effects, although being not suppressed, were negligible in the experiments. This was also proven by the fact that the measured VFR corresponds well with the expected values.

Flow through porous media, like the used OCF, usually has a large dynamic range. Therefore, the dual-VENC approach is of great use to prevent aliasing in fast flow regions but still realise a sufficient VNR in slow flow regions. For the chosen ratio between high- and low-VENC, the VNR was improved by $R = 2.25$ in comparison to a single-VENC measurement. Instead of doing a dual-VENC measurement, in the same time two accumulations of the high-VENC measurement could be done and averaged, which increases the VNR by $\sqrt{2}$. Therefore, the effective VNR improvement of the dual-VENC technique with $R = 2.25$ is $\frac{2.25}{\sqrt{2}} = 1.59$. An additional VNR improvement was achieved by averaging unwrapped and high-VENC data, as described by eq. (43). For $R = 2.25$ this is 9.4 %.

Each slice (and each velocity component) was visually inspected to determine if wrong unwrapping was present. Therefore, inside the pores it was searched for voxels, which show a large difference (about 2·VENC) in comparison to the surrounding ones. None of such voxels was found.

For the proposed sequence, a good compromise was found to achieve reduced dis-

placement errors, acceptable total measurement time and sufficient VNR.

4.6.2 Displacement Errors

For the flow phantom, maximum velocities of $23.5\,\frac{mm}{s}$ (x-/y-direction) and $17.3\,\frac{mm}{s}$ (z-direction) in the centre of the glass tube were determined. Higher velocities in x-/y-direction occurred due to the reduced cross-sectional area at the windings. Displacement errors are always a problem if the direction or magnitude of the velocity vectors change. This is generally the case for turbulent flow. Since for the measurement with the flow phantom the Reynolds number was $Re = 42$, laminar flow can be assumed. For the special case that only the straight tube of the flow phantom is considered (only axial velocity), in each axial slice a similar velocity should be present and therefore displacement errors would not have a negative effect on the velocity maps. However, large displacement errors would negatively influence the measured velocity fields in the windings of the flow phantom.

In these measurement a voxel size of $0.30\,mm$ was chosen. Considering the maximum velocity in x-/y-direction and the time between velocity encoding and readout, with eq. (52) a $displacement = 0.28$ voxels can be calculated, which corresponds to $0.08\,mm$. In [39], an overview of several current MRV studies is given and for the corresponding displacement errors values are specified between 0.9 and 14.8 voxels. In this context, the displacement errors shown in this work are relatively low. No matter how low the value is, displacement errors always occur, namely for spins located at the border of a voxel. However, it should be noted that the estimated displacement error occurs for the maximum velocity and therefore in most voxels the displacement error is much lower.

For the OCF, the maximum velocity was $44.7\,\frac{mm}{s}$ and the voxel size $0.45\,mm$. Therefore, displacement errors up to $displacement = 0.36$ voxels (corresponding to $0.16\,mm$) were present. This displacement error is small in comparison to the pore size of $5.8 \pm 1.9\,mm$. Additionally, the displacement error will be lower in most regions of the OCF as the displacement value of 0.36 voxels was calculated for the maximum velocity.

4.7 Conclusion

In this section, methods were described to achieve a good accuracy for MRV measurements and reduce systematic errors for slow flow of water through a 10 PPI OCF. A new multi-echo sequence with dedicated timings was proposed to achieve a compromise between VNR, total measurement time, spatial resolution and displacement errors. A dual-VENC encoding scheme was used and the repetition time was optimised for improving the VNR. Phase errors originating from different coherence pathways could be eliminated by averaging the datasets of odd and even echoes. Phase errors resulting from eddy currents could be eliminated by subtracting flow and no-flow velocity maps. An additional improvement of the VNR was achieved by using the dual-VENC technique and by weighted averaging of the unwrapped and high-VENC data.

For a reduction of the measurement time, MRV measurements could be combined with acceleration methods like compressed sensing [39] or parallel imaging [116].

In section 5, a further analysis of the velocity measurements is done. Also, other techniques are described for the correction of the phase offset. In section 6, the velocity maps measured with the presented MRV sequence are used for cross validation with CFD simulations.

5 Improvements

5.1 Introduction

In the previous section it was shown that for MRV measurements usually phase offsets, originating from eddy currents, occur. Correction of these offsets was done by doing a reference measurement without flow and subtracting the resulting phase map from the one acquired with flow. Doing so, the noise values are summed up and the accuracy is reduced by $\sqrt{2}$. To minimise this effect, the no-flow dataset can be fitted by a polynomial reducing the SNR loss [41, 117, 118]. However, it must be considered that for inaccurate fitting systematic errors may occur lowering the benefit of this technique. To my knowledge, this technique was not shown before for MRV measurements on porous media and also not for dual-VENC data.

For high accuracy of the acquired velocity maps, no changes should occur during the measurement time. However, different effects may prevent totally stable measurement conditions. For example, small temperature changes or changes in the electrical components may occur during the measurement operation [100, 101]. To minimise such effects, the measurement is started after the gradient amplifiers have warmed up for a few hours and the measurement is done in a closed air-conditioned room. If the flow is realised by a hydrostatically driven pump system, irregularities like pulsation effects can be neglected. However, the setup of such a hydrostatic pump as well as the setting of the desired flow rate is associated with a certain amount of effort. Other mechanical pump systems (for example peristaltic pumps, gear pumps, screw pumps, etc.) are often easier to handle and usually they enable higher flow rates. However, such pump systems are often sensitive to pulsation effects [119–122], especially peristaltic pumps. Pulsation effects are also a problem in medical application (e.g. blood flow). To reduce the influence of pulsation, in medical application triggering techniques are used to synchronise the repetition time T_{R} with the heart beat [33, 123].

Doing a reference measurement without flow, as described in the previous section, doubles the measurement time. If a study is conducted in which the flow fields of different samples are to be compared (as in [23, 124]), it would be advantageous if one no-flow measurement can be used as reference for a series of flow measurements in order to reduce the measurement time. Therefore, it shall be analysed to which extent such reference map is reproducible.

For medical application, it is not possible to repeat a measurement without flow as reference. For correction of phase errors, neighbouring stationary tissue may be used as reference [125, 126]. This technique also has the benefit that the measurement time is not increased. However, in [127] it was shown that this technique may worsen the accuracy. In this chapter the accuracy of this correction method shall be analysed quantitatively for porous media. This is of central interest to enable accurate cross-validation with CFD simulations.

Median-filtering is widely used in MRI to reduce the influence of noise [128–132]. To my knowledge, however, this has not yet been done for flow measured by MRV. Instead of doing polynomial fitting, also median-filtering may be done for the no-flow dataset before being subtracted from the dataset with flow. This should also reduce the SNR loss. It is to be clarified which method enables the best accuracy

of the resulting velocity maps.

5.2 Offset correction by polynomial fitting

If an offset correction is done by subtracting the no-flow velocity map voxel-wise, the VNR is lowered by $\sqrt{2}$. For reduced VNR loss, another correction method was used. Analogously to [41] a polynomial fit was applied to the no-flow dataset for reducing the effect of random noise. The following algorithm was used:

1. Otsu's thresholding algorithm [113] is applied to determine a threshold value based on the corresponding magnitude images. It is searched for the threshold value at which the intra-class variance of fore- and background is minimal. Based on the threshold value a binary mask BM_1 was calculated (see fig. 37(a)).

2. At the surface, partial volume effects are present, which can negatively influence the accuracy of the fit. To ignore such edge effects, another binary mask BM_2 was calculated. For each voxel in BM_1 it was checked if all 26 neighbouring voxels have the value 1. If yes, the considered voxel was set 1, if not it was set 0 (see fig. 37(b)).

3. Each no-flow velocity map was multiplied by the binary mask BM_2.

4. For each no-flow velocity map, polynomial fitting was done. The three-dimensional polynomial can be written as follows, where the order O is defined as the highest order of the polynomial's monomials (individual terms). The order of a term is the sum of the exponents of the variables that appear in it.

$$f(x,y,z) = \sum_{i,j,k=0}^{O} a_{i,j,k} \cdot x^i \cdot y^j \cdot z^k \qquad \text{for} \qquad i+j+k \leq O \qquad (58)$$

5. The polynomially fitted no-flow velocity map was subtracted from the corresponding map measured with flow.
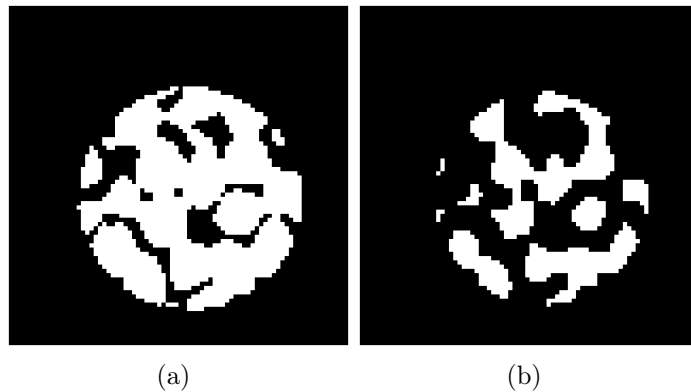

(a)   (b)

Figure 37: For the exemplary axial slice 41 the binary mask BM_1 (a) and the mask without edge voxels BM_2 (b) are shown.

5.3 Discontinuities in flow measurements

For perfectly reproducible measurements, the measured velocity maps of two accumulations only differ by their normally distributed noise values. Therefore, subtracting both maps would result in a standard deviation of noise increased by $\sqrt{2}$. In the following, the flow and no-flow MRV measurements done for the OCF structure (for details see section 4.4) are analysed in relation to their reproducibility. To exclude aliasing effects, only the velocity maps v_2 measured at the high-VENC are considered. Two accumulations were acquired and the corresponding velocity maps were subtracted from each other. This was done for the measurement with and without flow and all components (v_x, v_y, v_z). Results are exemplarily shown for one axial and one sagittal slice (figs. 38 and 39). For the measurements with flow larger values are visible. Also for the corresponding histograms a broadening can be observed (fig. 40). Corresponding standard deviation inside the OCF and tube
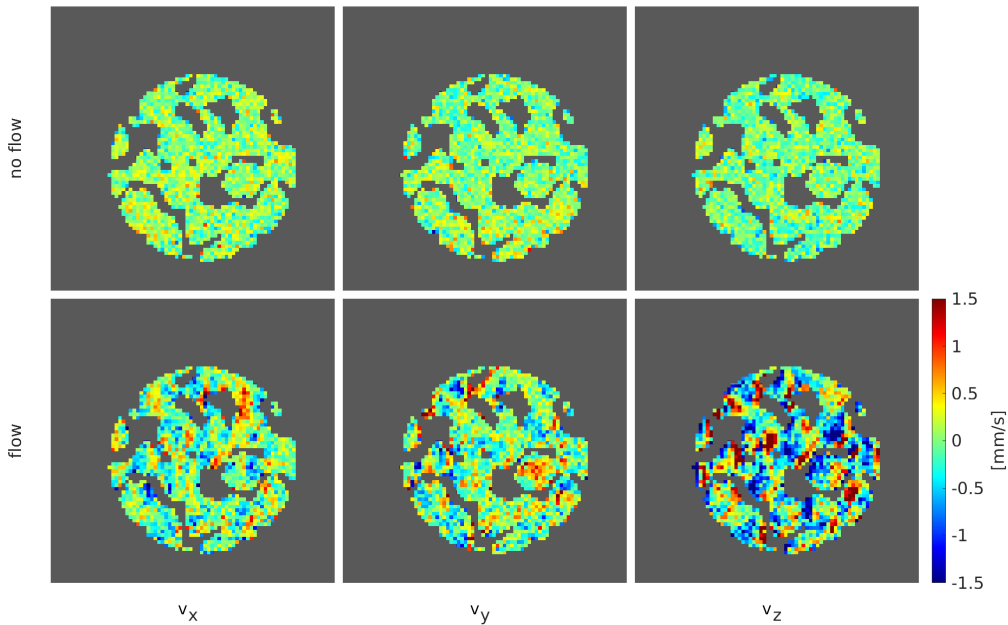
Figure 38: To evaluate the reproducibility, two accumulations were done for the measurements. Velocity maps from first and second accumulation were subtracted from each other. For the shown axial slice 41, larger variations are visible for the velocity values (v_2) with flow.

was determined (the noisy background was ignored by segmentation) and listed in table 4. Without flow, similar values are visible in x-, y- and z-direction, which are also roughly twice as high as the value $0.144\,\frac{mm}{s}$ calculated according to eq. (34). This corresponds the expectations because this $0.144\,\frac{mm}{s}$ was determined after averaging both accumulations (noise reduction by $\sqrt{2}$) and the values shown in table 4 were calculated by subtracting both accumulations (noise increased by $\sqrt{2}$). Values resulting from the velocity maps with flow are larger, between 2.2 and 3.7 fold increased.
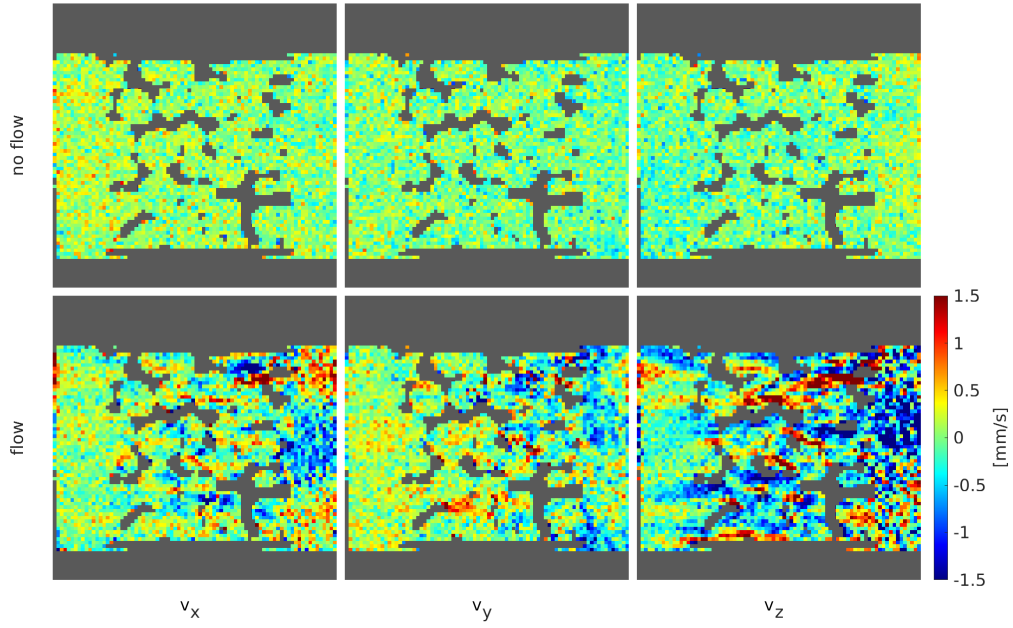
Figure 39: Velocity maps (v_2) from first and second accumulation were subtracted from each other. Analogously to fig. 38, for the shown sagittal slice 46 larger variations are visible for the velocity values with flow.
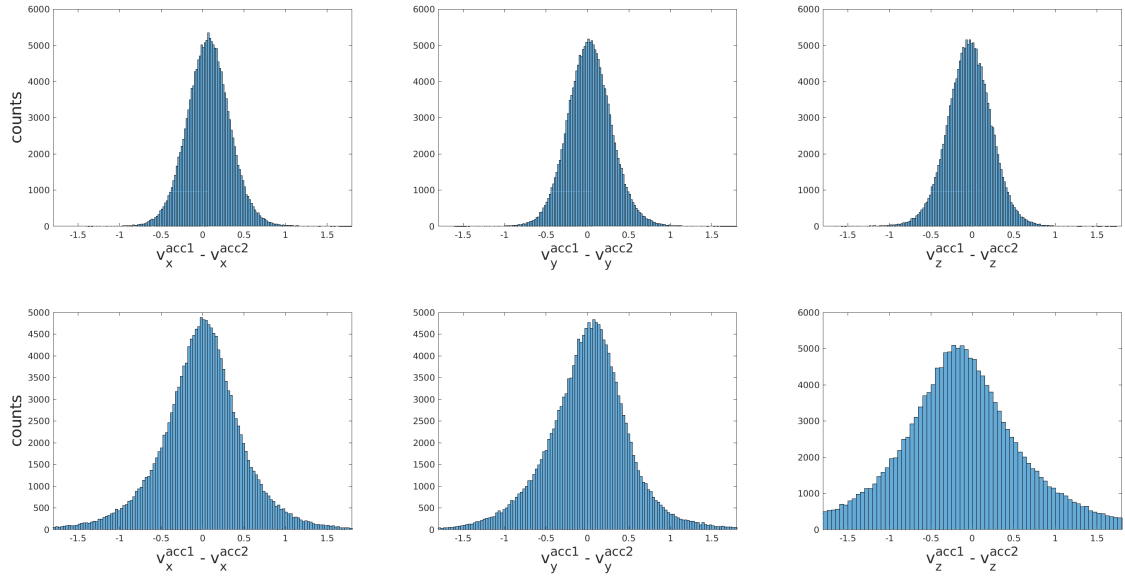
Figure 40: Velocity maps (v_2^{x}, v_2^{y}, v_2^{z}) from first and second accumulation were subtracted from each other. Histograms for the whole 3D difference maps were determined for the measurements done without (top row) and with flow (bottom row). For determining the histograms, only values inside the binary mask were considered (OCF and tube in the foreground, noisy background was ignored).

Discussion: When applying the dual-VENC technique, often a ratio R between two and three is chosen [47, 48, 133–135]. In the present study, an optimal R with negligible wrong unwrappings ($m = 5$, $P = 6 \cdot 10^{-7}$) was calculated and the optimal

Table 4: For each velocity map reconstructed from the high-VENC data (with and without flow) both accumulations were subtracted and the standard deviation was determined inside the OCF structure.

direction	σ_v (no-flow)[1]	σ_v (flow)[1]
x	0.263	0.607
y	0.269	0.601
z	0.268	0.974

[1] in $\frac{mm}{s}$

$R = 22$ could be chosen (eqs. (41) and (42), $N = 8$ due to subtraction of flow and no-flow velocity maps). For this calculation the mean SNR was assumed. However, voxels located at the edge areas are only partly filled with fluid and therefore have a lower SNR. For example, if a voxel is only filled to a quarter, the calculated optimal ratio would be $R = 5.4$. Due to large SSA, especially in porous media such edge voxels should be taken into account. Moreover, the calculation for such optimal R is only true for fully reproducible measurements. For a real measurement, changes may occur due to fluctuations of the fluid field or changes of the temperature or electrical components of the MRI system. Especially for 3D measurements, which usually run over longer time (the measurement for the OCF needed 20.6 h), such variations may be a significant factor. As shown in table 4, the standard deviation of the velocity maps with flow was up to 3.7 fold increased in comparison to the ones without flow. This indicates the presence of larger variations during the measurements with flow, which are presumably due to pulsation effect caused by the peristaltic pump used. Therefore, a rather low $R = 2.25$ was chosen.

A more systematic analysis of pulsation effects on MRV measurements should be done to achieve a better understanding and reduce flow induced phase fluctuations to such a level that similar σ_v values are obtained as in no-flow measurements. This should preferably be done by improving the pulsation dampening [136] or using a pulsation-free pump system. Alternatively, triggering techniques could be used that are widely applied in medical applications of MRV [33, 123]. Such measurements should be done for the same setup and VFR as described in section 4.4. The resulting standard deviation for the flow and no-flow velocity maps should be compared to evaluate the influence of pulsation. If lower pulsation effects are achieved, larger R values could be chosen to use the full potential of dual-VENC encoding.

It was assumed that screw pumps have a much lower pulsation in comparison to peristaltic pumps. Therefore, an analysis was done for the screw pump DM-JM Dosing Diamond series 012K2 (Nova Rotors, Sossano, Italy). Surprisingly, for the set VFR of $\sim 200\,\frac{ml}{min}$ the screw pump used did not guarantee a stable VFR during the measurement time. Over 2.5 h the VFR decreased continuously down to $\sim 90\,\%$ of the initially set VFR. Since it was also observed that the pump heated up considerably during operation, it can be assumed that this heating of the components was a contributory factor to the changed flow rate. Due to the instability of the VFR, no MRV measurements could be performed that were comparable to the ones done

with the peristaltic pump. Unfortunately, a further investigation or the purchase of another pump system is beyond the scope of this work.

However, it is proposed that a systematic study of different pump systems with corresponding MRV measurements will be carried out in the future to quantify the contribution of pulsation on velocity maps of porous media.

5.4 Global polynomial fitting

In section 4, velocity maps with and without flow were subtracted voxel-wise from each other to correct phase errors. In this section, global polynomial fitting is done for the no-flow map before subtracting. The velocity maps v_2 from section 4.4 are considered for each component (v_x, v_y, v_z). The no-flow velocity map (second accumulation) was polynomially fitted according to the algorithm presented in section 5.2. The principle of fitting is visualised for two central slices in the OCF structure by the example of a first order polynomial (see fig. 41).
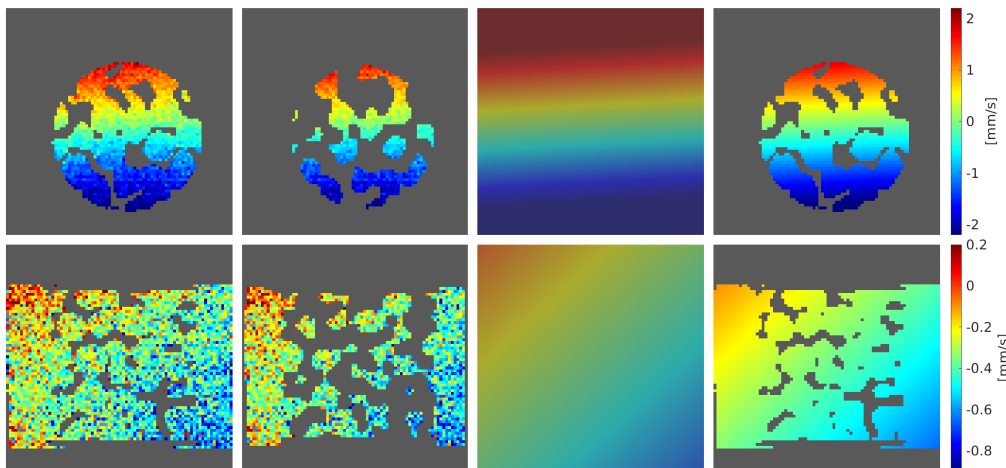
Figure 41: Top row: Axial slice 41. Bottom row: Sagittal slice 46. For the no-flow velocity map v_2^x ($VENC_2 = 45 \frac{mm}{s}$) spatially dependent offsets are visible (first column). For ignoring edge voxels, the algorithm from section 5.2 is used and the binary mask BM_2 is applied (second column). Values in this mask are exemplarily fitted by a first order polynomial. Higher order polynomial fits will be discussed in the course of this section. For the resulting map (third column) the mask BM_1 is applied (fourth column).

No-flow velocity map (first accumulation) and polynomially fitted map (second accumulation) were subtracted from each other. The resulting difference map is referred to as D_O where $O = [1, 6] \in \mathbb{Z}$ stands for the fit order of the polynomial fit. Exemplarily, one axial and one sagittal slice of D_1, D_2 and D_3 are shown in figs. 42 and 43.

Using the first order fit (D_1), areas with similar non-zero values can be observed locally. These areas are the most concise for the velocity in z-direction. For higher fit order these areas are not completely eliminated but smaller and values are more randomly distributed around zero. The standard deviation of the whole 3D velocity map within the OCF structure was determined and the corresponding values, as well as the Root-Mean-Square Error (RMSE) of the fits, are plotted in fig. 44.

Figure 42: No-flow velocity map (v_2) was corrected by subtracting the polynomially fitted map of different orders. Axial slice 41 is shown for v_x, v_y and v_z. For comparison, the voxel-wise subtracted maps are shown in fig. 38.
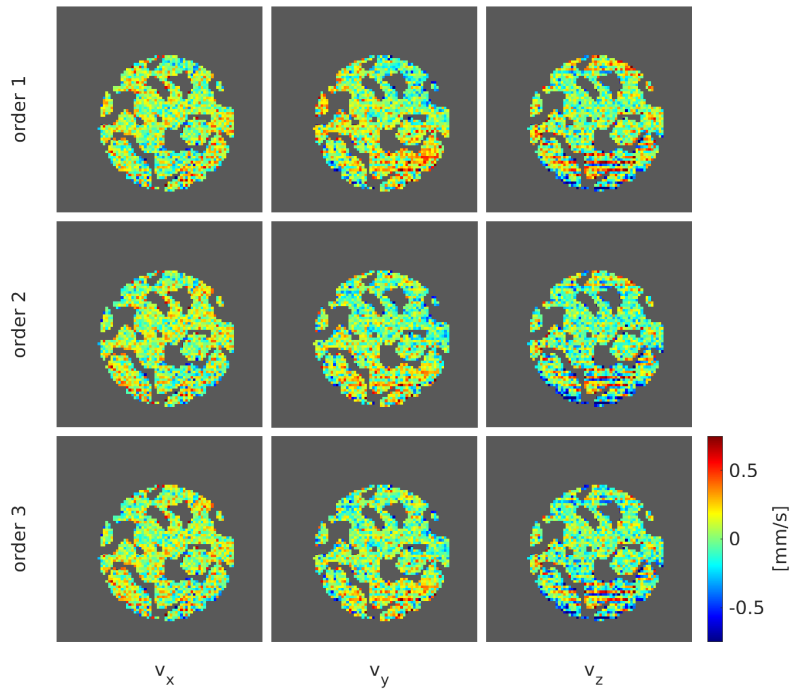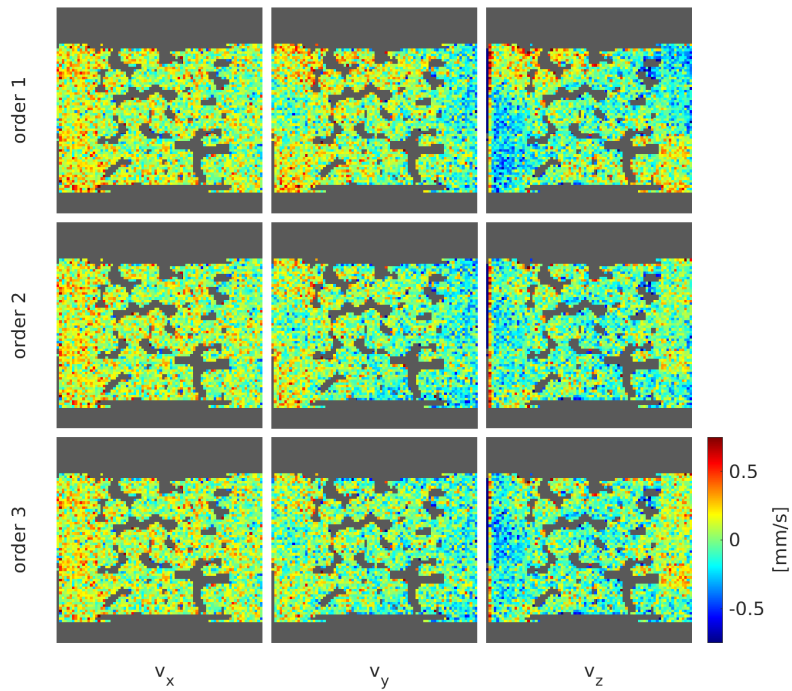

Figure 43: No-flow velocity map (v_2) was corrected by subtracting the polynomially fitted map of different orders. Sagittal slice 46 is shown for v_x, v_y and v_z. For comparison, the voxel-wise subtracted maps are shown in fig. 39.

Maximum values are visible for the first order fits. Independent of the fit order, the
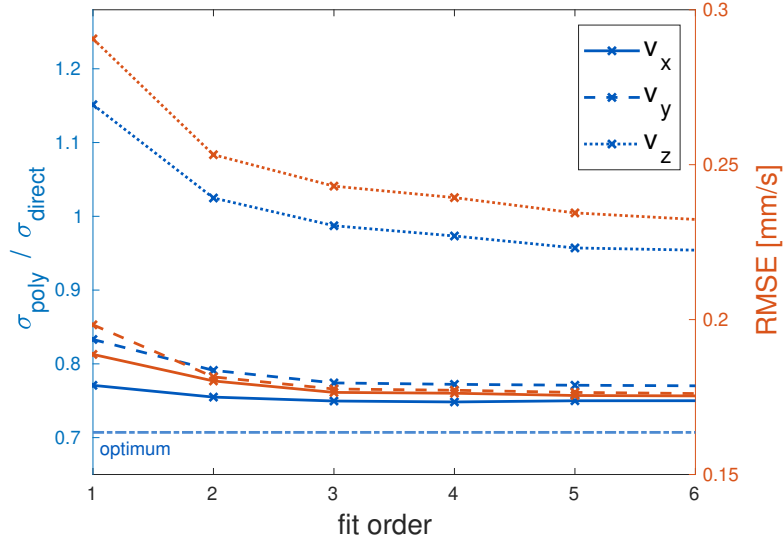

Figure 44: The no-flow velocity maps (v_2, second accumulation) were fitted by polynomials of different orders. The accuracy of the fits was determined by the RMSE. Here, the whole 3D map inside the OCF was considered. No-flow velocity maps (first accumulation) and fitted maps were subtracted from each other. The standard deviation was determined and normalised to the corresponding values from table 4. The optimum of $\sqrt{2}/2$ would result for a perfect fit.

standard deviation for the x- and y-component is lower than for directly subtracting two accumulations. For the different fit orders the values are in the range of 0.75 to 0.77 (x-component) and 0.77 to 0.83 (y-component). Also for the z-component a steady decrease can be observed for both, the RMSE and the standard deviation. However, only for third to sixth fit order the standard deviation is below 1 (0.98 to 0.95).

Phase cycling: Crusher and spoiler gradients in the sequence were used to suppress artefacts (for details about these gradients, see section 1.5.3). It is tested, if a further suppression can be achieved by using phase cycling for the excitation RF-pulse. The measurements for the OCF structure described in section 4.4 were repeated with same parameters, but phase cycling was done for the excitation RF-pulses. With a value of $212 \pm 2 \frac{\text{ml}}{\text{min}}$, the VFR was slightly larger (for the measurement without phase cycling, it was $206 \pm 2 \frac{\text{ml}}{\text{min}}$). One measurement consisted of two accumulations done with the phase of the excitation RF-pulses shifted by 180° and both accumulations were averaged. The receiver phase was also adapted so that the signals add up and do not cancel each other. Analogously to the previous analysis done in this section, two similar measurements were done (each with two averaged accumulations). The resulting velocity maps of the second measurement were polynomially fitted and subtracted from the velocity maps acquired for the first measurement. The resulting RMSE of each fit and the standard deviation of each fitted map was determined and is plotted against the corresponding order (see fig. 45). With increasing fit order, a
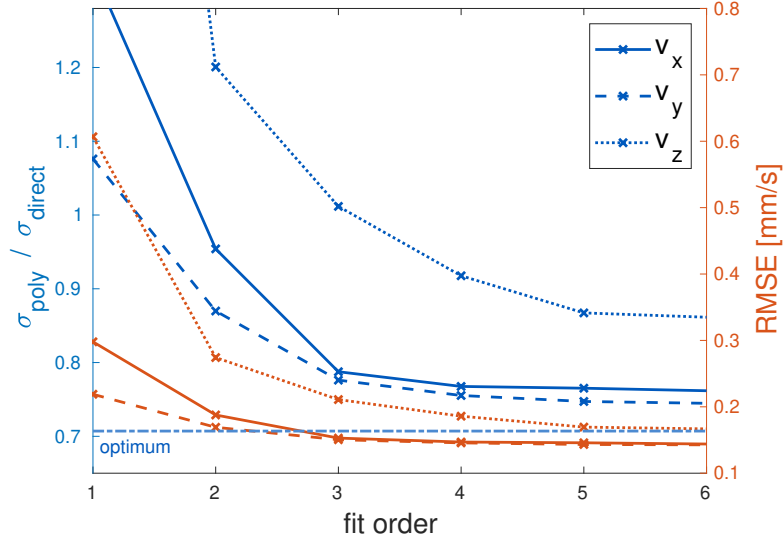
Figure 45: Phase cycling was done with the phase of the excitation RF-pulses shifted by 180°. Two similar measurements were done. The no-flow velocity maps (v_2, second measurement) were fitted by polynomials of different orders. The whole 3D map inside the OCF was considered and the accuracy of the fits was determined by the RMSE. No-flow velocity maps (first measurement) and fitted maps were subtracted from each other. The standard deviation was determined and normalised to the corresponding values if voxel-wise subtraction was done. The optimum of $\sqrt{2}/2$ would result for a perfect fit.

steady decrease can be observed for both, the standard deviation and the RMSE. This is the case for all components (v_x, v_y, v_z). For sixth fit order, the minimum standard deviations 0.76 (v_x), 0.74 (v_y) and 0.86 (v_z) are present.

Discussion: For the correction of phase errors in the velocity map, it is common to do a reference measurement without flow and subtract the resulting velocity map from the one acquired with flow voxel-wise. However, since the noise errors sum up, this increases the standard deviation by $\sqrt{2}$. In this section, the no-flow velocity map was polynomially fitted before being subtracted from the map acquired with flow. For a perfect fit, this would cause a reduction of the standard deviation by $\sqrt{2}/2 \approx 0.71$ in comparison to voxel-wise subtraction.

In this section, the fitting process was demonstrated for all three components of the aliasing-free maps v_2. Additionally, no-flow velocity maps were corrected by the fitted maps and the standard deviation was determined as another measure for the accuracy of the fits. RMSE and standard deviation were determined for different fitting orders. To analyse the influence of artefacts, measurements were done with and without phase cycling for the excitation RF-pulse.

In most cases, values of RMSE and standard deviation decrease with increasing fit order and thus, lowest values are present for the highest (sixth) order. For v_x and v_y without phase-cycling, no significant changes are present for third or higher fit order. Due to the fact that in no case a significantly increased standard deviation

was observed for higher fit order, it can be assumed that no overfitting was present. However, if fitting is done with even higher order, it shall be considered that overfitting may worsen the accuracy.

For the v_x- and v_y-maps, most artefacts could be suppressed by using crusher and spoiler gradients. If measurements are done with or without phase cycling for the excitation RF-pulse, no significant difference is present for the standard deviation of the corrected velocity map (table 5). However, a larger difference can be observed for v_z. One could assume that the reason for this difference are artefacts caused by remaining transverse magnetisation at the end of the sequence. However, dephasing of remaining transverse magnetisation at the end of the sequence was achieved by applying spoiler gradients. Furthermore, the long repetition time T_R compared to T_2 should have caused an almost complete dephasing of the spins before the next excitation pulse was applied. It can therefore be assumed that the artefacts resulted from the fact that the amplitude of the crusher gradients was not sufficient. Additional coherence pathways due to non-ideal refocusing pulses were therefore not completely suppressed. Obviously, the remaining artefacts are better suppressed if phase cycling is done additionally. The phase offset can be fitted more accurately, which results in a decreased RMSE and standard deviation. For the fit of sixth order, the standard deviation has a value of 0.86 instead of 0.95.

Table 5: The no-flow velocity maps (v_2, second accumulation) were fitted by polynomials of different orders. No-flow velocity maps (v_2, first accumulation) and fitted maps were subtracted from each other. The standard deviation was determined and normalised to the corresponding values if voxel-wise subtraction was done. The minimum values (in most cases, these are present for the highest fit order) are listed for the measurement without (1) and with (2) phase cycling for the RF-pulse.

	$\sigma(v_x)$	$\sigma_v(v_y)$	$\sigma_v(v_z)$
(1)	0.75	0.77	0.95
(2)	0.76	0.74	0.86

In this section, using a phase cycle doubled the measurement duration (but also improved the SNR by $\sqrt{2}$ due to averaging). For a shorter measurement duration, instead of phase cycling, crusher gradients with larger amplitude can be used to suppress the effects of the unwanted coherence pathways. It should be noted, however, that in this case stronger unwanted eddy currents occur, as these scale with the strength of the applied crusher gradients. Alternatively, for a better crusher effect, the duration of the crusher gradients can be increased. This, however, worsens the timing of the sequence, as longer echo times result.

5.5 Median filtering

In the previous sections, no-flow velocity maps were polynomially fitted before being used for offset correction. It is to be analysed whether median filtering can be done

alternatively. In median filtering, the values of the voxels in a defined neighbourhood of a voxel are collected, sorted by size and ranked. The middle value is selected from this sorted list and replaces the value of the current voxel. The filter size should be chosen in such a way that the local change of the phase offset in the considered neighbourhood is small in comparison to the noise values. Doing so, the standard deviation of the corrected velocity map is decreased due to denoising. For larger filter sizes, the image information is distorted.

For better understanding, this effect is visualised for the example of a 1D plot (fig. 46). However, in the following median filtering was done for the 3D velocity maps and consequently, 3D (cubic) neighbourhoods were considered to be filtered.
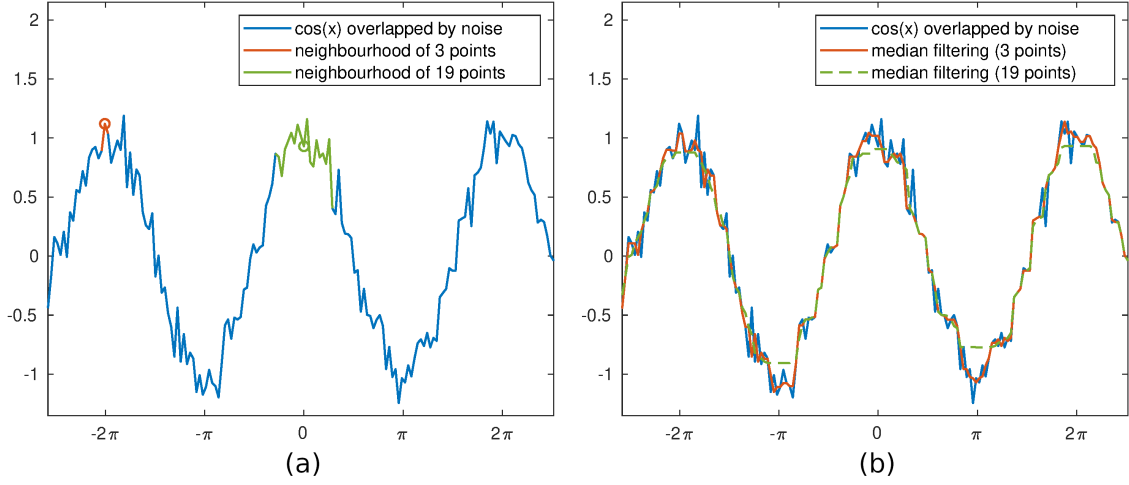

Figure 46: The principle of median filtering is visualised by the example of a plot of the function $f(x) = \cos(x)$, which is overlapped by normally distributed noise (blue). In (a), one exemplary data point in a neighbourhood of 3 data points is marked (orange, first maximum). When median filtering is done, the respective neighbourhood of each data point along the plot is considered and the median value is determined in each case. The value of each data point is replaced by the respective median value. Since the local change of the function in a neighbourhood of 3 data points is small in comparison to the noise values, denoising is achieved (b, orange curve). However, for a too large neighbourhood deformation of the filtered function results. This is visualised for a 19 data points large neighbourhood. For the filtered plot in (b, green curve), deformation results in such a way that the extrema are flattened.

All components (v_{x}, v_{y}, v_{z}) of the velocity map v_2 acquired with phase cycling (measurements from section 5.4) are considered. For the non-masked velocity maps, median filtering was done with different filter sizes (between $3{\times}3{\times}3$ and $15{\times}15{\times}15$). Filtered velocity maps are exemplarily shown in figs. 47 and 48. Measurement 1 and median filtered maps (measurement 2) were subtracted from each other. For each filter size, the standard deviation of the whole 3D velocity map within the OCF structure was determined and normalised to the corresponding no-flow values from table 4. Values are plotted in fig. 49. For the x-, y- and z-component, the minimum standard deviation is at filter size $5 \times 5 \times 5$ (see table 6).
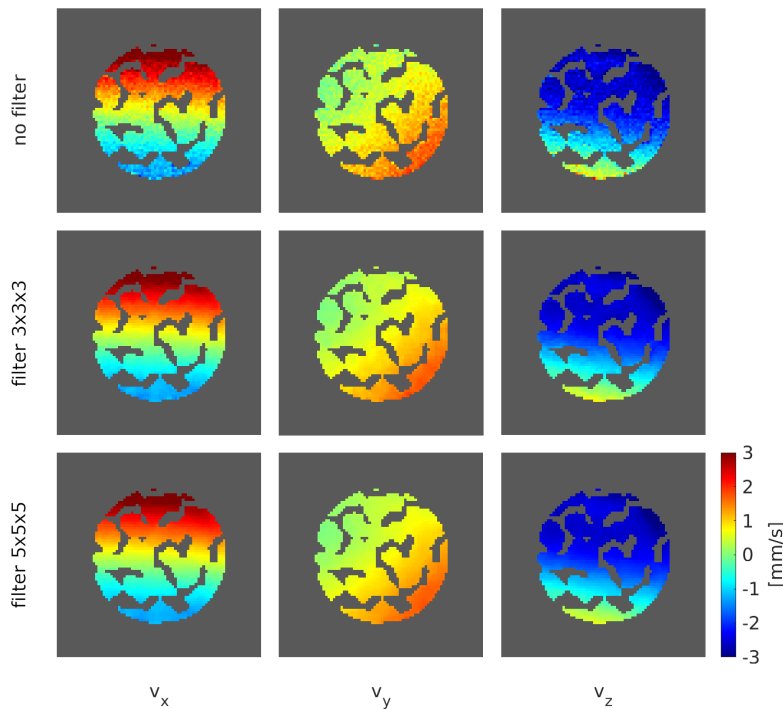
Figure 47: The no-flow velocity maps (v_2, $\mathrm{VENC}_2 = 45\,\frac{\mathrm{mm}}{\mathrm{s}}$, second measurement) were median filtered with different filter sizes. Corresponding maps are shown for axial slice 41. As reference, maps without filtering are shown.

Discussion: As an alternative to polynomial fitting, median filtering was used for correction of the phase offset. For all velocity components, an optimum was found for a filter size of $5 \times 5 \times 5$ voxels. Denoising due to median filtering decreases the standard deviation of the velocity map. For larger filter sizes, the standard deviation increases since the image information is distorted.

There is no significant difference in the standard deviation if the correction was done by polynomial fitting (sixth order) or by median filtering (filter size $5 \times 5 \times 5$) (see table 6). Therefore, median filtering is a suitable alternative to the more commonly used polynomial fitting [31, 41, 117, 118, 137, 138]. Different from polynomial fitting, median filtering does not involve the risk of overfitting. However, if the filter size is chosen too large, the accuracy is reduced. It is therefore advisable to check different filter sizes for a system to guarantee the best accuracy. It shall be noticed that phase offsets caused by eddy currents depend on the strength and direction of the applied gradients. Thus, the phase offset is different when parameters, e.g., the VENC-value or the chosen FOV are changed. Since the local change of the phase offset in the considered neighbourhood need to be small in comparison to the noise values, also the SNR plays an important role for the optimum filter size. Therefore, such an analysis of the optimum filter size should be done individually for each measurement.

56
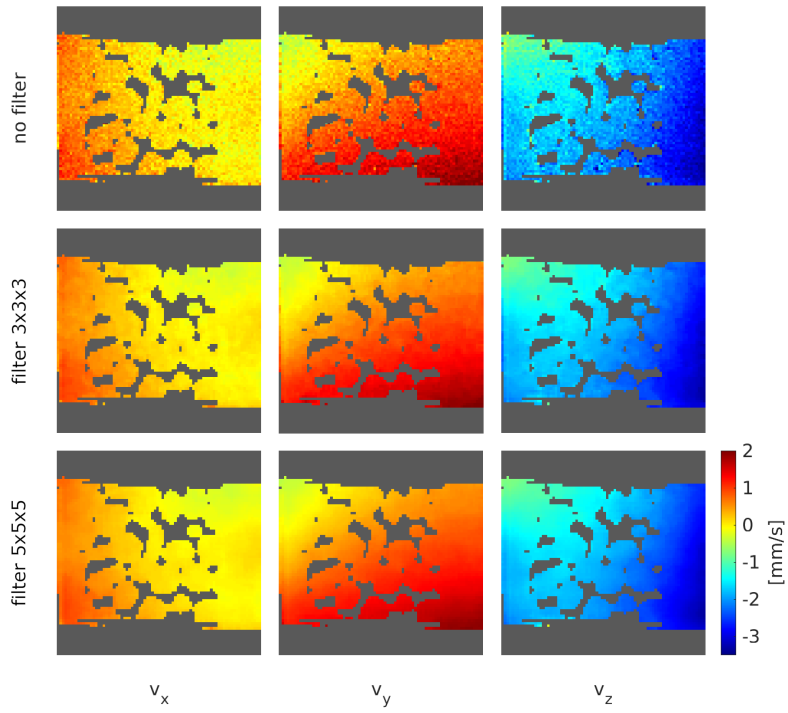
Figure 48: The no-flow velocity maps (v_2, $\text{VENC}_2 = 45\,\frac{\text{mm}}{\text{s}}$, second measurement) were median filtered with different filter sizes. Corresponding maps are shown for sagittal slice 46.
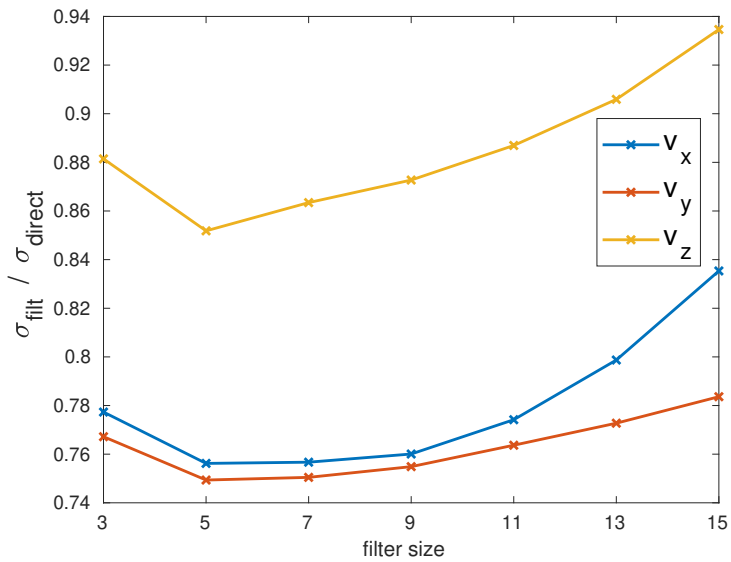
Figure 49: The no-flow velocity maps (v_2, first measurement) were offset corrected by median filtering velocity maps (second measurement) with different filter sizes. Measurement 1 and filtered maps were subtracted from each other. The standard deviation was determined for the whole 3D dataset and normalised to the corresponding values from table 4.

57

Table 6: The no-flow velocity maps with phase cycling for the excitation RF-pulse (v_2, second measurement) were fitted by polynomials of different orders. No-flow velocity maps (v_2, first measurement) and fitted maps were subtracted from each other. The standard deviation was determined and normalised to the corresponding values if voxel-wise subtraction was done. The minimum values (in most cases, these are present for the highest fit order) were determined (1). Alternatively, the offset correction was achieved by median filtering the second measurement (2). The minimum normalised standard deviation σ_v for the offset corrected map is present if median-filtering was done with a $5 \times 5 \times 5$ filter size.

	$\sigma(v_\mathrm{x})$	$\sigma(v_\mathrm{y})$	$\sigma(v_\mathrm{z})$
(1)	0.76	0.74	0.86
(2)	0.76	0.75	0.85

5.6 Reproducibility

It would be advantageous if the same no-flow reference could be used to correct the phase errors for different measurements. This would decrease the total measurement time. Therefore, in this section it is analysed to what extent the phase offset is reproducible.

Measurement parameters: A dedicated measurement was done for the OCF without flow of tap water. VENC-values were chosen analogously to section 4.4. For reduced measurement time, the matrix size was decreased and the shorter repetition time $T_\mathrm{R} = 1.2\,\mathrm{s}$ was chosen. Remaining parameters are listed in table 7. Noise

Table 7: Parameters for the measurements of the OCF without flow. For improved image quality measurements were averaged n-times.

Matrix size	FOV [mm^3]	Voxel size [mm]	VENC$_1$ $\left[\frac{\mathrm{mm}}{\mathrm{s}}\right]$	VENC$_2$ $\left[\frac{\mathrm{mm}}{\mathrm{s}}\right]$	n_avg	Meas. time [h]
$60 \times 60 \times 60$	$30 \times 30 \times 30$	0.5	20	45	2	2.4

parameters were determined for the low-VENC data (first eight echoes). For each pair of consecutive odd and even echo the magnitude images were combined (averaging) and the respective SNR was calculated according to eq. (35). The mean value was SNR = 142.3, which was used to calculate $\sigma_v = 0.202\,\frac{\mathrm{mm}}{\mathrm{s}}$ (eq. (34), number of encoding steps $N = 4$).

Shifting of the sample: After doing one measurement for the OCF as described above, the sample was shifted in axial direction so that only the glass tube was located in the FOV. The measurement was repeated with the same parameters. Resulting velocity maps v_1^z are shown in fig. 50. A spatially dependent phase offset is visible for both velocity maps. For subtraction of both velocity maps (OCF and glass
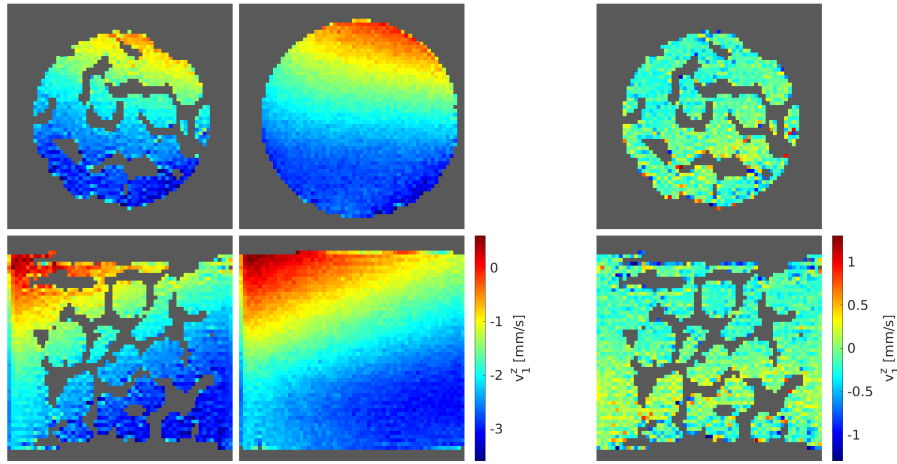
Figure 50: Velocity maps v_1^z are shown for axial slice 30 (top row) and coronal slice 31 (bottom row). Measurements were done for the OCF (left column) and repeated with same parameters after shifting the sample in axial direction such that only the glass tube was located in the FOV (centre column). Both velocity maps were subtracted from each other (right column).

tube) from each other, areas with similar non-zero values can be observed locally. Considering only the voxels inside the binary mask (ignoring the noisy background),
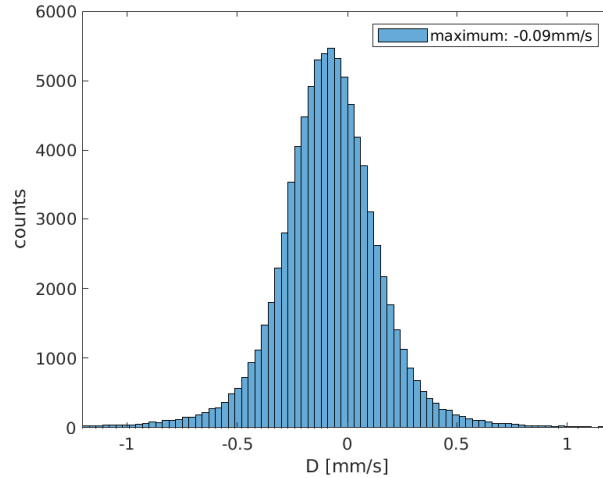
Figure 51: Histogram of the difference map D calculated by subtracting the velocity maps v_1^z with OCF and the glass tube located in the FOV from each other as shown in fig. 50.

the histogram was calculated for the difference map (fig. 51). The values are not distributed around zero, but have a maximum at $-0.09\,\frac{mm}{s}$. The standard deviation $0.453\,\frac{mm}{s}$ was determined, which is much larger if the phase offset of both velocity maps were perfectly reproducible. With regard to the σ_v calculated in section 5.6 this would be $\sqrt{2} \cdot 0.202\,\frac{mm}{s} = 0.286\,\frac{mm}{s}$.

Each map (OCF and glass tube) was fitted by a polynomial of sixth order. The resulting fitted maps were subtracted from each other and the mask for the OCF

Figure 52: For both velocity maps v_1^z (OCF and glass tube in the FOV) a polynomial fit of sixth order was done individually. Fitted maps were subtracted from each other. Exemplary, the corresponding axial slice 30 and coronal slice 31 of the difference map are shown.

was applied (fig. 52). For the difference map a spatially dependent offset is clearly visible. The values lie between $-0.394\,\frac{mm}{s}$ and $0.334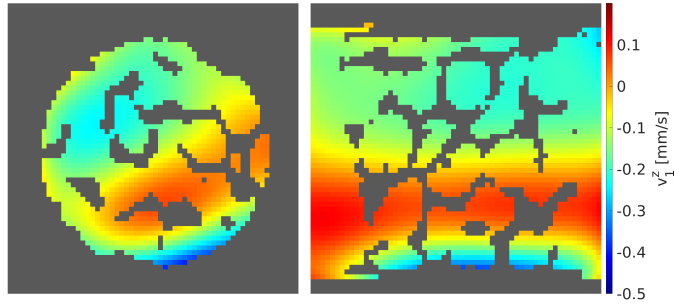\,\frac{mm}{s}$, which are larger than the standard deviation $\sigma_v = 0.202\,\frac{mm}{s}$ calculated in section 5.6.

Restarting of the gradient amplifiers: Without changing the position of the sample (glass tube in the FOV), settings of the shim coils were reset and the gradient amplifiers were turned off. After approximately 15 min the amplifiers were turned on again and the standard adjustments were done (setting shim coils, resonance frequency, pulse gain and reference gain). The measurement was repeated with the same parameters as before. Both velocity maps (v_1^z) were subtracted from each
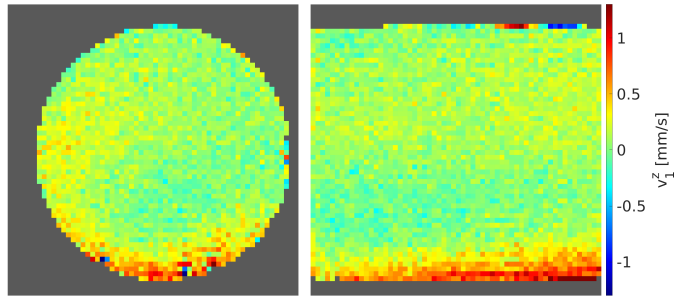
Figure 53: The difference map of both measurements with the tube in the FOV are shown for axial slice 30 and coronal slice 31. The corresponding histogram for the values inside the tube was determined and is shown in fig. 54.

other (fig. 53). Areas with similar non-zero values can be observed locally. For the corresponding histogram (fig. 54), the values are not normally distributed around zero. The maximum value is at $0.09\,\frac{mm}{s}$ and the right flank is broadened.
For both measurements with the tube in the FOV, a polynomial fit of sixth order was done. The resulting maps were subtracted from each other and the mask for the tube was applied (fig. 55). A spatially dependent offset is visible and values lie between $-0.097\,\frac{mm}{s}$ and $0.967\,\frac{mm}{s}$.

Figure 54: Histogram of the difference map. The difference map of both measurements with the tube in the FOV was determined as shown in fig. 53.
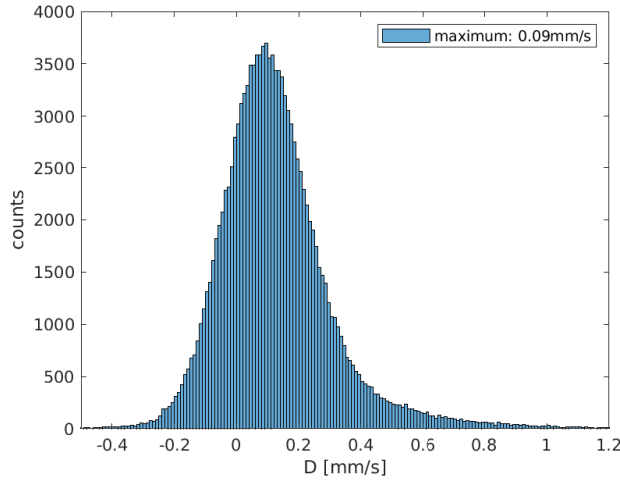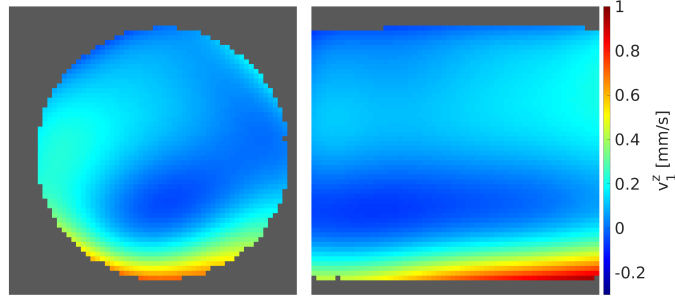

Figure 55: Difference map after subtracting both polynomial fits (both measurements with the tubes located in the FOV). Shown are axial slice 30 and coronal slice 31.

Discussion: In the previous sections it was described that a no-flow reference measurement is necessary to correct phase offsets and guarantee accurate velocity maps. It is desirable to reduce the additional measurement time caused by this reference measurement. For example, this would be interesting if similar velocity measurements are done for several samples. If the accuracy is high enough, one no-flow reference measurement could be done which is used for correcting the velocity map of each sample. Therefore, it is important to evaluate whether shifting of the sample and new settings of the gradient amplifiers due to a new setup influence the accuracy of such reference measurement. For this purpose, the reproducibility of a measurement was analysed in detail.

It was shown that the phase offset of the no-flow velocity map of water located in the OCF or glass tube differ. For the polynomially fitted velocity maps differences up to 2 % of the VENC were observed. This can be explained by magnetic susceptibility effects. The magnetic susceptibility is $\chi = -22.13$ ppm for PLA (the material of the OCF structure) [139] and $\chi = -1.19$ ppm for SiO_2 (the main component of glass) [140]. Thus, depending on whether it is in the OCF or the glass tube, water near the surface experiences a different resonance frequency and consequently a dif-

ferent phase shift when the velocity encoding gradients are applied. Therefore, the velocity maps differ from each other.

It was also of interest if an old reference measurement can be used for correcting another measurement done days later. To simulate such a situation, the gradient amplifiers were turned off and restarted after approximately 15 min. After that, the common adjustments were done again before repeating a no-flow velocity measurement without shifting the sample. For the fits of both measurements with the tube in the FOV, differences up to 5 % of the VENC were observed. It can be assumed that small changes in the electrical components took place after restarting the gradient amplifiers, which had an influence on the eddy currents. Here, thermal effects may play a role. With the gradient amplifiers also the water cooling of the gradient coils is turned off. Thus, the thermal condition after restarting the gradient coils and water cooling may be slightly different, which resulted in different eddy currents.

If such accuracy losses can be tolerated, it could be interesting to use one reference measurement for different samples or several measurement days. However, if highly accurate MRV-maps are needed (for example for cross-validation with CFD simulations), it is advisable to always do a no-flow reference scan immediately before or after the flow measurement to avoid accuracy loss, even if this increases the measurement time.

5.7 Stationary reference

In this section, it is analysed if a stationary sample can be used as reference to correct the phase offset. This technique has the benefit that an additional no-flow measurement would not be necessary and the total measurement time would be halved. Three regions of the measured velocity map were considered for polynomial fitting. In this context, binary masks were determined where the foreground was represented by the porous sample, the stationary phantoms and both together. The resulting fitted maps were used to correct the velocity values in the porous sample and were compared. For quantification, for each of these corrected maps the standard deviation inside the porous sample was determined.

Measurement parameters: A honeycomb structure (3D printed of PLA) with a channel size of $2.4\,\mathrm{mm}$ and a wall thickness between two channels of $0.8\,\mathrm{mm}$ (fig. 16) was located in the glass tube used for flow measurements. Measurements were done without flow of tap water, which was used as the sample fluid. As static reference, tiny glass bottles filled with tap water were attached to the outer wall of the glass tube. Therefore, a larger matrix size and FOV was chosen. The repetition time was $T_\mathrm{R} = 1.5\,\mathrm{s}$. Further measurement parameters are listed in table 8. Noise

Table 8: Parameters for the measurements of the honeycomb without flow. For improved image quality measurements were averaged n-times.

Matrix size	FOV [mm^3]	Voxel size [mm]	VENC$_1$ [$\frac{\mathrm{mm}}{\mathrm{s}}$]	VENC$_2$ [$\frac{\mathrm{mm}}{\mathrm{s}}$]	n_avg	Meas. time [h]
$100 \times 100 \times 100$	$60 \times 60 \times 60$	0.6	35	70	2	8.3

parameters were determined for the low-VENC (first eight echoes). For each pair of consecutive odd and even echo the magnitude images were combined (averaged) and the respective SNR was calculated according to eq. (35) with the mean SNR $= 228.5$, which was used to calculate $\sigma_\mathrm{v} = 0.196\,\frac{\mathrm{mm}}{\mathrm{s}}$ (eq. (34)).

Results: Exemplarily, one axial and one sagittal slice of the velocity map (v_1^z) are shown in fig. 56. A spatially dependent offset can be observed. Also the presence of several air bubbles in the channels can be observed. In the following, polynomial fitting of sixth order is done for different regions of the velocity map by using different binary masks (see fig. 57). The fitted maps are used to correct the offset of the non-fitted velocity map. To quantify the efficiency of each fit, the standard deviation inside the honeycomb structure (see second image in fig. 57) is determined after correction.

Global fitting: A binary mask with honeycomb structure and stationary phantoms as additional samples was determined (see first image in fig. 57). According to the algorithm described in section 5.2, a polynomial fit of sixth order was done for the velocity map (v_1^z) inside this mask. Velocity map and fitted map were subtracted
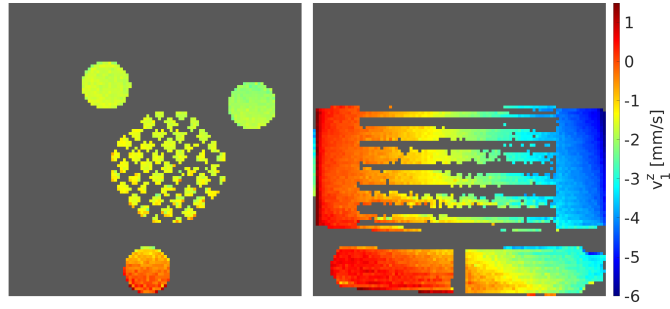
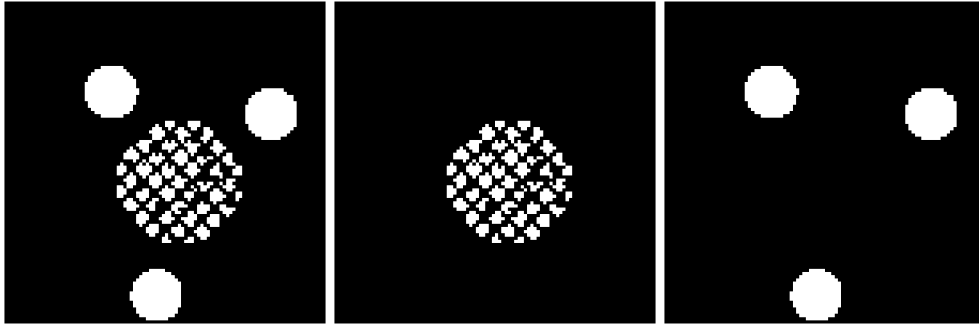Figure 56: For axial slice 46 and sagittal slice 51 of the velocity map v_1^z, a phase offset is visible.

Figure 57: Binary masks were determined for the honeycomb + stationary phantoms (left), only honeycomb (centre) and only stationary phantoms (right). Shown is axial slice 46.

from each other. As an example, slices of the resulting maps are shown in fig. 58. For the stationary references but also the honeycomb structure it is visible that the values in the difference map are distributed about zero. No significant offsets are present. Considering only the honeycomb structure itself (see second image in fig. 57) for the standard deviation a value of $0.228\,\frac{mm}{s}$ was determined.

Fitting for the honeycomb: By using a suitable binary mask, only the velocity values in the honeycomb structure were considered for fitting (see second image in fig. 57). The values in the stationary reference were ignored. Fitting was done for a sixth order polynomial. Velocity map and fitted map were subtracted from each other as shown in fig. 59. Considering only the honeycomb, in the resulting difference map a standard deviation of $0.270\,\frac{mm}{s}$ was determined.

Fitting for the stationary reference: Only the stationary references (see third image in fig. 57) were considered for the sixth order polynomial fitting. Fitted map and difference map are shown in fig. 60. Values distributed about zero are visible for the static references. However, for the honeycomb large areas with similar non-zero values are present. The standard deviation in the honeycomb structure is $0.448\,\frac{mm}{s}$.

64
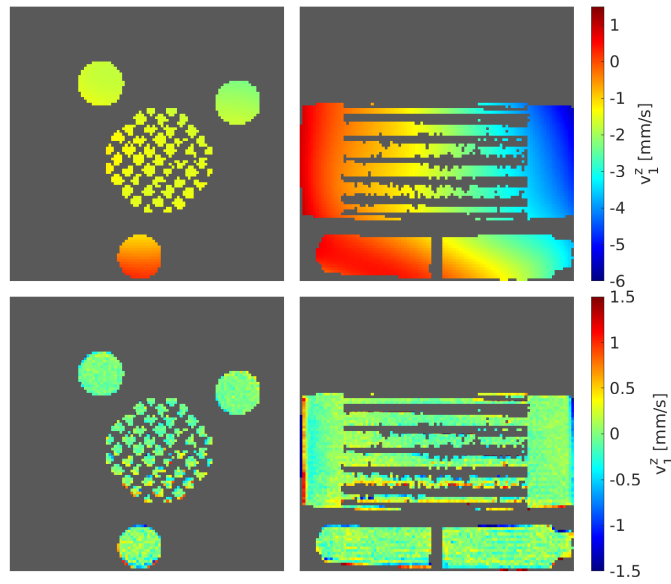
Figure 58: The velocity map was fitted with a polynomial of sixth order (top row). For offset correction, velocity map and fitted map were subtracted from each other (bottom row).
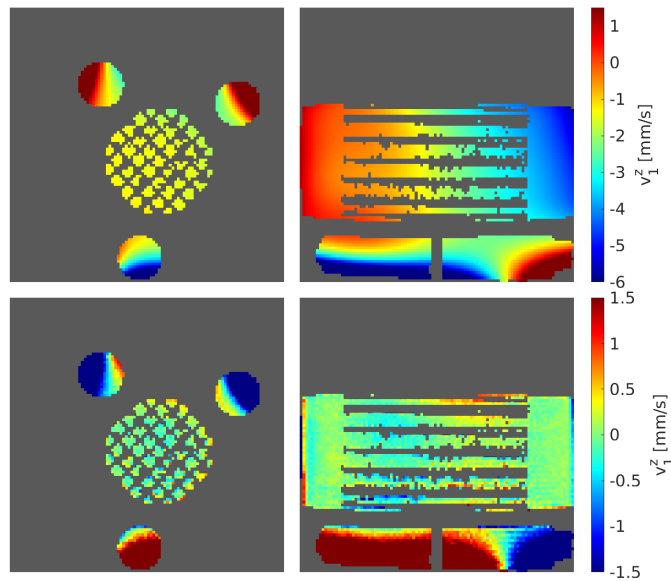
Figure 59: Only the velocity values in the honeycomb structure were considered for fitting with a sixth order polynomial (top row). When subtracting the fitted map from the velocity map, also the stationary phantoms were considered (bottom row).

Flow measurements: Velocity maps with flow were offset corrected by the no-flow maps, for which a global fit was done (honeycomb structure + stationary phantoms). For some axial slices, the resulting maps are shown in fig. 61. At some positions, gaps are visible in the honeycomb structure. It can be assumed that these belong to air bubbles, which adhered at the wall and were not removed by the flow.

65
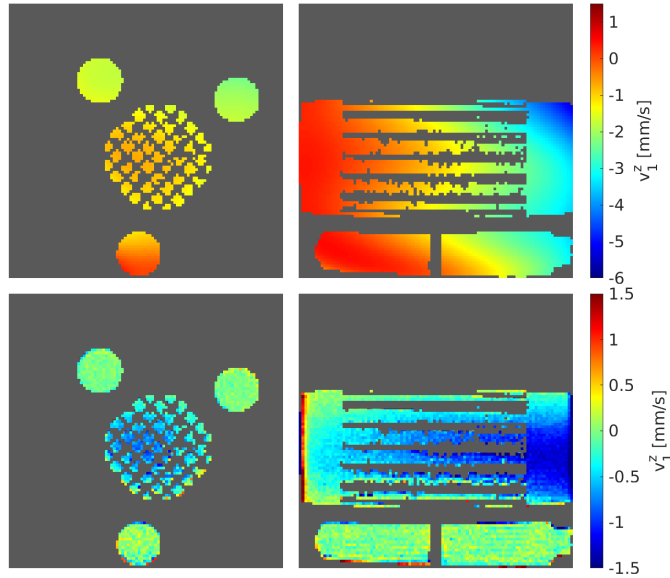
Figure 60: By using a dedicated binary mask, a polynomial fit was done only for the velocity values inside the stationary phantoms (top row). When doing the subtraction of fitted map and velocity map from each other, the stationary phantoms and the honeycomb structure were considered (bottom row).

Discussion: The accuracy of the phase correction by the polynomial fits is evaluated by the standard deviation. As reference, the standard deviation is considered if voxel-wise subtraction of the reference measurement was done. The calculated value was $\sigma_v = 0.196 \frac{mm}{s}$. Thus, for voxel-wise subtraction the standard deviation would be $\sqrt{2} \cdot 0.196 \frac{mm}{s} = 0.277 \frac{mm}{s}$. Polynomial fitting was done for three different regions of the velocity map. The corresponding (normalised) standard deviation is given in table 9.

Table 9: Different regions for the velocity map v_1^z were considered for fitting (polynomial of sixth order). For the honeycomb structure, the fit was additionally done for the binary mask BM_1 (including the edge voxels). The fitted map was subtracted from the non-fitted one and the standard deviation inside the honeycomb structure was determined. Values were normalised to the standard deviation if voxel-wise subtraction was done for offset correction.

offset fitted within	$\sigma_v[\frac{mm}{s}]$	σ_v (normalised)
honeycomb + stationary phantom	0.228	0.82
honeycomb	0.270	0.97
honeycomb (BM_1)	0.233	0.84
stationary phantom	0.448	1.62

It is visible that the lowest standard deviation is present if the honeycomb structure + the stationary phantoms are used for fitting. The standard deviation is slightly larger if only the honeycomb structure is used. This can be explained by the algo-
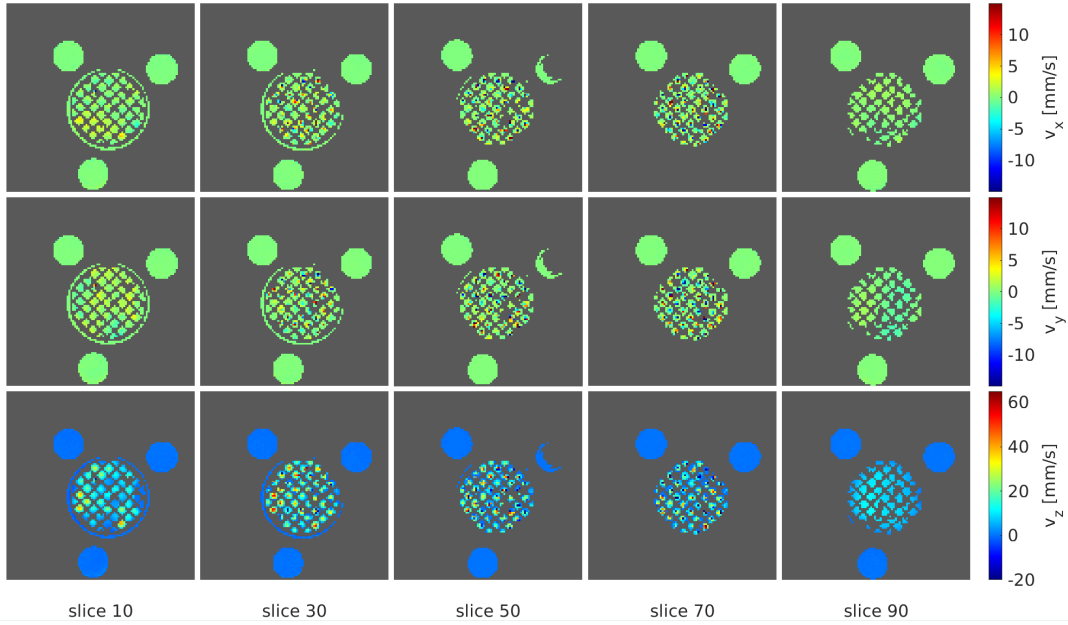
Figure 61: A global polynomial fit of sixth order was done for the no-flow maps (binary mask for honeycomb structure + stationary phantoms). Fitted maps were subtracted from the one acquired with flow. Maps with low-VENC were unwrapped by using the high-VENC data. Unwrapped and high-VENC maps were weighted averaged. For the resulting maps, several axial slices are shown. For fixation in the glass tube, seal tape was wrapped around the honeycomb structure. For some slices, the water filled gaps between honeycomb and glass vessel appear as "rings" with values about zero. It can be assumed that gaps in the honeycomb structure belong to air bubbles.

rithm, which is used to set the binary mask for which the fit is done (for details see section 5.2). Here, all edge voxels are ignored. Since the honeycomb structure has only 2.4 mm thin channels and in some channels unwanted air bubbles were present, at the voxel size of 0.6 mm there were several voxels being ignored since they are located at the surface. Thus, the number of voxels for the fit is rather low and the accuracy of the fit is reduced. However, it must be considered that if no outside positioned static phantoms were present, a smaller FOV could be chosen. For a constant matrix size, this would result in a smaller voxel size and a larger number of voxels for the fit. In this case, a higher accuracy could be expected.

For comparison, the polynomial fit was also done by using all non-zero voxels of the binary mask BM_1 of the honeycomb structure (including the edge voxels) for fitting. The resulting (normalised) standard deviation after correction of the non-fitted map is given in table 9. It is visible that in this case the accuracy is increased and the standard deviation is similar to the one acquired if honeycomb structure + stationary phantom are used for fitting.

Considering only the stationary phantom for the fit results in a large standard deviation for the honeycomb. Fitting for the external stationary phantoms does not accurately describe the phase offset in the honeycomb structure.

In the previous sections, phase offset correction for MRV flow measurements was

67

realised by repeating the measurement without flow and subtract the velocity map from the one acquired with flow, which doubles the measurement time. For reduction of the measurement time, it would be useful to do the offset correction by considering external positioned stationary phantoms, which makes the no-flow measurement unnecessary. However, it was shown that such correction is not very accurate. If the geometry of a sample allows it and the flow field is not influenced, the sample could be designed such that stationary regions are present inside the sample. For example, this could be achieved by 3D printing and creating cavities in the sample wall, which can be filled with fluid. Using these cavities for fitting should be more accurate than using external positioned phantoms. Furthermore, the size of the FOV would not need to be increased.

5.8 Conclusion

If flow is realised by a hydrostatic pump, irregularities like pulsation can be neglected. However, the setup of such a pump, as well as the setting of the desired flow rate, is associated with a certain amount of effort. In these measurements, a peristaltic pump was used and larger variations caused by pulsation effects could be determined in the measured velocity maps. In further measurements, an analysis of such pulsation effects should be done for different pump systems. However, such an analysis was beyond the scope of this work.

Generally, phase offsets introduced by eddy currents are a problem in MRV measurements, since they produce spatially dependent offsets in the phase maps. A minimisation of eddy currents could be achieved by optimisation of the sequence, for example by reducing the gradient strength. However, since this will make it necessary to increase the gradient duration and thus increases the echo time, it has negative effects on the SNR and increases displacement errors.

Also, phase offsets can be corrected by doing an additional measurement without flow and subtract the resulting map from the one acquired with flow. By voxel-wise subtraction, the SNR is worsen by $\sqrt{2}$. To minimise this SNR loss, a common technique is to polynomially fit the no-flow map before subtracting [41, 117, 118]. An algorithm was presented to ignore voxels at the surface and therefore reduce partial volume effects when fitting. Since the order of the polynomial has an impact on the accuracy of the fit, it is advisable to determine the optimum for a measurement. In particular, since eddy currents depend on the strength and direction of the applied gradients, the phase offset differs for measurements with different parameters (like for example different VENC-values or FOV). It should be noted that for a too high order of the polynomial overfitting may occur. However, for the shown data no overfitting could be observed for the highest order of six.

The no-flow phase map may also be denoised by using median-filtering. For best accuracy, different filter sizes should be tested. The change of the offset in the neighbourhood of the voxel to be filtered should be small compared to the noise values and thus depends on measurement parameters such as gradient strength and the SNR.

Crusher gradients were used to suppress artefacts caused by non-ideal refocusing pulses. Additionally, spoiler gradients at the end of the sequence were used to

suppress artefacts caused by residual transverse magnetisation. However, for the measured v_z it could be noticed that the amplitudes of these gradients were not sufficient to remove all artefacts. Remaining artefacts were eliminated by phase cycling the RF excitation pulse. Thus, the accuracy of the polynomial fits could be improved.

It was shown that small changes in a system, like shifting of the sample, causes a noticeable change of the phase offset (depending on the spatial position, up to 2% of the VENC). The same applies for restarting the gradient amplifiers (a change in the offset up to 5% of the VENC). It would reduce measurement time if the same reference measurement is used for the phase correction of different measurements. However, for high accuracy it is advisable to perform an extra reference measurement each time.

In medical application, a reference measurement without flow is not possible. Therefore, commonly surrounding static tissue is considered and polynomially fitted for phase offset correction. However, it was shown that using outside positioned static phantoms for offset correction involves inaccuracies. Outside the medical field, e.g. in the examination of porous media, it is advisable to always carry out an additional no-flow measurement as a reference in order to achieve the highest possible accuracy. If the geometry of a sample allows it, it would also be a conceivable alternative to introduce static phantoms inside the 3D-printed sample (e.g. liquid-filled spaces in the sample wall). Signals from these static phantoms could then be polynomially fitted to correct the phase offset.

6 Comparison of MRV measurements and CFD simulations

6.1 Introduction

Over the last decades, CFD simulations [24, 141] became an important tool to numerically investigate transport phenomena including mass, momentum and heat. These include problems in fluid mechanics like, for example, the calculation of the drag coefficient of vehicles or the design of porous media (like catalyst supports) that are flowed through by liquids or gases.

In CFD simulations, a system of equations is solved, including the Navier-Stokes equations and a mass balancing continuity equation. In addition, there are the boundary conditions at the boundaries of the calculated geometry and the initial condition to start the calculation. The big advantage of CFD is its flexibility and ability to control the conditions with the help of an adequate computional power compared to experiments. Therefore, it is widely used in the industry since CFD simulations offer a cost-effective alternative to experimental techniques. Choosing the appropriate numerical setup of CFD studies is important to represent a realistic approximation of the systems. Therefore, it is necessary to validate the results of CFD simulations with the corresponding experimental data. Once an appropriate and validated numerical setup is chosen, it can be implemented for further investigations with more flexibility and without possible measurements errors. In addition, CFD simulations can be used for cross validation of experiments for identification of the limitation and possible sources or errors.

The modelling using CFD simulations has been widely used to investigate local velocity [142, 143], temperature [70, 144] and concentration fields [145] within monolithic catalyst supports.

The implemented numerical setup of CFD simulations should be discretized and solved for the geometry of the investigated systems. There are two options to generate the digital geometry, which is used for the simulations. The first option is to scan the monolith by μCT, which allows to use its morphology in CFD simulations. The second option is to artificially generate a monolith, which is used in CFD simulations. If additional measurements shall be done, this geometry can be 3D printed. Afterwards, these utilized 3D geometries have to be segmented into the smaller control volumes for solution of the implemented numerical setup. The segmented geometry of the investigated system are known as mesh and the averaged size of each cell controls the resolution of the CFD simulations.

In [143] the flow of dimethyl sulfoxide solution within a transparent 20 PPI glass OCF was investigated by μPIV measurements and μCT-based CFD simulations. At three different positions, the time-averaged velocity fields from μPIV measurements were qualitatively and quantitatively compared with velocity fields from CFD simulations. Even though the whole geometry of the glass OCF was used for the measurements, only a part of the OCF - a representative elementary volume (REV) - was considered in the simulations. This neglects the effect of neighbouring pores on the velocity field and causes some of the reported discrepancies between numerical and experimental data. The flow of SF_6 within a diesel particulate filter was investi-

gated by 3D CFD simulations and MRV measurements [146]. A good agreement was reported between the obtained CFD and MRV velocity profiles using a high spatial resolution ($0.14 \frac{mm}{voxel}$) of the obtained velocity fields. In [40], flow through a Schwarz Diamond TPMS (triply periodic minimal surface) column was investigated. The agreement between MRV measurements and CFD simulations was also evaluated by comparing one-dimensional velocity profiles through the sample. However, for both works [40, 146], CFD and MRV velocity pattern were not directly compared. In [25], a full-field analysis of methane flows within a 20 PPI OCF by μCT-based CFD simulations and MRV measurements was performed. The agreement between simulated and experimental velocity fields was evaluated by slice-wise determining a similarity index. An average similarity index, which is by definition 1 for identical images, of about 0.7 was specified. The low spin density of methane gas led to rather low SNR. For better SNR, in [147] we used the liquid polyethylene glycol as fluid. Additionally, in [147] measurements were done with a smaller voxel size and a larger similarity index was found (average value of 0.83). However, for both works [25, 147], only the axial component of the velocity map was considered.

In this section, the same 10 PPI OCF structure as in [147] was used as sample. All three components of the velocity map (v_x, v_y, v_z) for water flow in the OCF structure are considered. Measurements were done with the multi-echo sequence (as presented in section 4) and are compared with CFD simulations.

6.2 MRV velocity maps

For the comparison with CFD simulations, the measured velocity maps described in section 4 are used. Offset correction was done by using polynomially fitting the no-flow velocity fields by third (v_x, v_y) and sixth order (v_z). For an increased VNR, unwrapped and high-VENC maps were weighted averaged.

6.3 CFD simulations

In collaboration with Mehrdad Sadeghi (working group of Prof. Dr.-Ing. Jorg Thöming, University of Bremen), CFD simulations were carried out using the finite-volume CFD software OpenFOAM (version 10). The steady-state water flow in this study was considered incompressible since the Mach number (Ma) is lower than 0.3 (see section 2.1). The solver simpleFoam was used within the OpenFOAM library to solve the governing equations of laminar and steady-state flows. This solver simpleFoam solves the pressure-velocity equation using the SIMPLEC (semi-implicit method for pressure-linked equations-consistent) algorithm [141]. Constant superficial velocities were considered at the inlet ($u_{inlet} = $ const.) and the outlet pressure was set zero ($p = 0$). A no-slip boundary condition ($u = 0$) was considered for the tube walls and the surface of the OCF. Mehrdad Sadeghi reconstructed the 10 PPI OCF from μCT images by using the image processing software ImageJ (version 1.52a, https://imagej.nih.gov/ij/) and Meshlab (version 1.3.2, http://www.meshlab.net/) as described in [25]. The morphology of the 3D-printed OCF was generated by modifying the original μCT images in ImageJ to have circular outer geometry and perfect fitting into the reactor, which prevents flow bypasses. The computational

mesh was generated via the commercial meshing software cfMesh (version 1.1.2, https://cfmesh.com/). Grid independency tests revealed computational networks with a minimum of 9.4 million cells required for the OCF structure.

6.4 Matching of MRV and CFD maps

The simulated CFD and the measured MRV velocity maps were loaded in Paraview (version 5.10). For the best agreement, both datasets were manually shifted in z-direction relative to each other. Since the CFD dataset is longer in z-direction, a 36 mm long (analogous to the MRV dataset) element from the central part was exported for further analysis in Matlab (fig. 62).
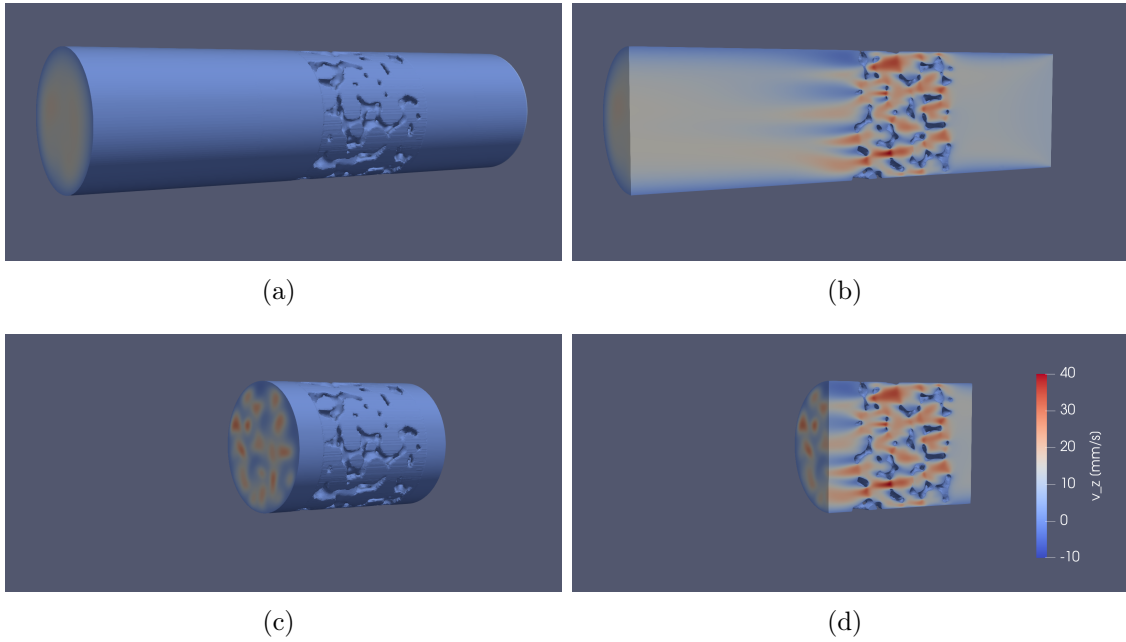

(a)　　　　　　　　　　　　　　　(b)

(c)　　　　　　　　　　　　　　　(d)

Figure 62: The CFD velocity map (a), which was loaded in Paraview, was cut to the length of the MRV map (c). For better visualisation for the v_z map in this figure, cross sections are shown (b,d).

The CFD data have a higher resolution than the MRV data. In order to make these two data sets comparable, the CFD data were mapped on the grid given by the MRV data. Afterwards, the CFD data were convolved to the same resolution as the MRV data. The CFD velocity map was rotated (1° to 360°) and for each rotation angle, the similarity index r between CFD and MRV velocity map was determined slice-wise by using the MATLAB-function corr2:

$$r = \frac{\sum_m \sum_n (A_{mn} - \bar{A})(B_{mn} - \bar{B})}{\sqrt{(\sum_m \sum_n (A_{mn} - \bar{A})^2)(\sum_m \sum_n (B_{mn} - \bar{B})^2)}} \quad (59)$$

Here, CFD and MRV velocity fields are depicted by the matrices A and B with the mean values $\bar{A}$ and $\bar{B}$. The corresponding values for the similarity index are shown in fig. 63. For the optimum rotational angle, the corresponding similarity indices
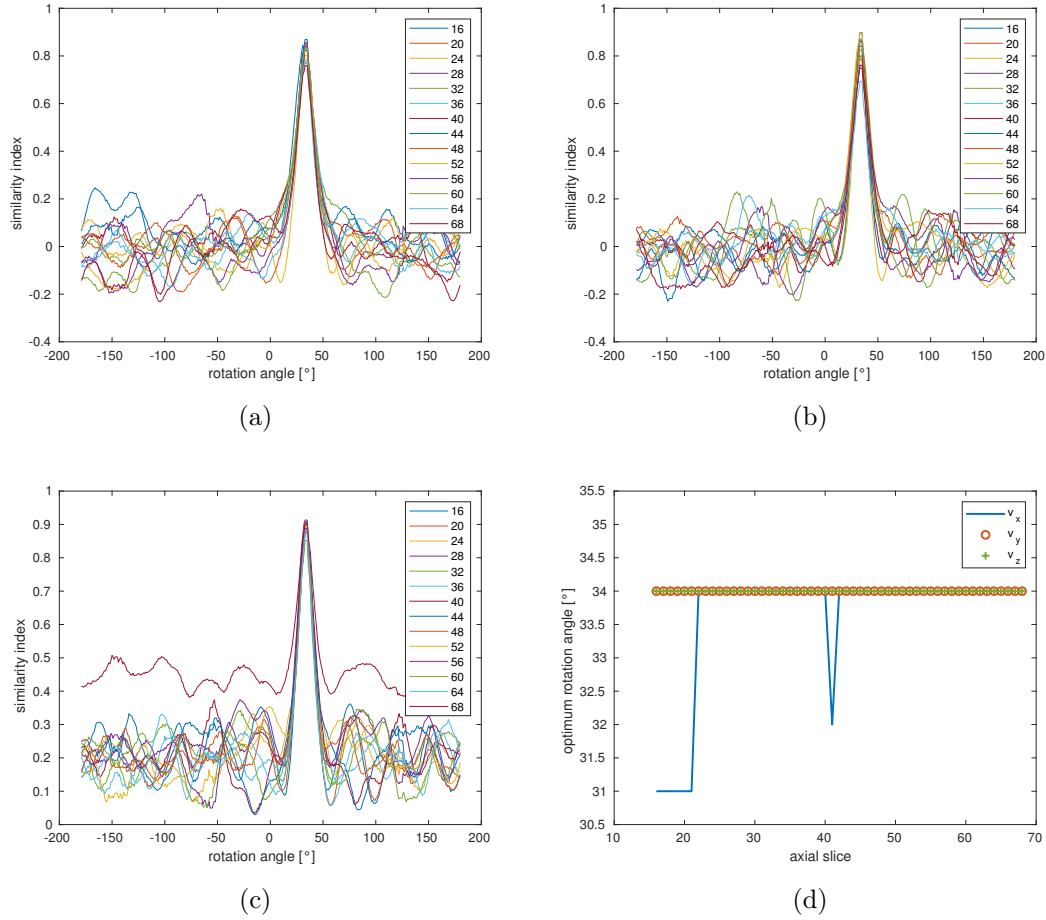
Figure 63: The CFD velocity maps were rotated from 1° to 360° and for each rotation angle the similarity index between CFD and MRV velocity maps was determined slice-wise. Exemplarily, the corresponding plots are shown for some axial slices of v_x (a), v_y (b) and v_z (c). For most axial slices the optimum rotational angle is 34°. However, for few slices the optimum is at 32° or 31° (d).

range from 0.76 to 0.87 (v_x), 0.69 to 0.90 (v_y) and 0.85 to 0.91 (v_z). For most axial slices, the optimum rotational angle is at 34°, but in few cases it is 32° or 31°. For the optimum rotation angle 34°, the CFD velocity maps were shifted in axial direction relatively to those acquired by MRV measurements. The similarity index between both velocity maps was determined slice-wise. The mean value of the similarity index was plotted against the corresponding shift position (fig. 64). For all velocity components, a maximum is visible for the case without shift. For increasing shift (in negative and positive direction), the similarity index steadily decreases.

6.5 Velocity maps

As described before, the optimum rotational angle was determined with a value of 34°. MRV velocity maps and by 34° rotated CFD velocity maps are shown in fig. 65. Visually, a high similarity between MRV and CFD velocity maps is visible.
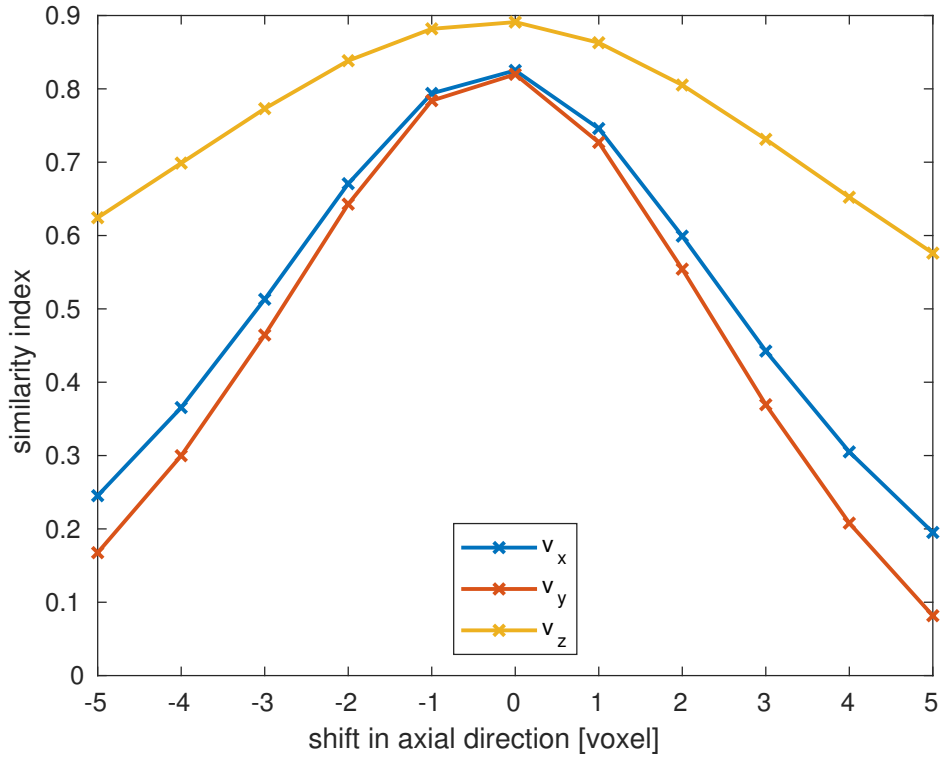
Figure 64: The CFD velocity map was rotated by the optimum angle 34°. Afterwards, it was shifted in axial direction relatively to the MRV velocity map. For each case, the mean value of the similarity index over all slices in the OCF was determined.

In fig. 66, the binary mask BM_2 (see section 5.2) was applied to ignore the voxels at the surface. By applying a dedicated binary mask, the inner region of the OCF was ignored and only the voxels at the surface were considered fig. 67. In fig. 68, the similarity index was determined slice-wise for different regions of the velocity maps. For all three velocity components it is visible, that the highest similarity index is present if the voxels located at the surface are ignored. Mean values are shown in table 10. The lowest similarity index is present if only the voxels located at the

Table 10: Mean values of the slice-wise determined similarity indices from fig. 68.

	$\text{sim}(v_x)$	$\text{sim}(v_y)$	$\text{sim}(v_z)$
whole OCF	0.83	0.82	0.89
only surface	0.77	0.77	0.83
without surface	0.88	0.88	0.95

surface are considered.
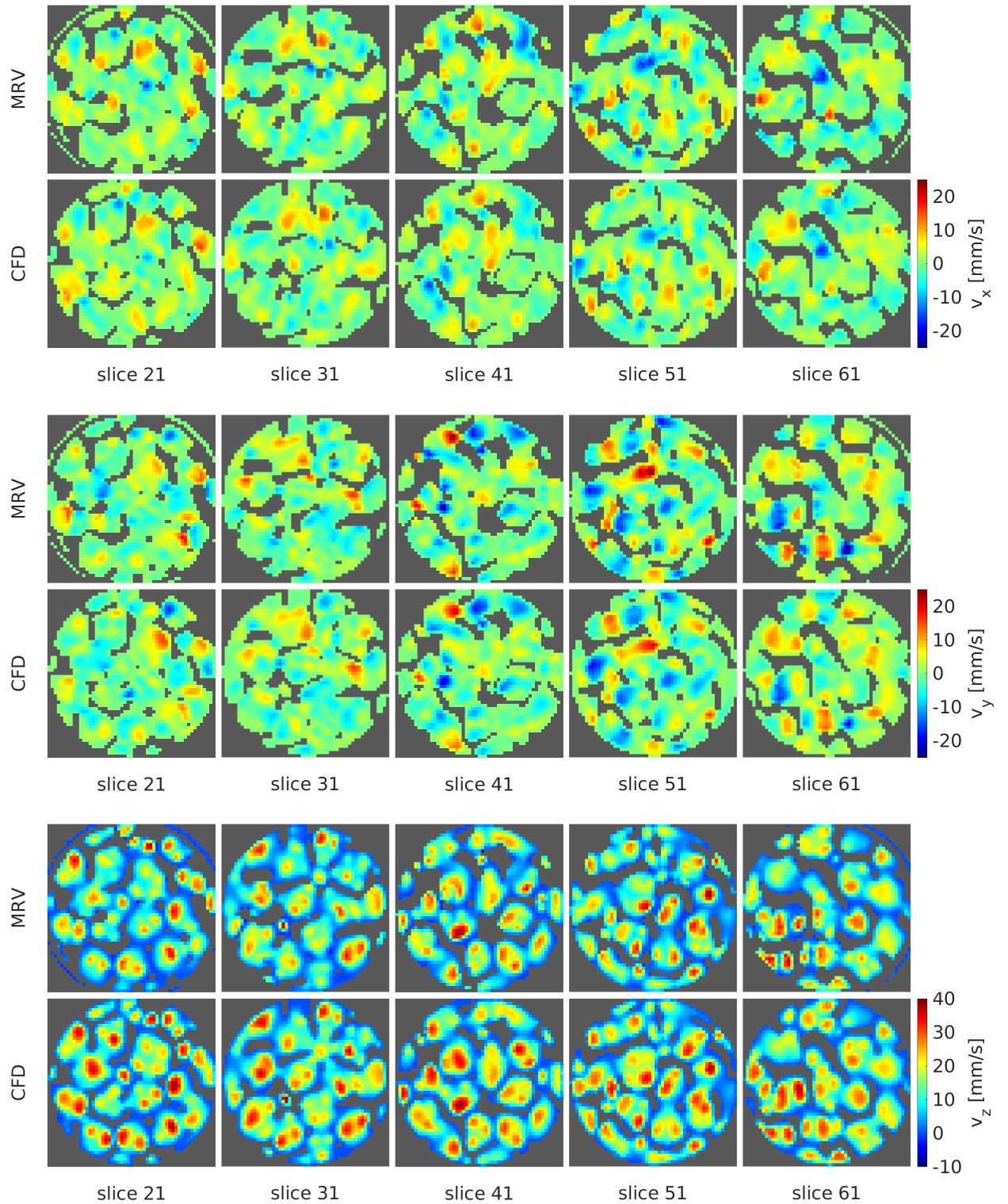
Figure 65: For the velocity maps v_x, v_y and v_z determined by MRV measurements and CFD simulations, exemplarily some axial slices are shown. The shown CFD velocity maps were rotated by the optimum rotation angle.
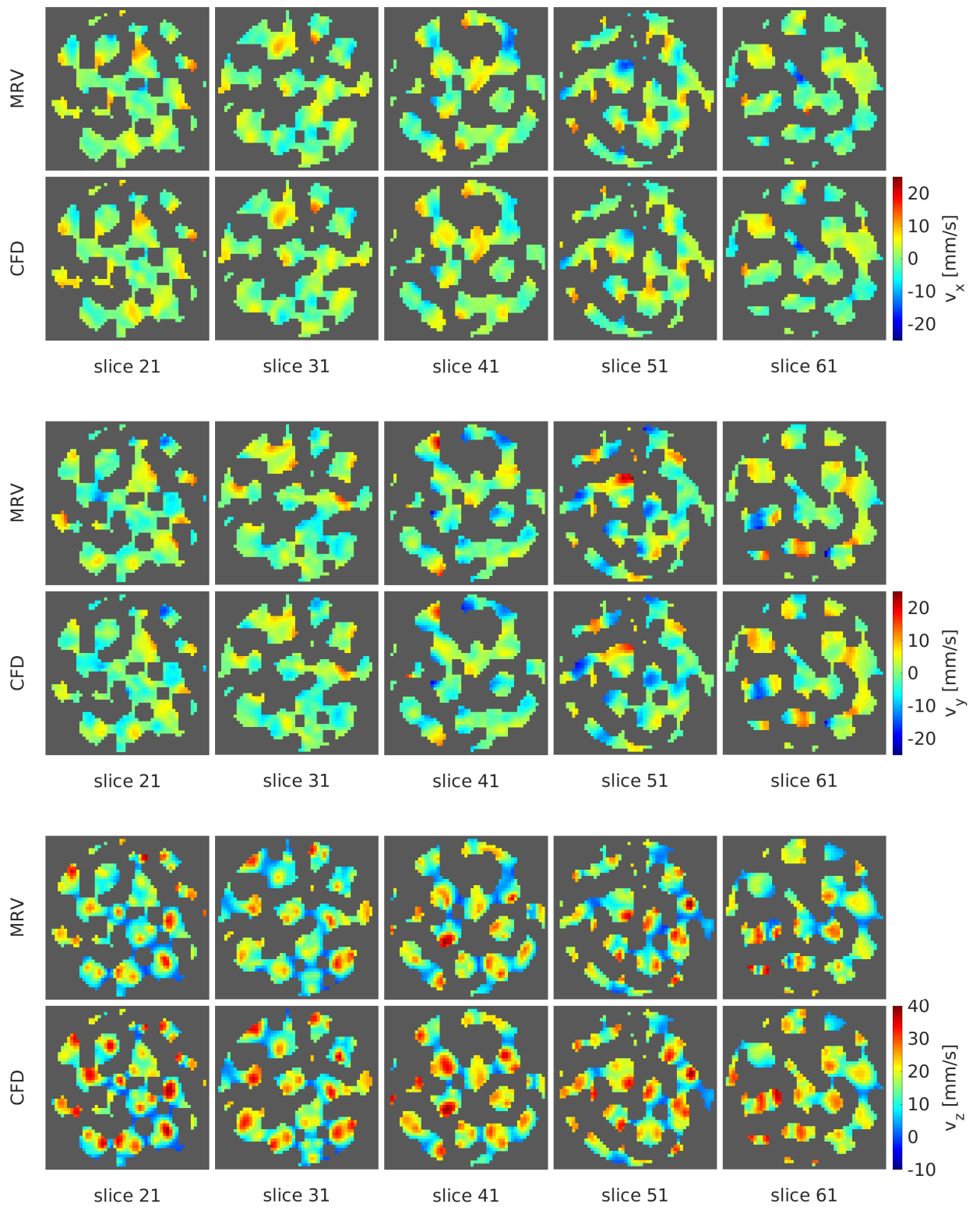
76

Figure 66: To ignore voxels at the surface, this binary mask BM₂ was applied to the maps shown in fig. 65.
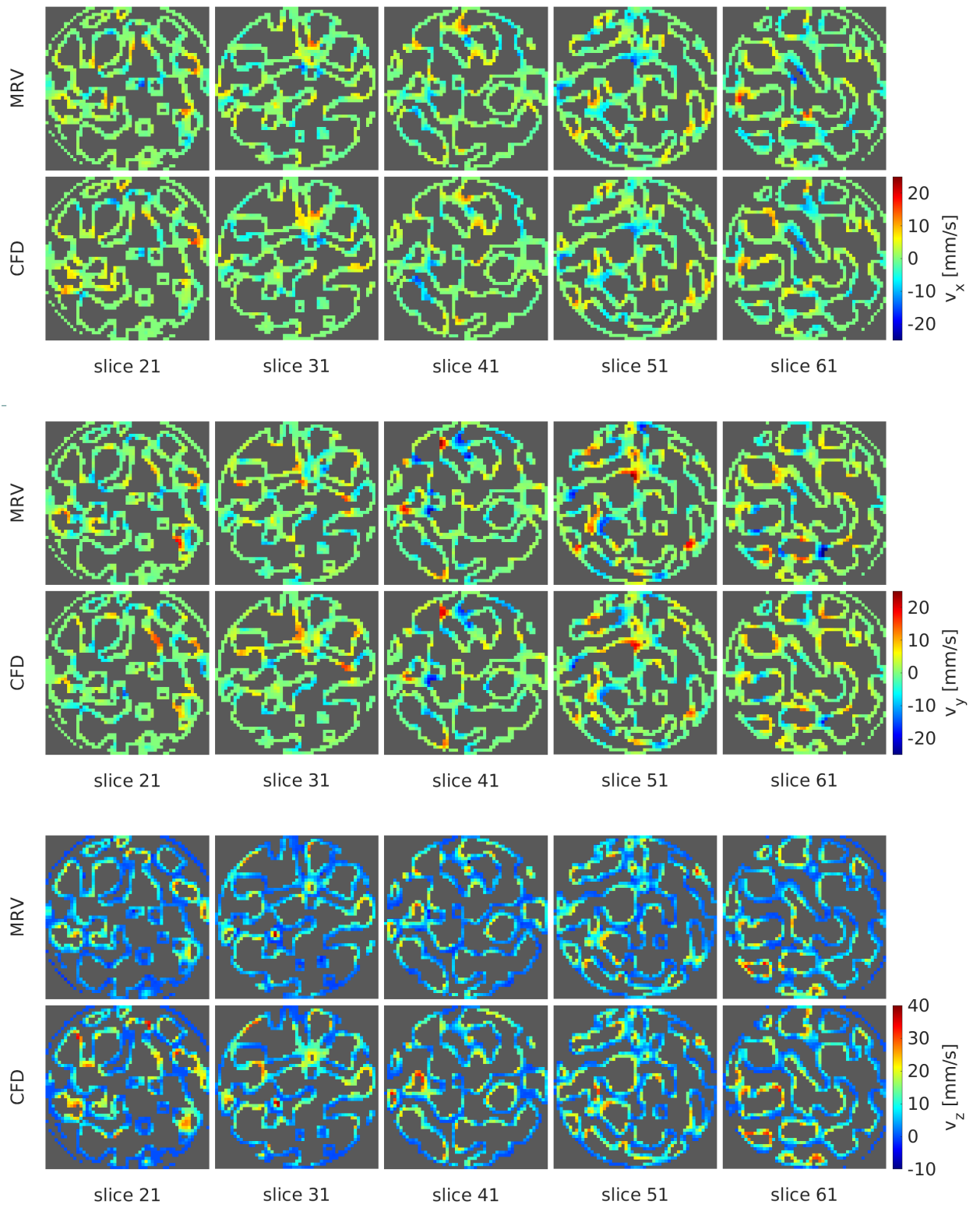
Figure 67: A dedicated binary mask was applied to ignore the voxels located at the surface for the velocity maps.
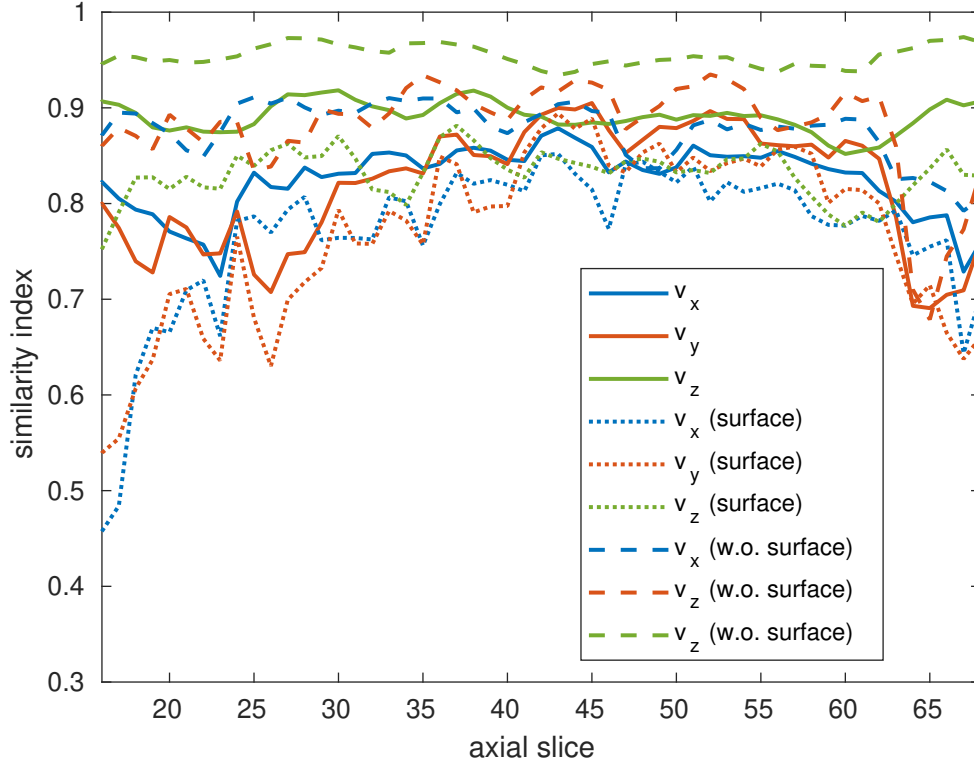
Figure 68: Three different binary masks were applied to the velocity fields (v_x, v_y, v_z) to consider different regions of the OCF structure. The whole OCF (solid line), the OCF without the surface (dashed line) or only the surface (dotted line) was considered. For each case, the similarity index was determined slice-wise.

6.6 Discussion

In this section, velocity maps acquired from MRV measurements and CFD simulations were compared. For a meaningful comparison, the velocity maps were matched by determining the similarity index at different rotation angles and different shift positions in axial direction of the CFD velocity maps. At the optimum rotational angle, similarity indices between 0.76 to 0.87 (v_x), 0.69 to 0.90 (v_y) and 0.85 to 0.91 (v_z) were found.

However, if only the surface of the OCF is considered, the similarity index becomes lower. Several reasons may be responsible for this. A small geometrical offset between MRV and CFD maps would cause the largest velocity difference near the surface due to the parabolic shape of the laminar flow (see fig. 33). Also, in the experiments it could not be guaranteed that water was completely free from air bubbles, which influenced the flow behaviour. For fast velocities they may be easily removed, while for regions with slow velocities it was more likely that air bubbles remain at the surface of the OCF and thus affect the similarity index more. This is the case for the surface, where preferably slow velocities are present. The effect of these air bubbles could not be quantified because their size was not large enough to be directly resolved in the MRI images. Since the presence of air bubbles would

reduce the amount of water, the SNR (and consequently the VNR) in the affected voxels would be lower. However, these minor SNR losses could not be distinguished from the partial volume effect as air bubbles occur at the surface of the structure. Another reason for the decreased similarity index are the low velocity values at the surface since the VNR is proportional to the velocity (see eq. (36)). Furthermore, the partial volume effect at the surface may result, in addition to reduced SNR, in overestimated velocity values [30, 31], which also lowers the similarity index for the comparison between MRV and CFD maps.

In section 4 it was mentioned that the time delay between spatial encoding and velocity encoding causes displacement errors for the MRV measurement. For the considered measurement, a value of $displacement = 0.36$ voxels was determined. Since this is the maximum value, in most regions of the OCF the displacement error is lower. However, it can be assumed that displacement errors, which play a larger role for the regions inside the OCF due to faster velocities, have a negative impact on the similarity index. Even though, it is visible that the effects of the voxels at the surface have a larger negative contribution on the similarity index.

6.7 Conclusion

A comparison between MRV and CFD velocity maps was done by considering the similarity index. Values were larger than the mean similarity index reported in [25] (around 0.7), where MRV measurements were done for methane flow in a 20 PPI OCF structure at a voxel size of $0.8 \frac{\text{mm}}{\text{pixel}}$. In [147], we used polyethylene glycol as fluid, which has a larger spin density than gaseous methane and therefore enables a better SNR. A 10 PPI OCF structure was measured at a voxel size of $0.53 \frac{\text{mm}}{\text{pixel}}$. The better SNR, the smaller voxel size and the larger pores of the sample have a positive impact on the similarity index. In addition, the dual-VENC technique used allowed for a higher VNR. Due to its larger SSA, partial volume effects should have a larger effect for the 20 PPI OCF structure used in [25] and thus reduce the similarity index.

Since measurements in [147] were only performed for the axial velocity and another MRV sequence was used, similar measurements for the 10 PPI OCF structure were performed with the multi-echo sequence presented in this work. In [147], a mean value for the similarity index of 0.83 was found. Similar values were also determined in this work. Depending on the velocity component, the mean value was between 0.82 and 0.89 (considering the whole OCF structure). By ignoring the surface of the OCF structure and considering only the inner region, larger mean similarity indices between 0.88 and 0.95 were found.

In section 5, the effect of pulsation of the flow on the measured velocity maps was described. It can be assumed, that this pulsation was another reason for the similarity index being below 1. It was already mentioned that further measurements should be done with a pump with lower pulsation. This would also be interesting to quantify the effect of pulsation on the similarity index.

Slow and fast flow regions in the OCF were analysed separately. It was found that the similarity index is larger if only fast flow regions are considered. It is decreased, if only slow flow regions are considered. Different reasons, like larger velocity changes

due to the parabolic shape of the laminar flow, air bubbles at the sample wall, partial volume effects and lower VNR, were discussed.

7 Summary and Outlook

In this work, methods were described to achieve a high accuracy for MRV measurements and reduce systematic errors for water flow through an OCF structure and a honeycomb structure. For an improved Velocity-to-Noise Ratio (VNR), the dual-VENC technique was used. The optimal ratio between high- and low-VENC (which is proportional to the VNR) was calculated to achieve the highest possible VNR improvement. However, since pulsation effects were observed in the measured velocity maps, a lower ratio than the theoretical optimum was used.

A new multi-echo sequence for 3D imaging of 3-directional velocity with optimised timings was proposed to achieve a compromise between VNR, total measurement time, spatial resolution and displacement errors. A dual-VENC encoding scheme was achieved with different velocity encoding steps for the individual echoes. Phase errors originating from coherence pathways were corrected by combining odd and even echoes and by a combination of crusher gradients around the refocusing pulses and phase cycling for the excitation pulse. For a good SNR, the repetition time T_{R} was optimised for tap water as fluid in a PLA-based OCF structure.

Remaining phase errors due to eddy currents were corrected by subtracting velocity maps acquired with and without flow. For such a subtraction, the noise values of both maps accumulate and decrease the SNR by $\sqrt{2}$. To reduce this SNR loss, no-flow maps can be polynomially fitted before being subtracted from the map with flow. As a new and alternative technique for reduced SNR loss, median filtering of the no-flow map was proposed. Both methods showed similar values for the standard deviation σ_{v}.

However, the advantage of polynomial fitting over median filtering is that parts of the image can be used as the basis for correcting the phase offset in the entire image. This is especially advantageous for systems where the flow cannot be turned off (as for example in the medical application). For offset correction, the signal phase from surrounding tissue, where stationary spins are present, is polynomially fitted and the resulting fitted map is used to correct the whole velocity image. In case of porous media, a stationary phantom may be introduced near the sample. Using this phantom for the polynomial fit makes the no-flow measurement superfluous and the total measurement time is halved. The benefit of such technique was analysed quantitatively.

As an alternative method to save total measurement time, it was analysed whether the same no-flow velocity map can be used to correct the phase offset for a series of measurements. However, for both techniques systematic errors were found. The most accurate results were obtained if an additional no-flow scan is done individually for every measurement. Therefore, such an additional no-flow measurement should always be done if highly accurate velocity maps are needed and the time for the additional measurement is available.

For cross-validation of CFD simulations, measurements are indispensable. Therefore, in this work velocity maps resulting from MRV measurements and CFD simulations for an OCF structure were quantitatively compared, after applying an algorithm to match them. MRV and CFD based velocity maps were compared by a structural similarity index. The determined values were larger than in a similar

analysis previously carried out with methane gas as the fluid in an OCF. Besides the smaller voxel size, larger pores and higher spin density of liquids and thus a better SNR of water compared to methane gas, additional accuracy was achieved by the dual-VENC technique used, which improves the VNR. The surface and the inside of the OCF were considered separately. A decreased similarity index for the surface caused by partial volume effects, lower VNR, the shape of the laminar flow profile and the presence of small air bubbles could be determined.

Outlook: The following ideas should be pursued to continue the work described in this thesis.

For further reduction of the total measurement time, the proposed multi-echo sequence could be combined with different acceleration methods like compressed sensing [39, 55] or parallel imaging [116].

Measurements done with a different setup or different pump systems would be helpful to better understand the impact of pulsation effects on the measured velocity maps. Using a system with lower pulsation would also allow to choose a larger ratio between high- and low-VENC and thus improve the VNR improvement for the dual-VENC technique.

If the flow through a sample cannot be turned off, outside positioned stationary phantoms can be used for phase offset correction. However, this makes it necessary to increase the FOV. Instead, for a future analysis porous media could be 3D printed in such a way that inside the struts of the sample stationary regions filled with liquids are present to be polynomially fitted and used for the offset correction. In this work, cross-validation of MRV measurements and CFD simulations were done for a single fluid phase. It would be interesting to adapt the proposed sequence to measure multi-phase flow (fluid-fluid or gas-fluid) and distinguish between the fluids used. Such a distinction could be made, for example, by frequency-selective excitation or the phases could be distinguished by their relaxation times. This would be particularly interesting if combined with numerical simulations. Since such a comparison of MRV measurements and numerical simulations for multiphase flow has not yet been done in the literature, such studies would make an interesting new contribution to current research.

References

[1] Santhi Maniam and Janio Szklaruk. Magnetic resonance imaging: Review of imaging techniques and overview of liver imaging. *World Journal of Radiology*, 2(8):309–322, 2010.

[2] Shreyas S. Vasanawala, Kate Hanneman, Marcus T. Alley, and Albert Hsiao. Congenital heart disease assessment with 4D flow MRI. *Journal of Magnetic Resonance Imaging*, 42(4):870–886, 2015.

[3] Gary H. Glover. Overview of functional magnetic resonance imaging. *Neurosurgery Clinics*, 22(2):133–139, 2011.

[4] Anwar Padhani. MRI for assessing antivascular cancer treatments. *The British Journal of Radiology*, 76(special issue):60–80, 2003.

[5] Bert-Jan De Bondt, Patricia J. Nelemans, Paul A. M. Hofman, Jan W. Casselman, Bernd Kremer, Jos M. A. van Engelshoven, and Regina G. H. Beets-Tan. Detection of lymph node metastases in head and neck cancer: a meta-analysis comparing US, USgFNAC, CT and MR imaging. *European Journal of Radiology*, 64(2):266–272, 2007.

[6] Pavan Tummala, Omer Junaidi, and Banke Agarwal. Imaging of pancreatic cancer: An overview. *Journal of Gastrointestinal Oncology*, 2(3):168–174, 2011.

[7] Hassan Shahid, James F. Wiedenhoefer, Carol Dornbluth, Pamela Otto, and Kenneth A. Kist. An overview of breast MRI. *Applied Radiology*, 45(10):7–13, 2016.

[8] Ashirbani Saha, Michael R. Harowicz, and Maciej A. Mazurowski. Breast cancer MRI radiomics: An overview of algorithmic features and impact of inter-reader variability in annotating tumors. *Medical Physics*, 45(7):3076–3085, 2018.

[9] Lynn F. Gladden, Fernando J. R. Abegao, Christopher P. Dunckley, Daniel J. Holland, Mark H. Sankey, and Andrew J. Sederman. MRI: Operando measurements of temperature, hydrodynamics and local reaction rate in a heterogeneous catalytic reactor. *Catalysis Today*, 155(3-4):157–163, 2010.

[10] Mojtaba Mirdrikvand, Harm Ridder, Jorg Thöming, and Wolfgang Dreher. Diffusion weighted magnetic resonance imaging for temperature measurements in catalyst supports with an axial gas flow. *Reaction Chemistry & Engineering*, 4(10):1844–1853, 2019.

[11] Harm Ridder, Christoph Sinn, Georg R. Pesch, Wolfgang Dreher, and Jorg Thöming. Spatially resolved direct gas-phase thermometry in chemical reactors using NMR. *Chemical Engineering Journal*, 433:133583, 2022.

[12] Jürgen Ulpts, Wolfgang Dreher, Miriam Klink, and Jorg Thöming. NMR imaging of gas phase hydrogenation in a packed bed flow reactor. *Applied Catalysis A: General*, 502:340–349, 2015.

[13] Susithra Lakshmanan, Wessenu A. Maru, Daniel J. Holland, Mick D. Mantle, and Andrew J. Sederman. Measurement of an oil–water flow using magnetic resonance imaging. *Flow Measurement and Instrumentation*, 53:161–171, 2017.

[14] Georg R. Pesch, Harm Ridder, and Christoph Sinn. Operando characterization of heterogeneously catalyzed gas-and multi-phase reactions using nuclear magnetic resonance imaging. *Chemical Engineering and Processing-Process Intensification*, 179:109086, 2022.

[15] Frank Stallmach and Jörg Kärger. The potentials of pulsed field gradient NMR for investigation of porous media. *Adsorption*, 5:117–133, 1999.

[16] Joseph D. Seymour and Paul T. Callaghan. "Flow-diffraction" structural characterization and measurement of hydrodynamic dispersion in porous media by PGSE NMR. *Journal of Magnetic Resonance, Series A*, 122(1):90–93, 1996.

[17] Mojtaba Mirdrikvand, Mehrdad Sadeghi, M. Nurul Karim, Jorg Thöming, and Wolfgang Dreher. Pore-scale analysis of axial and radial dispersion coefficients of gas flow in macroporous foam monoliths using NMR-based displacement measurements. *Chemical Engineering Journal*, 388:124234, 2020.

[18] Stephen D. Senturia and J. D. Robinson. Nuclear spin-lattice relaxation of liquids confined in porous solids. *Society of Petroleum Engineers Journal*, 10(3):237–244, 1970.

[19] Morrel H. Cohen and Kenneth S. Mendelson. Nuclear magnetic relaxation and the internal geometry of sedimentary rocks. *Journal of Applied Physics*, 53(2):1127–1135, 1982.

[20] Andrew J. Sederman, Michael L. Johns, Allan S. Bramley, Paul Alexander, and Lynn F. Gladden. Magnetic resonance imaging of liquid flow and pore structure within packed beds. *Chemical Engineering Science*, 52(14):2239–2250, 1997.

[21] Quan Chen, Wolfgang Kinzelbach, and Sascha Oswald. Nuclear magnetic resonance imaging for studies of flow and transport in porous media. *Journal of Environmental Quality*, 31(2):477–486, 2002.

[22] Andrew J. Onstad, Christopher J. Elkins, Frank Medina, Ryan B. Wicker, and John K. Eaton. Full-field measurements of flow through a scaled metal foam replica. *Experiments in Fluids*, 50(6):1571–1585, 2011.

[23] Gerd Mikolajczyk, Li Huang, Michaela Wilhelm, Wolfgang Dreher, and Stefan Odenbach. Colloid deposition in monolithic porous media – Experimental investigations using X-ray computed microtomography and magnetic resonance velocimetry. *Chemical Engineering Science*, 175:257–266, 2018.

[24] Berthold Noll. *Numerische Strömungsmechanik: Grundlagen.* Springer-Verlag, 1993.

[25] Mehrdad Sadeghi, Mojtaba Mirdrikvand, Georg R. Pesch, Wolfgang Dreher, and Jorg Thöming. Full-field analysis of gas flow within open-cell foams: comparison of micro-computed tomography-based CFD simulations with experimental magnetic resonance flow mapping data. *Experiments in Fluids*, 61(5):124, 2020.

[26] Martin Bruschewski, Sam Flint, and Sid Becker. Magnetic Resonance Velocimetry Measurement of Viscous Flows through Porous Media: Comparison with Simulation and Voxel Size Study. *Physics*, 3(4):1254–1267, 2021.

[27] Theodore C. Larson, William M. Kelly, Richard L. Ehman, and Felix W. Wehrli. Spatial misregistration of vascular flow during MR imaging of the CNS: cause and clinical significance. *American Journal of Neuroradiology*, 11(5):1041–1048, 1990.

[28] Dwight G. Nishimura, John I. Jackson, and John M. Pauly. On the nature and reduction of the displacement artifact in flow images. *Magnetic Resonance in Medicine*, 22(2):481–492, 1991.

[29] Marc Kouwenhoven, Mark B. M. Hofman, and Michiel Sprenger. Motion Induced Phase Shifts in MR: Acceleration Effects in Quantitative Flow Measurements—A Reconsideration. *Magnetic Resonance in Medicine*, 33(6):766–777, 1995.

[30] Chao Tang, Duane D. Blatter, and Dennis L. Parker. Accuracy of phase-contrast flow measurements in the presence of partial-volume effects. *Journal of Magnetic Resonance Imaging*, 3(2):377–385, 1993.

[31] Matt A. Bernstein, Kevin F. King, and Xiaohong Joe Zhou. *Handbook of MRI pulse sequences.* Elsevier, 2004.

[32] Paul T. Callaghan. *Principles of nuclear magnetic resonance microscopy.* Oxford University Press on Demand, 1993.

[33] Robert W. Brown, Yu-Chung N. Cheng, E. Mark Haacke, Michael R. Thompson, and Ramesh Venkatesan. *Magnetic resonance imaging: physical principles and sequence design.* John Wiley & Sons, 2014.

[34] Axel Haase, Jens Frahm, Dieter Matthaei, W. Hanicke, and K.-D. Merboldt. FLASH imaging. Rapid NMR imaging using low flip-angle pulses. *Journal of Magnetic Resonance (1969)*, 67(2):258–266, 1986.

[35] Allen D. Elster. Gradient-echo MR imaging: techniques and acronyms. *Radiology*, 186(1):1–8, 1993.

[36] William A. Edelstein, James M. S. Hutchison, Glyn Johnson, and Thomas Redpath. Spin warp NMR imaging and applications to human whole-body imaging. *Physics in Medicine & Biology*, 25(4):751–756, 1980.

[37] Juergen Hennig. Multiecho imaging sequences with low refocusing flip angles. *Journal of Magnetic Resonance (1969)*, 78(3):397–407, 1988.

[38] Mark H. Sankey, Daniel J. Holland, Andrew J. Sederman, and Lynn F. Gladden. Magnetic resonance velocity imaging of liquid and gas two-phase flow in packed beds. *Journal of Magnetic Resonance*, 196(2):142–148, 2009.

[39] Kristine John, Saad Jahangir, Udhav Gawandalkar, Willian Hogendoorn, Christian Poelma, Sven Grundmann, and Martin Bruschewski. Magnetic resonance velocimetry in high-speed turbulent flows: sources of measurement errors and a new approach for higher accuracy. *Experiments in Fluids*, 61(2):1–17, 2020.

[40] Daniel A. Clarke, Fabian Dolamore, Conan J. Fee, Petrik Galvosas, and Daniel J. Holland. Investigation of flow through triply periodic minimal surface-structured porous media using MRI and CFD. *Chemical Engineering Science*, 231:116264, 2021.

[41] Anila Lingamneni, Peter A. Hardy, Kimerly A. Powell, Norbert J. Pelc, and Richard D. White. Validation of cine phase-contrast MR imaging for motion analysis. *Journal of Magnetic Resonance Imaging*, 5(3):331–338, 1995.

[42] Norbert J. Pelc, Matt A. Bernstein, Ann Shimakawa, and Gary H. Glover. Encoding strategies for three-direction phase-contrast MR imaging of flow. *Journal of Magnetic Resonance Imaging*, 1(4):405–413, 1991.

[43] Adrian T. Lee, G. Bruce Pike, and Norbert J. Pelc. Three-Point Phase-Contrast Velocity Measurements with Increased Velocity-to-Noise Ratio. *Magnetic Resonance in Medicine*, 33(1):122–126, 1995.

[44] Hákon Gudbjartsson and Samuel Patz. The rician distribution of noisy MRI data. *Magnetic Resonance in Medicine*, 34(6):910–914, 1995.

[45] Michael Loecher and Daniel B. Ennis. Velocity Reconstruction With Nonconvex Optimization for Low-Velocity-Encoding Phase-Contrast MRI. *Magnetic Resonance in Medicine*, 80(1):42–52, 2018.

[46] Elizabeth J. Nett, Kevin M. Johnson, Alex Frydrychowicz, Alejandro Munoz Del Rio, Eric Schrauben, Christopher J. Francois, and Oliver Wieben. Four-Dimensional Phase Contrast MRI With Accelerated Dual Velocity Encoding. *Journal of Magnetic Resonance Imaging*, 35(6):1462–1471, 2012.

[47] Susanne Schnell, Sameer A. Ansari, Can Wu, Julio Garcia, Ian G. Murphy, Ozair A. Rahman, Amir A. Rahsepar, Maria Aristova, Jeremy D. Collins, James C. Carr, and Michael Markl. Accelerated Dual-venc 4D Flow MRI for Neurovascular Applications. *Journal of Magnetic Resonance Imaging*, 46(1):102–114, 2017.

[48] Sean Callahan, Narayana S. Singam, Michael Kendrick, M. J. Negahdar, Hui Wang, Marcus F. Stoddard, and Amir A. Amini. Dual-Venc acquisition for

4D flow MRI in aortic stenosis with spiral readouts. *Journal of Magnetic Resonance Imaging*, 52(1):117–128, 2020.

[49] Bernard Stanford Massey and John Ward-Smith. *Mechanics of Fluids*. CRC Press, 2012.

[50] Joseph H. Spurk and Nuri Aksel. *Strömungslehre: Einführung in die Theorie der Strömungen*. Springer, 2019.

[51] Katsumi Kose. One-shot velocity mapping using multiple spin-echo EPI and its application to turbulent flow. *Journal of Magnetic Resonance (1969)*, 92(3):631–635, 1991.

[52] Katsumi Kose. Instantaneous flow-distribution measurements of the equilibrium turbulent region in a circular pipe using ultrafast NMR imaging. *Physical Review A*, 44(4):2495–2504, 1991.

[53] Katsumi Kose. Visualization of local shearing motion in turbulent fluids using echo-planar imaging. *Journal of Magnetic Resonance (1969)*, 96(3):596–603, 1992.

[54] Andrew J. Sederman, Mick D. Mantle, Craig Buckley, and Lynn F. Gladden. MRI technique for measurement of velocity vectors, acceleration, and autocorrelation functions in turbulent flow. *Journal of Magnetic Resonance*, 166(2):182–189, 2004.

[55] Alexander B. Tayler, Daniel J. Holland, Andrew J. Sederman, and Lynn F. Gladden. Exploring the origins of turbulence in multiphase flow using compressed sensing MRI. *Physical Review Letters*, 108(26):264505, 2012.

[56] J. von Rotta. Experimenteller Beitrag zur Entstehung turbulenter Strömung im Rohr. *Ingenieur-Archiv*, 24(4):258–281, 1956.

[57] John N. Armor. A history of industrial catalysis. *Catalysis Today*, 163(1):3–9, 2011.

[58] Robert J. Farrauto and Ronald M. Heck. Environmental catalysis into the 21st century. *Catalysis Today*, 55(1-2):179–187, 2000.

[59] Gabriele Centi and Siglinda Perathoner. Catalysis and sustainable (green) chemistry. *Catalysis Today*, 77(4):287–297, 2003.

[60] S. Kumar Dey and Niraj S. Mehta. Automobile pollution control using catalysis. *Resources, Environment and Sustainability*, 2:100006, 2020.

[61] A. Hermann. Haber und Bosch: Brot aus Luft-Die Ammoniaksynthese. *Physikalische Blätter*, 21(4):168–171, 1965.

[62] Franz Kainer. *Die Kohlenwasserstoff-Synthese nach Fischer-Tropsch*. Springer-Verlag, 1950.

[63] Leon R.S. Rosseau, Vesna Middelkoop, Hans A.M. Willemsen, Ivo Roghair, and Martin van Sint Annaland. Review on additive manufacturing of catalysts and sorbents and the potential for process intensification. *Frontiers in Chemical Engineering*, 4:834547, 2022.

[64] Gianpiero Groppi and Enrico Tronconi. Honeycomb supports with high thermal conductivity for gas/solid chemical processes. *Catalysis Today*, 105(3-4):297–304, 2005.

[65] Martyn V. Twigg and James T. Richardson. Fundamentals and applications of structured ceramic foam catalysts. *Industrial & Engineering Chemistry Research*, 46(12):4166–4177, 2007.

[66] Julia Große, Benjamin Dietrich, Holger Martin, Matthias Kind, Jérome Vicente, and Edme H. Hardy. Volume image analysis of ceramic sponges. *Chemical Engineering & Technology: Industrial Chemistry-Plant Equipment-Process Engineering-Biotechnology*, 31(2):307–314, 2008.

[67] Tatsuhiko Uda, Masahiro Tanaka, and Kenzo Munakata. Characteristics of honeycomb catalysts for oxidation of tritiated hydrogen and methane gases. *Fusion Engineering and Design*, 83(10-12):1715–1720, 2008.

[68] Martyn V. Twigg and James T. Richardson. Preparation and properties of ceramic foam catalyst supports. *Studies in Surface Science and Catalysis*, 91:345–359, 1995.

[69] Martyn V. Twigg and James T. Richardson. Theory and applications of ceramic foam catalysts. *Chemical Engineering Research and Design*, 80(2):183–189, 2002.

[70] Christoph Sinn, Jonas Wentrup, Georg R. Pesch, and Jorg Thöming. Heat transport in open-cell foams: CFD analysis of artificial heat sources vs fully resolved exothermal reactions. *Industrial & Engineering Chemistry Research*, 60(12):4542–4551, 2021.

[71] M. Allen Northrup, Thomas J. Kulp, and S. Michael Angel. Fluorescent particle image velocimetry: application to flow measurement in refractive index-matched porous media. *Applied Optics*, 30(21):3034–3040, 1991.

[72] S. Saleh, J. F. Thovert, and P. M. Adler. Measurement of two-dimensional velocity fields in porous media by particle image displacement velocimetry. *Experiments in Fluids*, 12(3):210–212, January 1992.

[73] Andreas Lehwald, Stefan Leschka, Katharina Zähringer, and Dominique Thévenin. Fluid dynamics and mixing behavior of a static mixer using simultaneously Particle Image Velocimetry and Planar Laser-Induced Fluorescence measurements. In *14th International Symposium on Applications of Laser Techniques to Fluid Mechanics, Lisbon, Portugal*, pages 1–9, 2008.

[74] Olga Mihailova, Victor Lim, Michael J. McCarthy, Kathryn L. McCarthy, and Serafim Bakalis. Laminar mixing in a SMX static mixer evaluated by positron emission particle tracking (PEPT) and magnetic resonance imaging (MRI). *Chemical Engineering Science*, 137:1014–1023, 2015.

[75] Seth Langford, Cody Wiggins, Daniel Tenpenny, and Arthur Ruggles. Positron emission particle tracking (PEPT) for fluid flow measurements. *Nuclear Engineering and Design*, 302:81–89, 2016.

[76] Charles L. Dumoulin, Steven P. Souza, M. F. Walker, and W. Wagle. Three-dimensional phase contrast angiography. *Magnetic Resonance in Medicine*, 9(1):139–149, 1989.

[77] Michael P. Marks, Norbert J. Pelc, Michael R. Ross, and Dieter R. Enzmann. Determination of cerebral blood flow with a phase-contrast cine MR imaging technique: evaluation of normal subjects and patients with arteriovenous malformations. *Radiology*, 182(2):467–476, 1992.

[78] M. O'Donnell. NMR blood flow imaging using multiecho, phase contrast sequences. *Medical Physics*, 12(1):59–64, 1985.

[79] G. L. Nayler, D. N. Firmin, and D. B. Longmore. Blood flow imaging by cine magnetic resonance. *Journal of Computer Assisted Tomography*, 10(5):715–722, 1986.

[80] Matthias-C. Dulce, Gerhard H. Mostbeck, Margaret O'Sullivan, Melvin Cheitlin, Gary R. Caputo, and Charles B. Higgins. Severity of aortic regurgitation: interstudy reproducibility of measurements with velocity-encoded cine MR imaging. *Radiology*, 185(1):235–240, 1992.

[81] John-Peder Escobar Kvitting, Tino Ebbers, Lars Wigström, Jan Engvall, Christian L. Olin, and Ann F. Bolger. Flow patterns in the aortic root and the aorta studied with time-resolved, 3-dimensional, phase-contrast magnetic resonance imaging: implications for aortic valve–sparing surgery. *The Journal of Thoracic and Cardiovascular Surgery*, 127(6):1602–1607, 2004.

[82] Alex Frydrychowicz, Michael Markl, Daniel Hirtler, Andreas Harloff, Christian Schlensak, Julia Geiger, Brigitte Stiller, and Raoul Arnold. Aortic Hemodynamics in Patients With and Without Repair of Aortic Coarctation: In Vivo Analysis by 4D Flow-Sensitive Magnetic Resonance Imaging. *Investigative Radiology*, 46(5):24–35, 2011.

[83] Dieter R. Enzmann and Norbert J. Pelc. Normal flow patterns of intracranial and spinal cerebrospinal fluid defined with phase-contrast cine MR imaging. *Radiology*, 178(2):467–474, 1991.

[84] Dieter R. Enzmann and Norbert J. Pelc. Cerebrospinal fluid flow measured by phase-contrast cine MR. *American Journal of Neuroradiology*, 14(6):1301–1307, 1993.

[85] Andreas A. Linninger, Michalis Xenos, David C. Zhu, Mahadevabharath R. Somayaji, Srinivasa Kondapalli, and Richard D. Penn. Cerebrospinal Fluid Flow in the Normal and Hydrocephalic Human Brain. *IEEE Transactions on Biomedical Engineering*, 54(2):291–302, 2007.

[86] Xiaohong Ren, Siegfried Stapf, and Bernhard Blümich. Magnetic resonance visualisation of flow and pore structure in packed beds with low aspect ratio. *Chemical Engineering & Technology: Industrial Chemistry-Plant Equipment-Process Engineering-Biotechnology*, 28(2):219–225, 2005.

[87] Li Huang, Gerd Mikolajczyk, Ekkehard Küstermann, Michaela Wilhelm, Stefan Odenbach, and Wolfgang Dreher. Adapted MR velocimetry of slow liquid flow in porous media. *Journal of Magnetic Resonance*, 276:103 – 112, 2017.

[88] Alexander Penn, Christopher M. Boyce, Thomas Kovar, Takuya Tsuji, Klaas P. Pruessmann, and Christoph R. Müller. Real-Time Magnetic Resonance Imaging of Bubble Behavior and Particle Velocity in Fluidized Beds. *Industrial & Engineering Chemistry Research*, 57(29):9674–9682, July 2018.

[89] Paul R. Moran, Richard A. Moran, and Nolan Karstaedt. Verification and evaluation of internal flow and motion. True magnetic resonance imaging by the phase gradient modulation method. *Radiology*, 154(2):433–441, 1985.

[90] Richard Hausmann, Jonathan S. Lewin, and Gerhard Laub. Phase-contrast MR angiography with reduced acquisition time: new concepts in sequence design. *Journal of Magnetic Resonance Imaging*, 1(4):415–422, 1991.

[91] Charles L. Dumoulin, Steven P. Souza, Robert D. Darrow, Norbert J. Pelc, William J. Adams, and Stephen A. Ash. Simultaneous acquisition of phase-contrast angiograms and stationary-tissue images with Hadamard encoding of flow-induced phase shifts. *Journal of Magnetic Resonance Imaging*, 1(4):399–404, 1991.

[92] Thomas E. Conturo and Bruce H. Robinson. Analysis of encoding efficiency in MR imaging of velocity magnitude and direction. *Magnetic Resonance in Medicine*, 25(2):233–247, 1992.

[93] Charles L. Dumoulin. Phase contrast MR angiography techniques. *Magnetic Resonance Imaging Clinics of North America*, 3(3):399–411, 1995.

[94] Miguel Arevallilo Herráez, David R. Burton, Michael J. Lalor, and Munther A. Gdeisat. Fast two-dimensional phase-unwrapping algorithm based on sorting by reliability following a noncontinuous path. *Applied Optics*, 41(35):7437–7444, 2002.

[95] Mark Jenkinson. Fast, automated, N-dimensional phase-unwrapping algorithm. *Magnetic Resonance in Medicine*, 49(1):193–197, 2003.

[96] Marvin A. Schofield and Yimei Zhu. Fast phase unwrapping algorithm for interferometric applications. *Optics Letters*, 28(14):1194–1196, 2003.

[97] Hussein S. Abdul-Rahman, Munther A. Gdeisat, David R. Burton, Michael J. Lalor, Francis Lilley, and Christopher J. Moore. Fast and robust three-dimensional best path phase unwrapping algorithm. *Applied Optics*, 46(26):6623–6635, 2007.

[98] Hussein Abdul-Rahman, Miguel Arevalillo-Herráez, Munther Gdeisat, David Burton, Michael Lalor, Francis Lilley, Christopher Moore, Daniel Sheltraw, and Mohammed Qudeisat. Robust three-dimensional best-path phase-unwrapping algorithm that avoids singularity loops. *Applied Optics*, 48(23):4582–4596, 2009.

[99] Hugo Carrillo, Axel Osses, Sergio Uribe, and Cristóbal Bertoglio. Optimal Dual-VENC Unwrapping in Phase-Contrast MRI. *IEEE Transactions on Medical Imaging*, 38(5):1263–1270, 2019.

[100] Frank G. Shellock and John V. Crues. Temperature changes caused by MR imaging of the brain with a head coil. *American Journal of Neuroradiology*, 9(2):287–291, 1988.

[101] Kenneth R. Foster and Roland Glaser. Thermal mechanisms of interaction of radiofrequency energy with biological systems with relevance to exposure guidelines. *Health Physics*, 92(6):609–620, 2007.

[102] Erwin L. Hahn. Spin echoes. *Physical Review*, 80(4):580–594, 1950.

[103] Bernd André Jung and Matthias Weigel. Spin echo magnetic resonance imaging. *Journal of Magnetic Resonance Imaging*, 37(4):805–817, 2013.

[104] Nathan H. Williamson, Michal E. Komlosh, Dan Benjamini, and Peter J. Basser. Limits to flow detection in phase contrast MRI. *Journal of Magnetic Resonance Open*, 2-3:100004, 2020.

[105] G. Shiko, Andrew J. Sederman, and Lynn F. Gladden. MRI technique for the snapshot imaging of quantitative velocity maps using RARE. *Journal of Magnetic Resonance*, 216:183–191, 2012.

[106] Martin Bruschewski, Hanna Kolkmann, Kristine John, and Sven Grundmann. Phase-contrast single-point imaging with synchronized encoding: a more reliable technique for in vitro flow quantification. *Magnetic Resonance in Medicine*, 81(5):2937–2946, 2019.

[107] Andrea Amar, Bernhard Blümich, and Federico Casanova. Rapid Multiphase Flow Dynamics Mapped by Single-Shot MRI Velocimetry. *ChemPhysChem*, 11(12):2630–2638, 2010.

[108] Cynthia B. Paschal and H. Douglas Morris. K-space in the clinic. *Journal of Magnetic Resonance Imaging*, 19(2):145–159, 2004.

[109] Donald W. McRobbie, Elizabeth A. Moore, Martin J. Graves, and Martin R. Prince. *MRI from Picture to Proton*. Cambridge University Press, 2017.

[110] E. Mark Haacke and Gerald W. Lenz. Improving MR image quality in the presence of motion by using rephasing gradients. *American Journal of Roentgenology*, 148(6):1251–1258, 1987.

[111] Pradip M. Pattany, Jeffrey J. Phillips, Lee C. Chiu, James D. Lipcamon, Jeffrey L. Duerk, James M. McNally, and Surya N. Mohapatra. Motion artifact suppression technique (MAST) for MR imaging. *Journal of Computer Assisted Tomography*, 11(3):369–377, 1987.

[112] Allen D. Elster. Motion artifact suppression technique (MAST) for cranial MR imaging: superiority over cardiac gating for reducing phase-shift artifacts. *American Journal of Neuroradiology*, 9(4):671–674, 1988.

[113] Nobuyuki Otsu. A Threshold Selection Method from Gray-Level Histograms. *IEEE Transactions on Systems, Man, and Cybernetics*, 9(1):62–66, 1979.

[114] R. E. Wysong, D. P. Madio, and Irving J. Lowe. A novel eddy current compensation scheme for pulsed gradient systems. *Magnetic Resonance in Medicine*, 31(5):572–575, 1994.

[115] H. Michael Gach, Irving J. Lowe, David P. Madio, Arvind Caprihan, Stephen A. Altobelli, Dean O. Kuethe, and Eiichi Fukushima. A programmable pre-emphasis system. *Magnetic Resonance in Medicine*, 40(3):427–431, 1998.

[116] Hsu-Hsia Peng, Simon Bauer, Teng-Yi Huang, Hsiao-Wen Chung, Jürgen Hennig, Bernd Jung, and Michael Markl. Optimized parallel imaging for dynamic PC-MRI with multidirectional velocity encoding. *Magnetic Resonance in Medicine*, 64(2):472–480, 2010.

[117] Julia Busch, Daniel Giese, and Sebastian Kozerke. Image-based background phase error correction in 4D flow MRI revisited. *Journal of Magnetic Resonance Imaging*, 46(5):1516–1525, 2017.

[118] Carolin Wüstenhagen, Kristine John, Sönke Langner, Martin Brede, Sven Grundmann, and Martin Bruschewski. CFD validation using in-vitro MRI velocity data – Methods for data matching and CFD error quantification. *Computers in Biology and Medicine*, 131:104230, 2021.

[119] J. F. Guelich and U. Bolleter. Pressure Pulsations in Centrifugal Pumps. *Journal of Vibration and Acoustics*, 114(2):272–279, 1992.

[120] R. Spence and J. Amaral-Teixeira. Investigation into pressure pulsations in a centrifugal pump using numerical methods supported by industrial tests. *Computers & Fluids*, 37(6):690–704, 2008.

[121] D. Bach, F. Schmich, T. Masselter, and T. Speck. A review of selected pumping systems in nature and engineering—potential biomimetic concepts for improving displacement pumps and pulsation damping. *Bioinspiration & Biomimetics*, 10(5):051001, 2015.

[122] Lijian Shi, Yao Yuan, Haifeng Jiao, Fangping Tang, Li Cheng, Fan Yang, Yan Jin, and Jun Zhu. Numerical investigation and experiment on pressure pulsation characteristics in a full tubular pump. *Renewable Energy*, 163:987–1000, 2021.

[123] Katherine Selby, David Saloner, Charles M. Anderson, Daisy Chien, and Ralph E. Lee. MR angiography with a cardiac-phase–specific acquisition window. *Journal of Magnetic Resonance Imaging*, 2(6):637–643, 1992.

[124] Mojtaba Mirdrikvand, Mehrdad Sadeghi, Georg R. Pesch, Wolfgang Dreher, and Jorg Thöming. Full-Field Comparison of MRV and CFD of Gas Flow through Regular Catalytic Monolithic Structures. *Processes*, 9(3):566, 2021.

[125] Jan-Willem Lankhaar, Mark B. M. Hofman, J. Tim Marcus, Jaco J. M. Zwanenburg, Theo J. C. Faes, and Anton Vonk-Noordegraaf. Correction of phase offset errors in main pulmonary artery flow quantification. *Journal of Magnetic Resonance Imaging*, 22(1):73–79, 2005.

[126] Mark Hofman, Manouk J. A. Rodenburg, Karin Markenroth Bloch, Beat Werner, Jos J. M. Westenberg, Emanuela R. Valsangiacomo Buechel, Robin Nijveldt, Onno A. Spruijt, Philip J. Kilner, Albert C. van Rossum, and Peter D. Gatehouse. In-vivo validation of interpolation-based phase offset correction in cardiovascular magnetic resonance flow quantification: a multi-vendor, multi-center study. *Journal of Cardiovascular Magnetic Resonance*, 21(1):1–13, 2019.

[127] Savine Minderhoud, Nikki van der Velde, Jolanda J. Wentzel, Rob J. van der Geest, Mohammed Attrach, Piotr A. Wielopolski, Ricardo P. J. Budde, Willem A. Helbing, Jolien W. Roos-Hesselink, and Alexander Hirsch. The clinical impact of phase offset errors and different correction methods in cardiovascular magnetic resonance phase contrast imaging: a multi-scanner study. *Journal of Cardiovascular Magnetic Resonance*, 22(1):1–13, 2020.

[128] David A. G. Wicks, Gareth J. Barker, and Paul S. Tofts. Correction of intensity nonuniformity in MR images of any orientation. *Magnetic Resonance Imaging*, 11(2):183–196, 1993.

[129] Michael J. Benson, Christopher J. Elkins, Paul D. Mobley, Marcus T. Alley, and John K. Eaton. Three-dimensional concentration field measurements in a mixing layer using magnetic resonance imaging. *Experiments in Fluids*, 49:43–55, 2010.

[130] Alex J. Barker, Pim van Ooij, Krishna Bandi, Julio Garcia, Mazen Albaghdadi, Patrick McCarthy, Robert O. Bonow, James Carr, Jeremy Collins, S. Chris Malaisrie, and Michael Markl. Viscous energy loss in the presence of abnormal aortic flow. *Magnetic Resonance in Medicine*, 72(3):620–628, 2014.

[131] Christian Binter, Utku Gülan, Markus Holzner, and Sebastian Kozerke. On the accuracy of viscous and turbulent loss quantification in stenotic aortic flow

using phase-contrast MRI. *Magnetic Resonance in Medicine*, 76(1):191–196, 2016.

[132] Shaeez Usman Abdulla, David Reutens, Steffen Bollmann, and Viktor Vegh. MRI phase offset correction method impacts quantitative susceptibility mapping. *Magnetic Resonance Imaging*, 74:139–151, 2020.

[133] Maria Aristova, Alireza Vali, Sameer A. Ansari, Ali Shaibani, Tord D. Alden, Michael C. Hurley, Babak S. Jahromi, Matthew B. Potts, Michael Markl, and Susanne Schnell. Standardized Evaluation of Cerebral Arteriovenous Malformations Using Flow Distribution Network Graphs and Dual-venc 4D Flow MRI. *Journal of Magnetic Resonance Imaging*, 50(6):1718–1730, 2019.

[134] Masatoki Nakaza, Mitsuo Matsumoto, Tetsuro Sekine, Tatsuya Inoue, Takahiro Ando, Masashi Ogawa, Makoto Obara, Olgierd Leonowicz, Shinichiro Kumita, and Jitsuo Usuda. Dual-VENC 4D Flow MRI Can Detect Abnormal Blood Flow in the Left Atrium That Potentially Causes Thrombosis Formation after Left Upper Lobectomy. *Magnetic Resonance in Medical Sciences*, 21(3):433–443, 2022.

[135] Simin Mahinrad, Can Ozan Tan, Yue Ma, Maria Aristova, Andrew L. Milstead, Donald Lloyd-Jones, Susanne Schnell, Michael Markl, and Farzaneh A. Sorond. Intracranial Blood Flow Quantification by Accelerated Dual-venc 4D Flow MRI: Comparison With Transcranial Doppler Ultrasound. *Journal of Magnetic Resonance Imaging*, 56(4):1256–1264, 2022.

[136] Thomas W. Blythe, Andrew J. Sederman, J. Mitchell, E. H. Stitt, Andrew P. E. York, and Lynn F. Gladden. Characterising the rheology of non-Newtonian fluids using PFG-NMR and cumulant analysis. *Journal of Magnetic Resonance*, 255:122–131, 2015.

[137] Emil K. S. Espe, Jan Magnus Aronsen, Biljana Skrbic, Vidar Magne Skulberg, Jürgen E. Schneider, Ole M. Sejersted, Lili Zhang, and Ivar Sjaastad. Improved MR phase-contrast velocimetry using a novel nine-point balanced motion-encoding scheme with increased robustness to eddy current effects. *Magnetic Resonance in Medicine*, 69(1):48–61, 2013.

[138] Petter Dyverfeldt, Malenka Bissell, Alex J. Barker, Ann F. Bolger, Carl-Johan Carlhäll, Tino Ebbers, Christopher J. Francios, Alex Frydrychowicz, Julia Geiger, Daniel Giese, Michael D. Hope, Philip J. Kilner, Sebastian Kozerke, Saul Myerson, Stefan Neubauer, Oliver Wieben, and Michael Markl. 4D flow cardiovascular magnetic resonance consensus statement. *Journal of Cardiovascular Magnetic Resonance*, 17(1):1–19, 2015.

[139] F. G. Souza Jr., A. C. Ferreira, A. Varela, G. E. Oliveira, F. Machado, E. D. Pereira, E. Fernandes, J. C. Pinto, and M. Nele. Methodology for determination of magnetic force of polymeric nanocomposites. *Polymer Testing*, 32(8):1466–1471, 2013.

[140] W. M. Haynes, David R. Lide, and Thomas J. Bruno. *CRC Handbook of Chemistry and Physics 95th Edition.* CRC Press Boca Raton, FL, 2014.

[141] Henk Kaarle Versteeg and Weeratunge Malalasekera. *An introduction to computational fluid dynamics: the finite volume method.* Pearson education, 2007.

[142] Augusto Della Torre, Gianluca Montenegro, G. R. Tabor, and M. L. Wears. CFD characterization of flow regimes inside open cell foam substrates. *International Journal of Heat and Fluid Flow*, 50:72–82, 2014.

[143] Sebastian Meinicke, Christian-Ole Möller, Benjamin Dietrich, Michael Schlüter, and Thomas Wetzel. Experimental and numerical investigation of single-phase hydrodynamics in glass sponges by means of combined μPIV measurements and CFD simulation. *Chemical Engineering Science*, 160:131–143, 2017.

[144] Christoph Sinn, Jonas Wentrup, Georg R. Pesch, Jorg Thöming, and Lars Kiewidt. Structure-heat transport analysis of periodic open-cell foams to be used as catalyst carriers. *Chemical Engineering Research and Design*, 166:209–219, 2021.

[145] Augusto Della Torre, Francesco Lucci, Gianluca Montenegro, Angelo Onorati, P. Dimopoulos Eggenschwiler, Enrico Tronconi, and Gianpiero Groppi. CFD modeling of catalytic reactions in open-cell foam substrates. *Computers & Chemical Engineering*, 92:55–63, 2016.

[146] Jason D. Cooper, Li Liu, Nicholas P. Ramskill, Timothy C. Watling, Andrew P. E. York, E. Hugh Stitt, Andrew J. Sederman, and Lynn F. Gladden. Numerical and experimental studies of gas flow in a particulate filter. *Chemical Engineering Science*, 209:115179, 2019.

[147] Mehrdad Sadeghi, Adrian Ricke, Georg R. Pesch, Wolfgang Dreher, and Jorg Thöming. Comparative full-field velocimetry of liquid flow within monolithic catalyst carriers via CFD simulations and MRV measurements. *Experiments in Fluids*, 64(8):138, 2023.

Acknowledgement

Versicherung an Eides Statt:

Ich, Adrian Ricke, versichere an Eides Statt durch meine Unterschrift, dass ich die vorstehende Arbeit selbständig und ohne fremde Hilfe angefertigt und alle Stellen, die ich wörtlich dem Sinne nach aus Veröffentlichungen entnommen habe, als solche kenntlich gemacht habe, mich auch keiner anderen als der angegebenen Literatur oder sonstiger Hilfsmittel bedient habe.
Ich versichere an Eides Statt, dass ich die vorgenannten Angaben nach bestem Wissen und Gewissen gemacht habe und dass die Angaben der Wahrheit entsprechen und ich nichts verschwiegen habe.
Die Strafbarkeit einer falschen eidesstattlichen Versicherung ist mir bekannt, namentlich die Strafandrohung gemäß § 156 StGB bis zu drei Jahren Freiheitsstrafe oder Geldstrafe bei vorsätzlicher Begehung der Tat bzw. gemäß § 161 Abs. 1 StGB bis zu einem Jahr Freiheitsstrafe oder Geldstrafe bei fahrlässiger Begehung.